Numerical Modelling of River Discharge Effects on Hypoxia and Its Long-term Responses to Climate Change in the Ariake/Yatsushiro Sea, Japan

郝, 琳

https://hdl.handle.net/2324/7182423

出版情報：Kyushu University, 2023, 博士（工学）, 課程博士
バージョン：
権利関係：

NUMERICAL MODELLING OF RIVER DISCHARGE EFFECTS ON HYPOXIA AND ITS LONG-TERM RESPONSES TO CLIMATE CHANGE IN THE ARIAKE AND YATSUSHIRO SEA, JAPAN

LIN HAO

Abstract

Climate change is driving dramatic transformations in the natural environment of coastal marine areas. The consequential shifts in seawater temperature, ocean acidification, rising sea levels, and resulting damage to marine ecosystems have drawn considerable attention from scientists, policymakers, and the broader public. These changes not only impact marine life directly but also have indirect consequences, altering weather patterns, affecting coastal communities, influencing economies, and impacting global biodiversity.

Dissolved oxygen (DO) serves as a critical indicator for sustaining the health of marine ecosystems. Nonetheless, reports of declining DO levels have been reported in numerous oceans, shelf seas, and lakes worldwide since 1950s. Hypoxia, defined as DO below 3 mg/L, is considered to be strongly associated with the amplified frequency of extreme rainfall events driven by climate change, which poses a mounting threat to marine ecosystems on a global scale. However, in many estuarine and coastal waters, DO levels are intricately linked to the interaction of complex physical and biochemical processes. This complexity poses a significant challenge in assessing DO dynamics and maintaining a balanced aquatic ecosystem, presenting an ongoing issue within oceanography.

The Ariake Sea and the Yatsushiro Sea are semi-enclosed coastal water areas characterized by features resembling a Region of Freshwater Influence (ROFI). In recent years, the Ariake Sea and Yatsushiro Sea have faced pronounced water quality deterioration, including hypoxia and red tides, significantly impacting local fisheries. After 2000, the decline of cultured Nori (seaweed) has emerged as a crucial concern in Ariake Sea fisheries, while clam farming has become a focal issue in Yatsushiro Sea fisheries since 2010. An increasing number of studies have substantiated that hypoxia, as a significant contributor to the degradation of marine ecosystems in both bays, has shown a steady increase in both its duration and spatial extent over time.

However, a comprehensive analysis of the duration and spatiotemporal distribution of hypoxia attributed to climate change remains incomplete. Two primary reasons contribute to this: firstly, conducting long-term assessments of hypoxia development through field observations faces challenges due to inadequate data support; and secondly, the complexity of the physical ecology of estuaries makes models limited in their practical application and requires that these models have the ability to comprehensively analyze and simulate hydrodynamic and ecological processes.

In this study, we utilized numerical models that involved coupling a general three-dimensional (3-D) hydrodynamic coastal model with a lower-trophic ecosystem model. We aim to find out the potential causes behind seasonal hypoxic events and to evaluate the long-term responses to climate change. The study within this thesis is structured across seven chapters, outlined as follows:

Chapter 1 outlines the research background, objectives, and overall study outline.

Chapter 2 provides an overview of the present conditions and challenges faced by the Ariake/Yatsushiro Sea, exploring the impact of climate change on shallow sea aquatic environments and ecosystems through literature review.

Chapter 3 presents the evaluation of the impacts of extreme summer precipitation events on the marine environment of the Ariake Sea. It aims to illuminate the relationship between salinity stratification and variations in DO levels. This study particularly focused on investigating the influence of the historic 2020 Kyushu Floods, one of the largest rainfall events in recent history, on the development of hypoxia. Findings suggest that large-scale effluent events could exacerbate salinity stratification, leading to hypoxic conditions.

Chapter 4 shows the influence of summer effluent on bottom hypoxia within the Yatsushiro Sea. Results highlighted that the 2020 Kyushu Floods induced severe hypoxia across extensive areas. Persistent low DO levels in the southern region may be attributed to limited flow velocity and restricted water exchange.

Chapter 5 explores the correlation between river discharge and the duration of hypoxia in the Ariake Sea during the summer rainy season. The analysis provides insights into varying effluent scales on environmental dynamics. The study also assessed the stratification of the Ariake Sea due to freshwater inflow using a stratification index. The results indicate that the duration of hypoxia displayed a strong positive correlation between hypoxia duration and effluent volume near the river mouth, supported by notably high correlation coefficients.

Chapter 6 provides a comprehensive analysis of long-term water quality changes in the Ariake Sea, emphasizing trends of increasing hypoxia across spatial scales. The investigation explores climate change impacts on critical variables—temperature, salinity, DO, and nutrient levels. Findings over the past three decades highlight distinct responses in environmental factors to climate change, resulting in notable shifts in temperature patterns and altered precipitation trends.

Chapter 7 summarizes the conclusions obtained from this study and future work.

Acknowledgment

I extend my deepest gratitude to those whose unwavering support and guidance were pivotal in the completion of this article.

My utmost appreciation goes to Professor Shinichiro Yano, my supervisor from the Department of Urban Environmental Engineering at Kyushu University. His patient guidance, invaluable advice, and constant encouragement not only steered me through this thesis but also significantly influenced my future aspirations. I am equally thankful to my professor for providing invaluable academic exchange opportunities and enriching my understanding of my field. I consider it an immense privilege and honor to have had the opportunity to work and study under his invaluable guidance.

Alongside expressing my gratitude to my supervisor, I extend my heartfelt appreciation to the rest committee members, Prof. Takahiro Kuba and Prof. Masaru Yamashiro of Kyushu University. Their valuable insights, encouragement, and thought-provoking questions were instrumental in broadening the scope of my research and incorporating diverse perspectives.

I am equally grateful to Associate Professor Yasuyuki Maruya of the Environmental Fluid Dynamics Laboratory for his invaluable insights and guidance during my research. Additionally, I would like to express my heartfelt gratitude to Ms. Yoko Kaneko, the administrative assistant in our laboratory, whose generous assistance with business trip procedures proved invaluable.

I extend my sincere appreciation to the China Scholarship Council (CSC) for sponsoring my doctoral research at Kyushu University. Your generosity and support have been instrumental in my academic journey, and I am profoundly honored to be one of your recipients.

I extend my deepest gratitude to all members of the Environmental Fluid Dynamics Laboratory, Department of Civil Engineering, Kyushu University. The shared experiences have left an indelible mark on me, creating cherished memories that will endure a lifetime.

My heartfelt gratitude goes to my beloved family for their unwavering support, unwavering faith, and enduring patience throughout this journey. Furthermore, I am indebted to my friends whose attentive ear, unwavering encouragement, and dedicated time assisted me in overcoming the challenges encountered during the completion of this thesis.

Each of you has played an integral role in this achievement, and for that, I am deeply and sincerely grateful.

Contents

Chapter1

Chapter 2

Chapter 3

Chapter 4

Chapter 5

Chapter 6

Chapter 7

List of Figures

List of Tables

Chapter1

Introduction

1.1 Research Background

1.1.1 Response of shallow coastal seas to climate change

Since the Industrial Revolution, the influence of human activities on the natural environment has steadily increased. Life on Earth is currently undergoing one of the most momentous decades in terms of climate change (Thornton et al., 2014). The 5th and 6th assessment reports (AR5 and AR6) of the Intergovernmental Panel on Climate Change (IPCC) have offered a more precise insight into the considerable and progressively irreversible harm inflicted upon terrestrial, freshwater, coastal, and open ocean ecosystems due to climate change (IPCC, 2014 and 2023). The World Meteorological Organization (WMO) projects a probability that global average temperatures will surpass pre-industrial levels by more than 1.5°C for at least one year within the next five years (IPCC, 2018). Global warming plays a crucial role in driving changes within the climate system, resulting in the intensification and increased complexity of climate events (AghaKouchak et al., 2020). For instance, each additional 0.5°C of global warming brings about noticeable increases in the intensity and frequency of hot extremes, such as heatwaves, heavy precipitation, as well as agricultural and ecological droughts in certain regions (IPCC, 2018). The latest AR6 report (IPCC, 2023) indicates that global surface temperatures are projected to continue rising at least into the middle of this century under all considered emission scenarios (Fig. 1.1a and b), while precipitation is expected to increase in high-latitude regions, the equatorial Pacific, and certain monsoon areas, but decrease in some subtropical and limited tropical regions under scenarios SSP2-4.5, SSP3-7.0, and SSP5-8.5 (Fig. 1.1c).

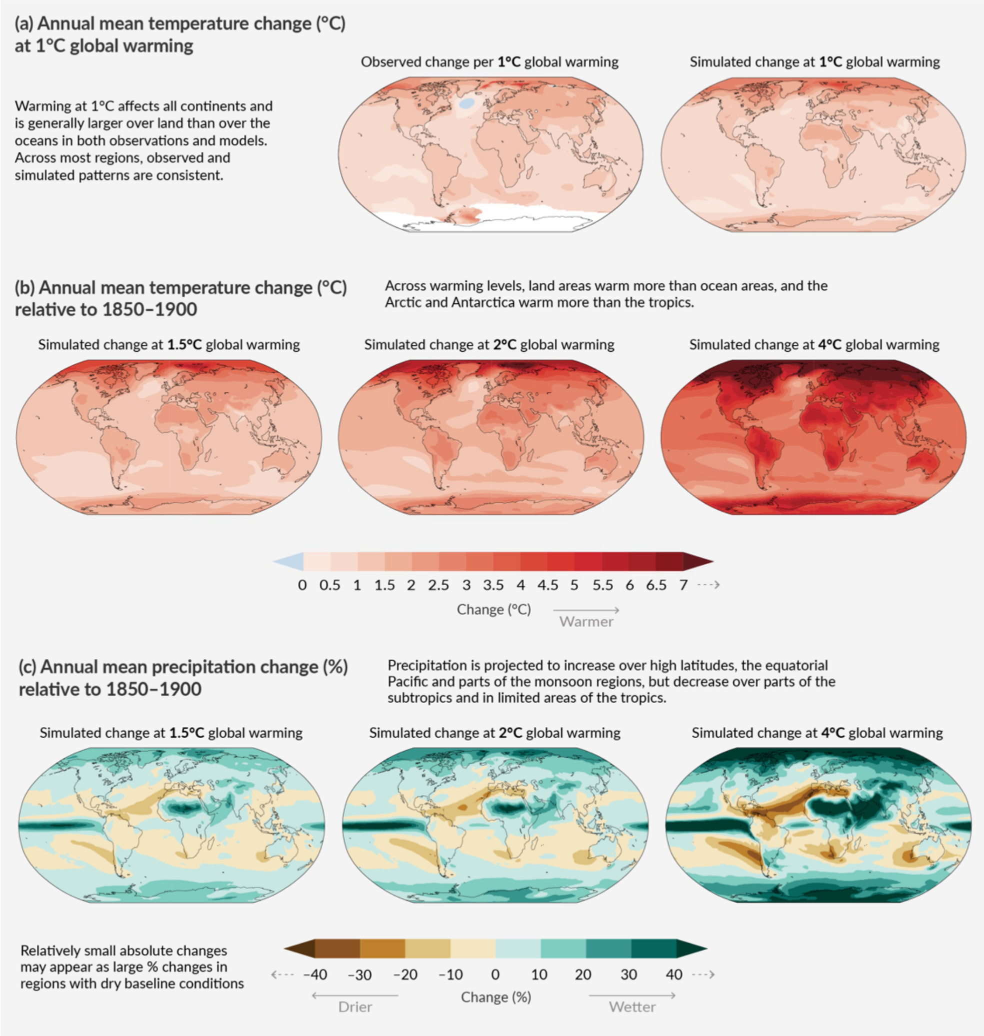

Figure 1.1 Annual Mean Surface Temperature Changes: (a) Comparison of Observed and Simulated Changes in Annual Mean Surface Temperature, (b) Simulated Annual Mean Temperature Changes (°C), and (c) Precipitation Changes (%). (source: IPCC, 2023)

As the greatest carbon sink on the Earth, the ocean absorbs the excess heat and energy released from the continuously increasing greenhouse gas emissions trapped in the Earth's system. The UN Climate Change has shown that human-driven global warming has become the primary driver of transformation in the marine environment, including ice-melting, sea-level rise, marine heatwaves, and ocean acidification (United Nations Environment Programme, 2023). These changes will ultimately have lasting impacts on marine biodiversity, as well as the livelihoods of ocean and coastal communities. Simultaneously, human activities are altering rainfall patterns and increasing the occurrence of extreme precipitation events as a result of climate change. The AR6 report indicates that since 1950s, the average precipitation on a global scale may have already increased, and the rate of increase has been even more rapid since the 1980s (IPCC, 2023). These alterations in precipitation patterns not only have significant impacts on terrestrial agriculture and ecosystems but also affect the salinity distribution in the near-surface ocean and the balance of coastal marine ecosystems.

The shallow coastal sea, as a vital link connecting the ocean and continent, not only provides humans with ample fish resources but also plays a pivotal role in preserving the aquatic ecological environment. Globally, shallow coastal seas are the primary source of fish caught by humans, accounting for 90% of global fish catches (Simpson & Sharples, 2012). In recent years, the excessive development of the marine economy in coastal regions has posed significant challenges to the offshore environment and ecosystems. This development has led to issues like overfishing, resulting in the depletion of fish stocks, the influx of excess nutrients leading to eutrophication, and the gradual emergence of hypoxia (Kwiatkowski et al., 2020). Consequently, these alterations render coastal marine environments exceptionally vulnerable and highly responsive to the impacts of climate change, such as rising sea levels and the increasing occurrence of extreme precipitation and storm surges (Thornton et al., 2014).

1.1.2 The role of DO in aquatic ecosystems

Dissolved oxygen (DO), as a pivotal component of aquatic systems, plays a crucial role in the aquatic ecological environment. Primarily, it serves as the essential oxygen source that enables aquatic organisms to respire and sustain their existence. Furthermore, DO actively engages in redox reactions within the water, facilitating the decomposition of organic waste, the breakdown of pollutants, and the preservation of the chemical equilibrium of the aquatic ecosystem. DO in seawater primarily originates from two main sources: the atmosphere and the process of photosynthesis carried out by phytoplankton, as shown in Fig. 1.2. Presently, there is a global decline in DO levels, resulting in significant harm to aquatic life. Declines in DO concentration linked to climate change and human activity are among the most significant changes in coastal and ocean waters (Thornton et al., 2014).

Global warming is considered to be the primary cause of DO depletion in open oceans

(Schmidtko et al., 2017; Kwiatkowski et al., 2020). The susceptibility of diverse aquatic environments to external stressors varies depending on their geomorphology and circulation (Diaz, 2001). In most estuaries and coastal waters, however, DO depletion is a complex interaction that can be understood as a coupled response of physical factors and biochemical factors, such as warming caused by climate change, leading to the increase in biological metabolism and reduction of DO solubility (Scanes et al., 2020; Zhang et al., 2022), eutrophication that triggers the excessive production of organic matter to consume oxygen in the water (Hagy et al., 2004; Murphy et al., 2011), and stratification primarily due to large amounts of freshwater inflow, which inhibits water exchange and leads to reduced oxygen levels in deeper water (Wiseman et al., 1997; Tishchenko et al., 2013; Yu et al., 2015). Additionally, wind stress somewhat promotes DO transport by generating waves and eddies (Ni et al., 2016). Marine organisms, particularly benthic species, are highly susceptible to changes in oxygen levels due to their limited contact with atmospheric oxygen supply and oxygen depletion in underlying sediment (Diaz and Rosenberg, 1995; Coley et al., 2007).

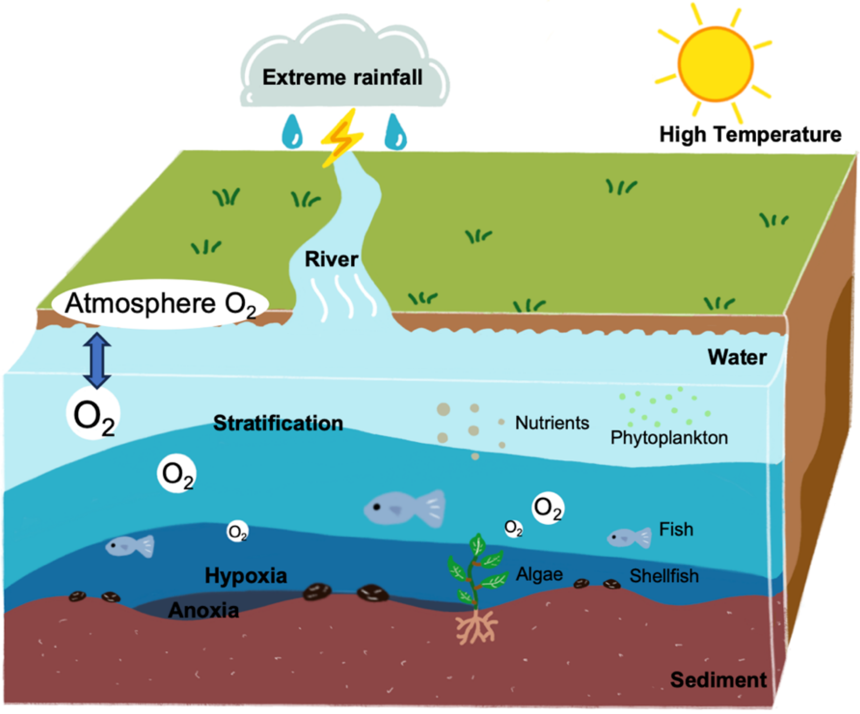

Figure 1.2 Conceptual diagram of oxygen dynamics in shallow water.

1.1.3 The Ariake/Yatsushiro Sea: a region of freshwater influence

The Ariake Sea, as the object of this study, is an estuary or bay-type freshwater influence area (ROFI) surrounded by Fukuoka, Saga, Nagasaki, and Kumamoto Prefectures, all of which are located in Kyushu Island, western Japan (Fig. 1.2). It is one of the most important shallow seas for fisheries and seaweed production in western Japan (Yagi et al., 2011). Simultaneously, it is the largest bay in Kyushu, about 100 kilometers long, with an average width of 18 kilometers and a depth of 20 m. Due to its large length-to-width ratio and shape formation, the oscillation period of the inner parts of the bay resonates with the semidiurnal tide in the outer sea (Tabata et al., 2015). Therefore, the Ariake Sea is also considered to have the largest tidal range in Japan, with a tidal range of 3-6 m and extensive mudflats account for 40% of the total area of tidal flats in Japan. Since the tidal flats provide a unique ecosystem for a large amount of marine and amphibious life, the environment in the Arisaka Sea allows a wide range of marine products to be harvested. It provides approximately 50% of the total production in Japan, especially the cultivation of Nori (seaweed). Moreover, the Ariake Sea is well-known for its fishery products, which has been dubbed the “Sea of Treasure” due to its abundant fishery resources (Jia et al., 2018).

There are eight A-class rivers as the main freshwater source flows into the Ariake Sea, which supplies large amounts of nutrients and suspended sediments to the bay. The Chikugo River, as the largest freshwater source inflow to the bay, connects to the northern part of the Ariake Sea. High concentration of suspended clay and silt in the Chikugo River, shallow depth and large tidal amplitude generate high turbidity and low transparency in the inner area of the bay (Azhikodan & Yokoyama, 2018). And the off-Kumamoto area, which is in the middle and eastern part of the bay, is surrounded by the two main rivers, the Midori River and Shira River respectively, the tidal flat here is mostly sandy (Hayami et al., 2015; Tsutsumi, 2006).

Isahaya Bay is located in the western part of the Ariake Sea and has been once known as one of the largest tidal flats in Japan. However, its topography was changed with the reclamation project of the construction of the 7 km long Isahaya Sea dike in 1997. The main purposes of the dike were to reclaim land for farming and for flood prevention. Since then, the fishery in the Ariake Sea has been on the decline and the water quality of the regulating reservoir in the bay has deteriorated dramatically (Jia et al., 2018). In 2015, compared to 1989 figures, there was a 27% reduction in the total catch (from 58,477 to 15,612 tons) and a 20% decrease in fish catch (from 12,294 to 2,498 tons) (Sasaki, 2017). Many studies indicated that the decrease in fisheries is likely to be related to the reclamation project, which also caused the deterioration of the sea floor environment.

The Yatsushiro Sea is located between Kumamoto and Kagoshima Prefectures and is connected to the southern part of the Ariake Sea. Similar to the Ariake Sea, it is a typical semi-enclosed sea area affected by ROFI. The Kuma River is the only A-class river that flows into the bay. In recent years, the Yatsushiro Sea has witnessed a substantial surge in red tide occurrences, coinciding with escalating water temperatures (Takikawa et al., 2005). Moreover, the bay has experienced a marked decline in annual catches of Manila clams and various groundfish species like Nibe Croaker and Sole (Ministry of the Environment, 2017).

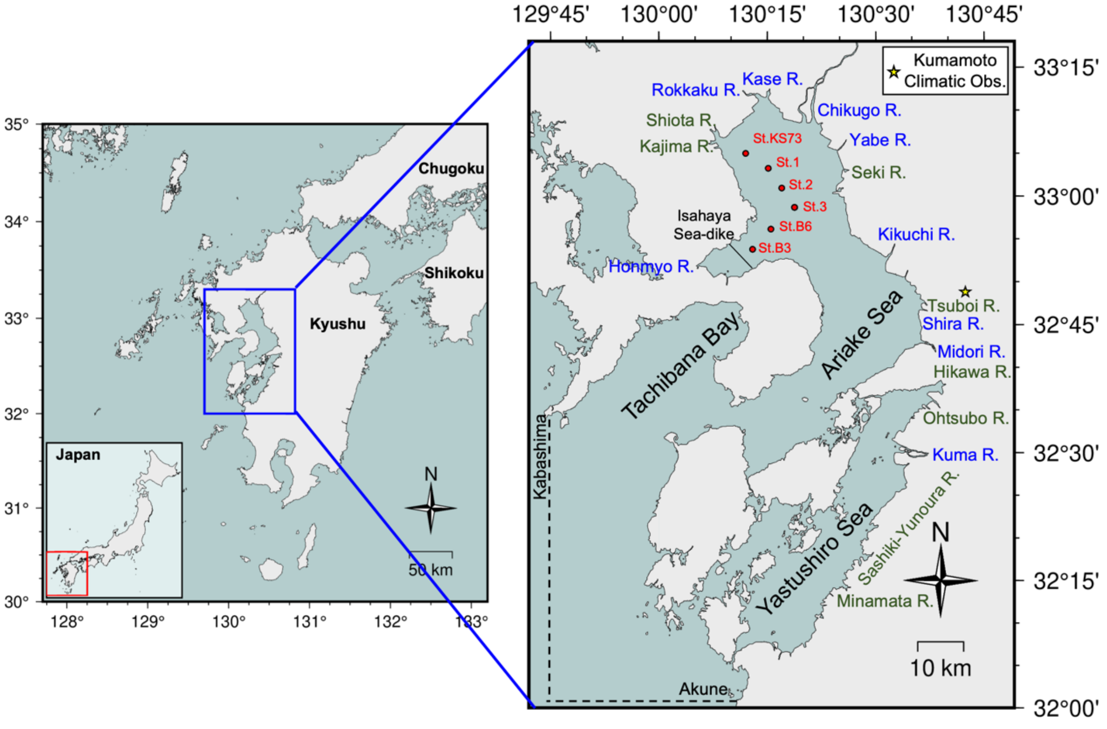

Figure 1.3 Location map of Ariake/Yatsushiro Sea and its major tributaries. Blue and green letters represent class A and class B rivers, respectively. The red dots show the observational stations and the pentagram shows the Kumamoto climate observation station.

1.2 Objectives

The Ariake/Yatsushiro Sea, one of Japan's largest bays, serves as a critical marine ecosystem and plays a vital role in supplying fisheries resources. Nevertheless, in recent years, the bays have faced significant water quality issues and a decline in fishery production. These challenges are primarily driven by human activities such as overfishing and excessive nutrient loading, as well as climate change like global warming and increased extreme precipitation. Currently, studies on the water quality of the Ariake/Yatsushiro Sea predominantly rely on field measurements, while there is a relative dearth of research concerning climate-induced alterations in this region. Given the complex and changing estuarine conditions caused by climate change, conventional field measurements have limitations in capturing the complex and dynamic processes and predicting future changes. In contrast, modeling provides a practical approach to simulating complex dynamic processes and provides valuable insights into the complex interactions between climate factors and their effects on the marine ecosystem.

In this study, our primary objective was to evaluate the problem of declining water quality in the Ariake/Yatsushiro Sea, with a specific focus on the impact of extreme rainfall on DO levels. To achieve this, we employed a coupled numerical model, utilizing Delft3D, to simulate and analyze the impact of these weather events Furthermore, we analyzed water quality changes in the Ariake Sea spanning the last three decades and clarified the relationship between the effluent scale and the development of hypoxia. The specific aims of this study are detailed in the following points:

(1) To evaluate the impact of extreme summer precipitation, notably the 2020 Kyushu Floods, on hypoxia in the Ariake/Yatsushiro Sea, focusing on the vulnerability of DO levels to effluent events.

(2) To investigate the impact of stratification on hypoxia development and elucidate the relationship between river discharge and the duration of hypoxia in the Ariake Sea floor during the summer rainy season.

(3) To conduct a comprehensive analysis of long-term water quality alterations

in the Ariake Sea, emphasizing the impact of climate change, specifically addressing the escalating trend of hypoxia across diverse spatial scales.

1.3 Outline of the Thesis

The structure of this thesis is shown in Fig. 1.4.

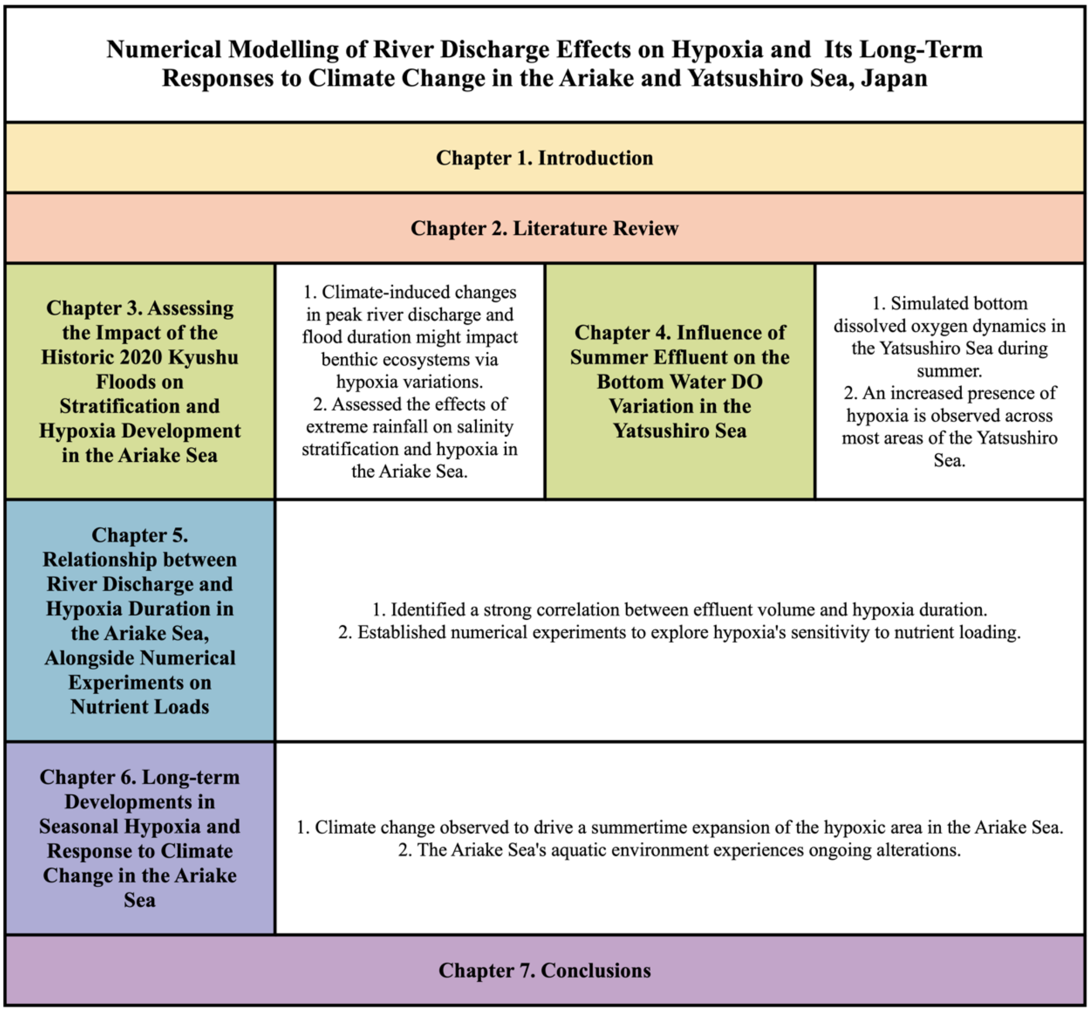

Numerical Modelling of River Discharge Effects on Hypoxia and Its Long-Term Responses to Climate Change in the Ariake and Yatsushiro Sea, Japan

Chapter 1. Introduction

Chapter 2. Literature Review

Chapter 3. Assessing the Impact of the Historic 2020 Kyushu Floods on Stratification and Hypoxia Development in the Ariake Sea	1. Climate-induced changes in peak river discharge and flood duration might impact benthic ecosystems via hypoxia variations. 2. Assessed the effects of extreme rainfall on salinity stratification and hypoxia in the Ariake Sea.	**Chapter 4. Influence of Summer Effluent on the Bottom Water DO Variation in the Yatsushiro Sea**	1. Simulated bottom dissolved oxygen dynamics in the Yatsushiro Sea during summer. 2. An increased presence of hypoxia is observed across most areas of the Yatsushiro Sea.
Chapter 5. Relationship between River Discharge and Hypoxia Duration in the Ariake Sea, Alongside Numerical Experiments on Nutrient Loads	1. Identified a strong correlation between effluent volume and hypoxia duration. 2. Established numerical experiments to explore hypoxia's sensitivity to nutrient loading.		
Chapter 6. Long-term Developments in Seasonal Hypoxia and Response to Climate Change in the Ariake Sea	1. Climate change observed to drive a summertime expansion of the hypoxic area in the Ariake Sea. 2. The Ariake Sea's aquatic environment experiences ongoing alterations.		

Chapter 7. Conclusions

Figure 1.4 Thesis structure.

References

AghaKouchak, A., Chiang, F., Huning, L. S., Love, C. A., Mallakpour, I., Mazdiyasni, O., Moftakhari, H., Papalexiou, S. M., Ragno, E., & Sadegh, M. (2020). Climate Extremes and Compound Hazards in a Warming World. *Annual Review of Earth and Planetary Sciences*, *48*(1), 519–548. https://doi.org/10.1146/annurev-earth-071719-055228

Azhikodan, G., & Yokoyama, K. (2018). Sediment transport and fluid mud layer formation in the macro-tidal Chikugo river estuary during a fortnightly tidal cycle. *Estuarine, Coastal and Shelf Science*, *202*, 232–245. https://doi.org/10.1016/j.ecss.2018.01.002

Breitburg, D., Levin, L. A., Oschlies, A., Grégoire, M., Chavez, F. P., Conley, D. J., Garçon, V., Gilbert, D., Gutiérrez, D., Isensee, K., Jacinto, G. S., Limburg, K. E., Montes, I., Naqvi, S. W. A., Pitcher, G. C., Rabalais, N. N., Roman, M. R., Rose, K. A., Seibel, B. A., … Zhang, J. (2018). Declining oxygen in the global ocean and coastal waters. *Science*, *359*(6371), eaam7240. https://doi.org/10.1126/science.aam7240

Conley, D. J., Carstensen, J., Ærtebjerg, G., Christensen, P. B., Dalsgaard, T., Hansen, J. L. S., & Josefson, A. B. (2007). LONG-TERM CHANGES AND IMPACTS OF HYPOXIA IN DANISH COASTAL WATERS. *Ecological Applications*, *17*(sp5), S165–S184. https://doi.org/10.1890/05-0766.1

Diaz, R. J. (2001). Overview of Hypoxia around the World. *Journal of Environmental Quality*, *30*(2), 275–281. https://doi.org/10.2134/jeq2001.302275x

Diaz, R. J., & Rosenberg, R. (1995). Marine benthic hypoxia: a review of its ecological effects and the behavioural responses of benthic macrofauna. *Oceanography and marine biology. An annual review*, *33*(245), 03.

Hagy, J. D., Boynton, W. R., Keefe, C. W., & Wood, K. V. (2004). Hypoxia in Chesapeake Bay, 1950-2001: Long-Term Change in Relation to Nutrient Loading and River Flow. *Estuaries*, *27*(4), 634–658.

Hayami, Y., Maeda, K., & Hamada, T. (2015). Long term variation in transparency in the inner area of Ariake Sea. *Estuarine, Coastal and Shelf Science*, *163*, 290–296.

https://doi.org/10.1016/j.ecss.2014.11.029

Hermanson, L., Smith, D., Seabrook, M., Bilbao, R., Doblas-Reyes, F., Tourigny, E., Lapin, V., Kharin, V. V., Merryfield, W. J., Sospedra-Alfonso, R., Athanasiadis, P., Nicoli, D., Gualdi, S., Dunstone, N., Eade, R., Scaife, A., Collier, M., O'Kane, T., Kitsios, V., … Kumar, A. (2022). WMO Global Annual to Decadal Climate Update: A Prediction for 2021–25. *Bulletin of the American Meteorological Society*, *103*(4), E1117–E1129. https://doi.org/10.1175/BAMS-D-20-0311.1

IPCC. (2014). Climate Change 2014: Synthesis Report. Contribution of Working Groups I, II and III to the Fifth Assessment Report of the Intergovernmental Panel on Climate Change [Core Writing Team, R.K. Pachauri and L.A. Meyer (eds.)]. *IPCC, Geneva, Switzerland*, 151 pp.

IPCC. (2018). Summary for Policymakers. In: Global Warming of 1.5°C. An IPCC Special Report on the impacts of global warming of 1.5°C above pre-industrial levels and related global greenhouse gas emission pathways, in the context of strengthening the global response to the threat of climate change, sustainable development, and efforts to eradicate poverty [Masson-Delmotte, V., P. Zhai, H.-O. Pörtner, D. Roberts, J. Skea, P.R. Shukla, A. Pirani, W. Moufouma-Okia, C. Péan, R. Pidcock, S. Connors, J.B.R. Matthews, Y. Chen, X. Zhou, M.I. Gomis, E. Lonnoy, T. Maycock, M. Tignor, and T. Waterfield (eds.)]. *Cambridge University Press, Cambridge, UK and New York, NY, USA*, pp. 3-24. https://doi.org/10.1017/9781009157940.001.

IPCC. (2023). Sections. In: Climate Change 2023: Synthesis Report. Contribution of Working Groups I, II and III to the Sixth Assessment Report of the Intergovernmental Panel on Climate Change [Core Writing Team, H. Lee and J. Romero (eds.)]. *IPCC, Geneva, Switzerland,* pp. 35-115, doi: 10.59327/IPCC/AR6-9789291691647

Jia, R., Lei, H., Hino, T., & Arulrajah, A. (2018). Environmental changes in Ariake Sea of Japan and their relationships with Isahaya Bay reclamation. *Marine Pollution Bulletin*, *135*, 832–844. https://doi.org/10.1016/j.marpolbul.2018.08.008

Kwiatkowski, L., Torres, O., Bopp, L., Aumont, O., Chamberlain, M., Christian, J. R., Dunne, J. P., Gehlen, M., Ilyina, T., John, J. G., Lenton, A., Li, H., Lovenduski,

N. S., Orr, J. C., Palmieri, J., Santana-Falcón, Y., Schwinger, J., Séférian, R., Stock, C. A., … Ziehn, T. (2020). Twenty-first century ocean warming, acidification, deoxygenation, and upper-ocean nutrient and primary production decline from CMIP6 model projections. *Biogeosciences*, *17*(13), 3439–3470. https://doi.org/10.5194/bg-17-3439-2020

Ministry of the Environment. (2017). Report of Ariake Sea / Yashiro Sea Comprehensive Survey and Evaluation Committee, Chapter 3 (in Japanese).

Murphy, R. R., Kemp, W. M., & Ball, W. P. (2011). Long-Term Trends in Chesapeake Bay Seasonal Hypoxia, Stratification, and Nutrient Loading. *Estuaries and Coasts*, *34*(6), 1293–1309. https://doi.org/10.1007/s12237-011-9413-7

Ni, X., Huang, D., Zeng, D., Zhang, T., Li, H., & Chen, J. (2016). The impact of wind mixing on the variation of bottom dissolved oxygen off the Changjiang Estuary during summer. *Journal of Marine Systems*, *154*, 122–130. https://doi.org/10.1016/j.jmarsys.2014.11.010

Rabalais, N. N., Díaz, R. J., Levin, L. A., Turner, R. E., Gilbert, D., & Zhang, J. (2010). Dynamics and distribution of natural and human-caused hypoxia. *Biogeosciences*, *7*(2), 585–619. https://doi.org/10.5194/bg-7-585-2010

Sasaki, K. (2017). *The Causality between the Isahaya Bay Reclamation Project and Declining Fisheries in the Ariake Sea*. *4*, 16–18.

Scanes, E., Scanes, P. R., & Ross, P. M. (2020). Climate change rapidly warms and acidifies Australian estuaries. *Nature Communications*, *11*(1), 1803. https://doi.org/10.1038/s41467-020-15550-z

Schmidtko, S., Stramma, L., & Visbeck, M. (2017). Decline in global oceanic oxygen content during the past five decades. *Nature*, *542*(7641), 335–339. https://doi.org/10.1038/nature21399

Simpson, J. H., & Sharples, J. (2012). *Introduction to the physical and biological oceanography of shelf seas*. Cambridge University Press.

Tabata, T., Hiramatsu, K., & Harada, M. (2015). Assessment of the Water Quality in the Ariake Sea Using Principal Component Analysis. *Journal of Water Resource and Protection*, *07*(01), 41–49. https://doi.org/10.4236/jwarp.2015.71003

Takikawa, K., Aoyama, C., Tanaka, K., Morimoto, K., & Watanabe, K. (2005). Characteristics of Environment in Yatsushiro Sea. *Asian and Pacific Coasts 2005, September 4-8, 2005, Jeju, Korea*, 1452–1463.

Thornton, P. K., Ericksen, P. J., Herrero, M., & Challinor, A. J. (2014). Climate variability and vulnerability to climate change: A review. *Global Change Biology*, *20*(11), 3313–3328. https://doi.org/10.1111/gcb.12581

Tishchenko, P. Ya., Lobanov, V. B., Zvalinsky, V. I., Sergeev, A. F., Koltunov, A., Mikhailik, T. A., Tishchenko, P. P., Shvetsova, M. G., Sagalaev, S., & Volkova, T. (2013). Seasonal Hypoxia of Amursky Bay in the Japan Sea: Formation and Destruction. *Terrestrial, Atmospheric and Oceanic Sciences*, *24*(6), 1033. https://doi.org/10.3319/TAO.2013.07.12.01(Oc)

Tsutsumi, H. (2006). Critical events in the Ariake Bay ecosystem: Clam population collapse, red tides, and hypoxic bottom water. *Plankton and Benthos Research*, *1*(1), 3–25. https://doi.org/10.3800/pbr.1.3

United Nations Environment Programme. (2023). *Emissions Gap Report 2023: Broken Record – Temperatures hit new highs, yet world fails to cut emissions (again)*. https://wedocs.unep.org/20.500.11822/43922

Wiseman, Wm. J., Rabalais, N. N., Turner, R. E., Dinnel, S. P., & MacNaughton, A. (1997). Seasonal and interannual variability within the Louisiana coastal current: Stratification and hypoxia. *Journal of Marine Systems*, *12*(1–4), 237–248. https://doi.org/10.1016/S0924-7963(96)00100-5

Yagi, Y., Kinoshita, I., Fujita, S., Aoyama, D., & Kawamura, Y. (2011). Importance of the upper estuary as a nursery ground for fishes in Ariake Bay, Japan. *Environmental Biology of Fishes*, *91*(3), 337–352. https://doi.org/10.1007/s10641-011-9790-6

Yu, L., Fennel, K., Laurent, A., Murrell, M. C., & Lehrter, J. C. (2015). Numerical analysis of the primary processes controlling oxygen dynamics on the Louisiana shelf. *Biogeosciences*, *12*(7), 2063–2076. https://doi.org/10.5194/bg-12-2063-2015

Zhang, J., Gilbert, D., Gooday, A., Levin, L., Naqvi, S. W. A., Middelburg, J. J., Scranton, M., Ekau, W., Pena, A., Dewitte, B., Oguz, T., Monteiro, P. M. S., Urbán, E., Rabalais, N. N., Ittekkot, V., Kemp, W. M., Ulloa, O., Elmgren, R., & Escobar-Briones, E. (2010). *Natural and human-induced hypoxia and consequences for coastal areas: Synthesis and future development*.

Zhang, W., Dunne, J. P., Wu, H., & Zhou, F. (2022). Regional projection of climate warming effects on coastal seas in east China. *Environmental Research Letters*, *17*(7), 074006. https://doi.org/10.1088/1748-9326/ac7344

Chapter 2

Literature Review

2.1 Potential Mechanisms of Hypoxia in Shallow Coastal Water

Dissolved oxygen (DO) concentration is a crucial indicator for assessing the well-being of aquatic ecosystems and is traditionally defined by a threshold of 2 mg/L, which serves as a fundamental benchmark for identifying oxygen-depleted conditions. When the DO concentration falls below 2 mg/L, it is classified as hypoxia (Diaz & Rosenberg, 1995). Ritter and Montagna (1999) and Tokunaga et al. (2009) defined hypoxia as 3 mg/L through the assessment of long-term changes in DO concentration, which is better adapted to the local ecosystem dynamics. Worldwide recognition of DO deterioration has risen since the middle of the 20th century (Diaz & Rosenberg, 2008). There are increasing reports of hypoxic events from marine ecosystems around the world. *e.g.*, Baltic Sea (Conley et al., 2002), Gulf of Mexico (Turner et al., 2005), Texas-Louisiana Shelf (Wiseman et al., 1997), Chesapeake Bay (Hagy et al., 2004) and East China Sea (Chen et al., 2007). In Japan, hypoxia has been identified as a significant environmental issue in the semi-enclosed shallow bays since the 1970s (Suzuki, 2001), *e.g.*, Tokyo Bay (Kodama & Horiguchi, 2011), Ise Bay (Fujiwara et al., 2002) and Mikawa Bay (Suzuki & Matsukawa, 1987). However, the dominant factors triggering hypoxia can exhibit considerable variation due to the complex estuary morphology and circulation (Rabouille et al., 2008). As shown in Fig. 2.1, numerous external factors and processes can contribute to and exacerbate the occurrence of hypoxia in coastal waters, including warming, stratification, nutrient loading, land-use changes, overfishing, and wind (Jackson et al., 2001; Levin et al., 2009; Hallett et al., 2018; Wang et al., 2022).

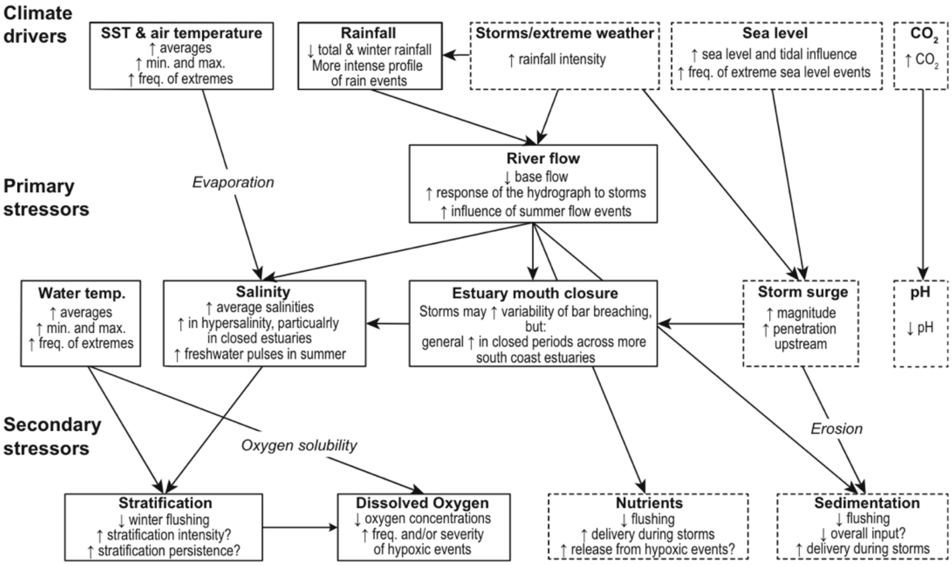

Figure 2.1 Conceptual diagram of key climatic drivers and their effects on the primary and secondary environmental stressors of the estuaries. (Dashed boxes indicate drivers and effects whose direction and/or magnitude of change is less certain or considered to be less significant) (Hallett et al., 2018)

Rising surface water temperatures and the frequent occurrence of extreme warming events caused by climate change are some of the causes of coastal hypoxia. From a biochemical control perspective, water temperature plays a crucial role in regulating the metabolism of aquatic organisms and influencing the biological population distribution of aquatic communities. During summer, increased water temperatures can foster the growth of fish and plankton, consequently increasing the consumption of DO (Roman et al., 2019). From a physical control perspective, the rise in water temperatures may result in a decrease in the DO saturation of the water, diminishing its capacity to DO effectively (Du et al., 2018). In addition, warmer water temperatures leading to thermal stratification can impede or disrupt the typical mixing or circulation of water (Wang et al., 2017). Thus, the intricate interplay between biochemical controls and physical factors bears substantial implications for the dynamics of DO in marine ecosystems.

Salinity-driven stratification induced by freshwater inflow plays a pivotal role in the development of hypoxia in the majority of coastal seas. As freshwater, often rich in nutrients, enters coastal areas, it establishes a stratification gradient, resulting in distinct layers with varying salinity levels. This stratification creates relatively stable water layers, hindering the replenishment of upper oxygen to the lower layers (Wiseman et al., 1997; Murphy et al., 2011). Simultaneously, organic matter, such as decomposing phytoplankton and detritus, tends to sink into the lower layers, contributing to oxygen reduction in the bottom layers (Wiseman et al., 1997). Limited vertical mixing leads to oxygen consumption surpassing replenishment, resulting in reduced oxygen levels and the establishment of hypoxic or anoxic conditions.

Meanwhile, nutrient loads typically associated with river inflows play a pivotal role in marine ecosystems. On one hand, the increase in nutrients stimulates the growth and subsequent decay of phytoplankton, resulting in excessive oxygen consumption (Malone et al., 1988). On the other hand, the excessive input of nitrogen and phosphorus contributes to a reduction in oxygen content in the bottom water body Kemp et al., 2009). Under hypoxic and anoxic conditions, the denitrification process in the nitrogen cycle intensifies, and organic phosphorus is more readily released from the sediment. Therefore, the development of hypoxia is intricately linked to nutrient cycling in the ecosystem (Kemp et al., 2005).

Certain factors have been identified as contributors to the distribution of DO. For instance, upwelling-favorable winds can induce upwelling, bringing deep water to the surface and altering the distribution of water temperature, salinity, and DO (Feng et al., 2014). Additionally, storm surges play a crucial role in enhancing turbulent mixing and disrupting stratification, thereby facilitating improved oxygen transport (Li et al., 2006).

These factors collectively contribute to the development of hypoxia, exhibiting varying degrees of dominance in complex coastal physical environments and ecosystems. Therefore, conducting in-depth research on the factors that significantly influence hypoxia is crucial, serving as a foundation for the development of adaptive policies.

2.2 Challenges in the Ariake/Yatsushiro Sea

Since the 1990s, the Ariake Sea has grappled with severe environmental and ecosystem challenges, culminating in substantial reductions in yield and ecosystem collapse. These challenges include weakened water purification ability, sediment accumulation on the seafloor, frequent occurrences of red tides, and the development of hypoxia (Nakata et al., 2009; Wang et al., 2017). These environmental disturbances had profound effects on fisheries, notably manifesting in the slowed growth and increased mortality of benthic communities, with the Manila clam (*Ruditapes philippinarum*) being particularly affected (Tsutsumi, 2006; Tsutsumi et al., 2015).

A contributing factor to these challenges may arise from coastal development activities, particularly the reclamation and dam construction in Isahaya Bay, part of the Ariake Bay estuary, further exacerbating these issues (Tsutsumi, 2006; Wang et al., 2017). The reclamation of Isahaya Bay directly led to the reduction of tidal flats, disrupting the living environment for benthic organisms. Additionally, it resulted in a decrease in tide and tidal current, altering sediment quality, intensifying stratification, and causing a reduction in dissolved oxygen levels (Hodoki & Murakami, 2006; Wang et al., 2017; Kim et al., 2018).

Climate change could be a significant factor contributing to the alterations in the Ariake/Yatsushiro Sea. In recent decades, there has been a notable increase in the occurrence of large-scale red tide events, inflicting considerable damage on cultured Nori (Tsutsumi, 2006). Concurrently, bottom hypoxia in the inner bay of the Ariake Sea has extensively expanded (Wang et al., 2017). These phenomena typically emerge after the rainy season. Heavy rainfall, leading to significant inflows of freshwater, triggers stratification and hinders the exchange of water columns, ultimately resulting in hypoxia (Stanley & Nixon, 1992). Moreover, the excessive loading of nutrients can further augment the proliferation of red tide events (Tsutsumi, 2021).

The ecological and environmental issues confronting the Ariake/Yatsushiro Sea have garnered considerable attention. However, the intricate nature of its aquatic environment necessitates extensive and sustained investigation for a comprehensive understanding. Hence, a thorough examination of the long-term changes in the Ariake Sea becomes imperative to formulate a more holistic approach to safeguarding and restoring the ecological equilibrium of marine ecosystems.

2.3 Application of Numerical Models

Currently, the primary approaches for investigating physical and ecological processes in coastal oceans encompass field monitoring, numerical simulation, and remote sensing technology. Numerical simulation stands out for its capacity to deliver high spatial and temporal resolution, along with the flexibility of processing at various scales through multi-scenario simulations. Developing numerical models serves as a pivotal tool in enhancing the comprehension of the intricate physical and ecological processes within complex coastal waters. Through the simulation and analysis of diverse interactions in marine systems, models offer an effective means to unveil the complexities inherent in both the physical dynamics and ecosystem interactions of coastal waters.

This study employed the open-source numerical simulation software package, Delft3D, which incorporates the FLOW and WAQ modules developed by Deltares. Delft3D is a robust and efficient modeling tool for simulating hydrodynamics and water quality in coastal and estuarine waters and has been successfully applied to multiple aquatic systems (Bai et al., 2022), such as Yangtze Estuary and Breton Sound Estuary (Chen et al., 2015; Wang et al., 2017).

In previous research, Wang et al. (2017) utilized the general hydrodynamic model calculated by Delft3D for numerical experiments on nonlinear tides and fine-grained sediment transport in the Ariake Sea and Yatsushiro Sea. This confirmed the nonlinear characteristics of tides. Tadokoro et al. (2020) employing a general 3D hydrodynamic model and a 1D DO transport model, evaluated the effects of thermal stratification and DO in the Ariake Sea. The study concluded that temperature changes are a significant factor influencing thermal stratification and changes in dissolved oxygen distribution. They explored the effects of temperature and river flow changes on dissolved oxygen distribution under specific conditions after global warming through numerical experiments. The results indicated that rising air temperatures, increasing river temperatures, and elevated ocean temperatures exert the most significant impact on hypoxic waters. In the Yatsushiro Sea, the dynamics of seawater carbon dioxide (CO_2) have been assessed using Delft3D, demonstrating the model's proficiency in simulating CO_2 pressure (Xiong et al., 2022).

References

Bai, J., Zhao, J., Zhang, Z., & Tian, Z. (2022). Assessment and a review of research on surface water quality modeling. *Ecological Modelling*, *466*, 109888. https://doi.org/10.1016/j.ecolmodel.2022.109888

Chen, C.-C., Gong, G.-C., & Shiah, F.-K. (2007). Hypoxia in the East China Sea: One of the largest coastal low-oxygen areas in the world. *Marine Environmental Research*, *64*(4), 399–408. https://doi.org/10.1016/j.marenvres.2007.01.007

Chen, X., Shen, Z., Li, Y., & Yang, Y. (2015). Physical controls of hypoxia in waters adjacent to the Yangtze Estuary: A numerical modeling study. *Marine Pollution Bulletin*, *97*(1–2), 349–364. https://doi.org/10.1016/j.marpolbul.2015.05.067

Conley, D. J., Humborg, C., Rahm, L., Savchuk, O. P., & Wulff, F. (2002). Hypoxia in the Baltic Sea and Basin-Scale Changes in Phosphorus Biogeochemistry. *Environmental Science & Technology*, *36*(24), 5315–5320. https://doi.org/10.1021/es025763w

Diaz, R. J., & Rosenberg, R. (1995). Marine benthic hypoxia: a review of its ecological effects and the behavioural responses of benthic macrofauna. *Oceanography and marine biology. An annual review*, *33*(245), 03.

Diaz, R. J., & Rosenberg, R. (2008). Spreading Dead Zones and Consequences for Marine Ecosystems. *Science*, *321*(5891), 926–929. https://doi.org/10.1126/science.1156401

Du, J., Shen, J., Park, K., Wang, Y. P., & Yu, X. (2018). Worsened physical condition due to climate change contributes to the increasing hypoxia in Chesapeake Bay. *Science of The Total Environment*, *630*, 707–717. https://doi.org/10.1016/j.scitotenv.2018.02.265

Feng, Y., Fennel, K., Jackson, G. A., DiMarco, S. F., & Hetland, R. D. (2014). A model study of the response of hypoxia to upwelling-favorable wind on the northern Gulf of Mexico shelf. *Journal of Marine Systems*, *131*, 63–73. https://doi.org/10.1016/j.jmarsys.2013.11.009

Fujiwara, T., Takahashi, T., Kasai, A., Sugiyama, Y., & Kuno, M. (2002). The Role of Circulation in the Development of Hypoxia in Ise Bay, Japan. *Estuarine, Coastal* *and Shelf Science*, *54*(1), 19–31. https://doi.org/10.1006/ecss.2001.0824

Hagy, J. D., Boynton, W. R., Keefe, C. W., & Wood, K. V. (2004). Hypoxia in Chesapeake Bay, 1950-2001: Long-Term Change in Relation to Nutrient Loading and River Flow. *Estuaries*, *27*(4), 634–658.

Hallett, C. S., Hobday, A. J., Tweedley, J. R., Thompson, P. A., McMahon, K., & Valesini, F. J. (2018). Observed and predicted impacts of climate change on the estuaries of south-western Australia, a Mediterranean climate region. *Regional Environmental Change*, *18*(5), 1357–1373. https://doi.org/10.1007/s10113-017-1264-8

Hodoki, Y., & Murakami, T. (2006). Effects of tidal flat reclamation on sediment quality and hypoxia in Isahaya Bay. *Aquatic Conservation: Marine and Freshwater Ecosystems*, *16*(6), 555–567. https://doi.org/10.1002/aqc.723

Jackson, J. B. C., Kirby, M. X., Berger, W. H., Bjorndal, K. A., Botsford, L. W., Bourque, B. J., Bradbury, R. H., Cooke, R., Erlandson, J., Estes, J. A., Hughes, T. P., Kidwell, S., Lange, C. B., Lenihan, H. S., Pandolfi, J. M., Peterson, C. H., Steneck, R. S., Tegner, M. J., & work(s):, R. R. W. R. (2001). Historical Overfishing and the Recent Collapse of Coastal Ecosystems. *Science, New Series*, *293*(5530), 629–638.

Kemp, W., Boynton, W., Adolf, J., Boesch, D., Boicourt, W., Brush, G., Cornwell, J., Fisher, T., Glibert, P., Hagy, J., Harding, L., Houde, E., Kimmel, D., Miller, W., Newell, R., Roman, M., Smith, E., & Stevenson, J. (2005). Eutrophication of Chesapeake Bay: Historical trends and ecological interactions. *Marine Ecology Progress Series*, *303*, 1–29. https://doi.org/10.3354/meps303001

Kemp, W. M., Testa, J. M., Conley, D. J., Gilbert, D., & Hagy, J. D. (2009). Temporal responses of coastal hypoxia to nutrient loading and physical controls. *Biogeosciences*, *6*(12), 2985–3008. https://doi.org/10.5194/bg-6-2985-2009

Kim, S., Hayami, Y., Tai, A., & Tada, A. (2018). The mechanism of bottom water DO variation in summer at the northern mouth of Isahaya Bay, Japan. *Journal of Oceanography*, *74*(6), 595–605. https://doi.org/10.1007/s10872-018-0467-z

Kodama, K., & Horiguchi, T. (2011). Effects of hypoxia on benthic organisms in

Tokyo Bay, Japan: A review. *Marine Pollution Bulletin*, *63*(5–12), 215–220. https://doi.org/10.1016/j.marpolbul.2011.04.022

Levin, L. A., Ekau, W., Gooday, A. J., Jorissen, F., Middelburg, J. J., Naqvi, S. W. A., Neira, C., Rabalais, N. N., & Zhang, J. (2009). *Effects of natural and human-induced hypoxia on coastal benthos*.

Li, M., Zhong, L., Boicourt, W. C., Zhang, S., & Zhang, D.-L. (2006). Hurricane-induced storm surges, currents and destratification in a semi-enclosed bay. *Geophysical Research Letters*, *33*(2), L02604. https://doi.org/10.1029/2005GL024992

Malone, T., Crocker, L., Pike, S., & Wendler, B. (1988). Influences of river flow on the dynamics of phytoplankton production in a partially stratified estuary. *Marine Ecology Progress Series*, *48*, 235–249. https://doi.org/10.3354/meps048235

Murphy, R. R., Kemp, W. M., & Ball, W. P. (2011). Long-Term Trends in Chesapeake Bay Seasonal Hypoxia, Stratification, and Nutrient Loading. *Estuaries and Coasts*, *34*(6), 1293–1309. https://doi.org/10.1007/s12237-011-9413-7

Nakata, H., Mishina, H., Takahashi, T., & Hirano, K. (2009). *A Newly Emerging Environmental Issue: Development of Hypoxia in the Bottom Water of Ariake Bay*.

Rabouille, C., Conley, D. J., Dai, M. H., Cai, W.-J., Chen, C. T. A., Lansard, B., Green, R., Yin, K., Harrison, P. J., Dagg, M., & McKee, B. (2008). Comparison of hypoxia among four river-dominated ocean margins: The Changjiang (Yangtze), Mississippi, Pearl, and Rhône rivers. *Continental Shelf Research*, *28*(12), 1527–1537. https://doi.org/10.1016/j.csr.2008.01.020

Ritter, C., Montagna, P.A. (1999). Seasonal Hypoxia and Models of Benthic Response in a Texas Bay. *Estuaries 22*, 7. https://doi.org/10.2307/1352922

Roman, M. R., Brandt, S. B., Houde, E. D., & Pierson, J. J. (2019). Interactive Effects of Hypoxia and Temperature on Coastal Pelagic Zooplankton and Fish. *Frontiers in Marine Science*, *6*, 139. https://doi.org/10.3389/fmars.2019.00139

Stanley, D. W., & Nixon, S. W. (1992). Stratification and Bottom-Water Hypoxia in the Pamlico River Estuary. *Estuaries*, *15*(3), 270.

https://doi.org/10.2307/1352775

Suzuki, T. (2001). Oxygen-Deficient Waters along the Japanese Coast and Their Effects upon the Estuarine Ecosystem. *Journal of Environmental Quality*, *30*(2), 291–302. https://doi.org/10.2134/jeq2001.302291x

Suzuki, T., & Matsukawa, Y. (1987). Hydrography and budget of dissolved total nitrogen and dissolved oxygen in the stratified season in Mikawa Bay, Japan. *Journal of the Oceanographical Society of Japan*, *43*(1), 37–48. https://doi.org/10.1007/BF02110632

Tadokoro, M., & Yano, S. (2019). Evaluation of Effects of Temperature and River Discharge Changes Due to Climate Change on Hypoxia in the Ariake Sea. *Journal of Japan Society of Civil Engineers, Ser. B2 (Coastal Engineering), 75*(2), I_1231-I_1236. https://doi.org/10.2208/kaigan.75.I_1231

Tadokoro, M., Yano, S., Peizhi, Q., & Orrheim, L. (2020). Effects of change of density stratification due to Isahaya Sea-Dyke on the fate of anoxic water in the Ariake Sea. *IOP Conference Series: Earth and Environmental Science*, *419*(1), 012161. https://doi.org/10.1088/1755-1315/419/1/012161

Tokunaga T., Kodama M., Kimoto K., Shibahara Y. (2009). Characteristics of hypoxia in the inner western area of Ariake Bay. J. *Jpn. Soc. Civ. Eng. Ser B2 Coast. Eng. 65*, 1011–1015. https://doi.org/10.2208/kaigan.65.1011

Tsutsumi, H. (2006). Critical events in the Ariake Bay ecosystem: Clam population collapse, red tides, and hypoxic bottom water. *Plankton and Benthos Research*, *1*(1), 3–25. https://doi.org/10.3800/pbr.1.3

Tsutsumi H. (2021). Mechanisms of ecosystem crisis originated in frequent occurrence of red tides in Ariake Bay. *Japanese Journal of Benthology*, *76*(0), 103–127. https://doi.org/10.5179/benthos.76.103

Tsutsumi, H., Takamatsu, A., Nagata, S., Orita, R., Umehara, A., Komorita, T., Shibanuma, S., Takahashi, T., Komatsu, T., & Montani, S. (2015). Implications of changes in the benthic environment and decline of macro-benthic communities in the inner part of Ariake Bay in relation to seasonal hypoxia. *Plankton and*

Benthos Research, *10*(4), 187–201. https://doi.org/10.3800/pbr.10.187

Turner, R. E., Rabalais, N. N., Swenson, E. M., Kasprzak, M., & Romaire, T. (2005). Summer hypoxia in the northern Gulf of Mexico and its prediction from 1978 to 1995. *Marine Environmental Research*, *59*(1), 65–77. https://doi.org/10.1016/j.marenvres.2003.09.002

Wang, H., Chen, Q., Hu, K., & La Peyre, M. K. (2017). A Modeling Study of the Impacts of Mississippi River Diversion and Sea-Level Rise on Water Quality of a Deltaic Estuary. *Estuaries and Coasts*, *40*(4), 1028–1054. https://doi.org/10.1007/s12237-016-0197-7

Wang, K., Yao, J., Wang, J., Liu, H., & Yin, K. (2022). Role of Winds in Interrupting the Formation of Coastal Hypoxia. *Frontiers in Marine Science*, *9*, 839812. https://doi.org/10.3389/fmars.2022.839812

Wiseman, Wm. J., Rabalais, N. N., Turner, R. E., Dinnel, S. P., & MacNaughton, A. (1997). Seasonal and interannual variability within the Louisiana coastal current: Stratification and hypoxia. *Journal of Marine Systems*, *12*(1–4), 237–248. https://doi.org/10.1016/S0924-7963(96)00100-5

Xiong, B., Yano, S., Komai, K., Saito, N., Komori, H., Chi, B., Hao, L., & Nakayama, K. (2022). Interaction between seawater carbon dioxide dynamics and stratification in shallow coastal waters: A preliminary study based on a weekly validated three-dimensional ecological model. *Frontiers in Marine Science*, *9*, 991802. https://doi.org/10.3389/fmars.2022.991802

Chapter 3

Assessing the Impact of the Historic 2020 Kyushu Floods on Stratification and Hypoxia Development in the Ariake Sea

3.1 Introduction

Dissolved Oxygen (DO) plays a vital role in the material circulation of marine ecosystems. According to the latest special report of the IPCC, oxygen depletion has emerged as a significant concern attributed to both human activities and climate-related threats (IPCC, 2018). Hypoxia can be defined as DO less than 3 mg/L and occurs as a combined result of biochemically controlled DO consumption and physically controlled limited oxygen replenishment (Du et al., 2018). The altered precipitation patterns due to climate change significantly affect river regimes across various basins, particularly the intensity of summer river flows (Abeysingha et al., 2020; Kundzewicz et al., 2015), and stand as one of the primary causes of oxygen depletion in most coastal areas (Rabalais et al., 2010).

Extreme rainfall events, a consequence of climate change, have become more frequent in recent years, causing significant negative impacts on coastal economies and marine ecosystems (Easterling et al., 2000). The IPCC 2018 Special Report suggests a high probability of increased mean precipitation in the mid-latitude land areas of the Northern Hemisphere since 1951 due to climate change (IPCC, 2018). The intensified and prolonged rainfall from extreme rainfall events presents considerable challenges, including flooding, soil erosion, and infrastructure damage (Wang et al., 2017; Osburn et al., 2019). Heavy rainfall often triggers substantial runoff, carrying pollutants, sediments, and nutrients from the land surface into coastal and marine environments. This influx exacerbates water quality deterioration along coastal waters, intensifying issues like eutrophication and hypoxia (Tishchenko et al., 2013; Sinha et al., 2017). Simultaneously, it can arouse soil erosion, impacting agricultural lands and various ecosystems (Knapp et al., 2008).

The Ariake Sea is one of the most important shallow coastal areas for fisheries and seaweed production, generating 40% of the total cultured Nori (seaweed) in Japan, and is considered one of the Regions of Freshwater Influence (ROFIs). The eight main A-class rivers, serving as the primary sources of freshwater inflow, play a critical role in the marine environment and benthic ecosystem of the bay. The Chikugo River is the largest river at the head of the bay, with a watershed area of approximately 2,863 km^2. The Chikugo River basin accounts for 42% of the total combined watershed area of major rivers flowing into the Ariake Sea and contributes an average annual discharge of 94 m^3/s into the bay. Over the last 50 years, the Chikugo River, classified as one of the A-class rivers, has exhibited a consistent upward trend in its annual maximum daily discharge (Fig. 3.1). In the 2020 Kyushu Floods, particularly, the large-scale effluent caused by heavy rainfall occurred from July 5 to July 7 in the Chikugo River basin. The water level obtained at the Senoshita Observatory located downstream of the river (6.95 m at 13:00 on July 7) became the highest water level in the past years and the estimated maximum daily discharge reached 6,590 m^3/s, which exceeded the past 20 years (MLIT, 2020). Large-scale effluent may be extremely detrimental to the coastal physical environment and the bottom fauna habitats of the bay. According to the records of the Kyushu Regional Agricultural Administration Office (2019), the influx of freshwater caused the development of density stratification and the occurrence of the hypoxic water mass for a long period in the Northern Ariake Sea and Isahaya Bay. Extreme rainfall events have resulted in a significant influx of freshwater into the Ariake Sea, potentially causing a decrease in surface layer salinity and an increase in water column stability (Yano et al., 2014). Concurrently, this large-scale freshwater influx has induced density stratification, a significant factor contributing to the development of hypoxia in the bottom layer (Scully, 2013).

This study aims to assess the effects of extreme rainfall events on hypoxia in the Ariake Sea, utilizing numerical models calculated by Delft3D. Additionally, the results are compared with five other cases to elucidate variations in hypoxia resulting from different flood patterns. The objective is to lay the groundwork for informed coastal area management and to devise strategies for adapting to climate change.

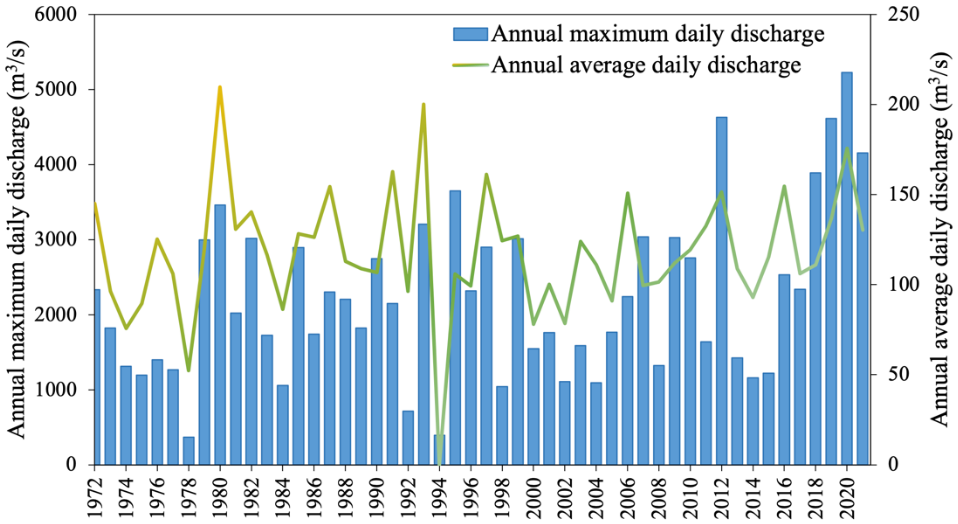

Figure 3.1 The annual maximum discharge and annual average discharge in the Chikugo River over the past five decades.

3.2 Hydrodynamic Model

This study utilized a generalized coastal three-dimensional hydrodynamic model developed by (Yano et al., 2010) and executed through the Delft3D-FLOW module. The Delft3D-FLOW module is a multi-dimensional (2D or 3D) hydrodynamic and transport simulation program designed to compute non-steady flow and transport phenomena. It considers tidal and meteorological influences on a curvilinear, boundary-fitted grid, or spherical coordinates. Its applications include assessing hydraulic structure stability, salt intrusion, pollutant dispersion, and sediment transport. In this section, we elucidate the mathematical principles supporting the Delft3D-FLOW module and outline the basic structure of the calculation area.

3.2.1 Hydrodynamic equations

The fundamental mathematical principle behind the hydrodynamic model Delft3D-FLOW involves solving the Navier-Stokes equations for incompressible fluids, utilizing the finite difference method under shallow water assumptions (Deltares, 2017). In this section, we present the continuity equation and momentum equations to elucidate this process.

The continuity equation and momentum equations for three-dimensional flow are given by:

$$\frac{\partial \rho}{\partial t} + \frac{\partial(\rho U)}{\partial x} + \frac{\partial(\rho V)}{\partial y} + W\frac{\partial(\rho W)}{\partial z} = 0 \qquad (3.1)$$

and

$$\frac{\partial U}{\partial t} + U\frac{\partial U}{\partial x} + V\frac{\partial U}{\partial y} + W\frac{\partial U}{\partial z} - fV = -\frac{1}{\rho}\frac{\partial p}{\partial x} + \frac{1}{\rho}\left(\frac{\partial}{\partial x}\tau_{xx} + \frac{\partial}{\partial y}\tau_{yx} + \frac{\partial}{\partial z}\tau_{zx}\right) \qquad (3.2)$$

$$\frac{\partial V}{\partial t} + U\frac{\partial V}{\partial x} + V\frac{\partial V}{\partial y} + W\frac{\partial V}{\partial z} + fU = -\frac{1}{\rho}\frac{\partial p}{\partial y} + \frac{1}{\rho}\left(\frac{\partial}{\partial x}\tau_{xy} + \frac{\partial}{\partial y}\tau_{yy} + \frac{\partial}{\partial z}\tau_{zy}\right) \qquad (3.3)$$

$$\frac{\partial W}{\partial t} + U\frac{\partial W}{\partial x} + V\frac{\partial W}{\partial y} + W\frac{\partial W}{\partial z} = -g - \frac{1}{\rho}\frac{\partial p}{\partial z} + \frac{1}{\rho}\left(\frac{\partial}{\partial x}\tau_{xz} + \frac{\partial}{\partial y}\tau_{yz} + \frac{\partial}{\partial z}\tau_{zz}\right) \qquad (3.4)$$

where x and y represent the horizontal coordinate system, while z denotes the vertical coordinate system (with upward direction as positive), t stands for time, and v signifies the flow velocity vector (= (U, V, W)). Here, $U(x, y, z, t)$, $V(x, y, z, t)$, and $W(x, y, z, t)$ denote the flow velocity components in the x, y, and z directions respectively. The pressure is denoted by $p(x, y, z, t)$, and the density by $\rho(x, y, z, t)$. Additionally, terms such as τ_{xx} (x, y, z, t), etc., represent stress tensor. g is acceleration due to gravity (m/s^2). f is Coriolis frequency (1/s) and is defined by:

$$f = 2\omega \sin \phi \qquad (3.5)$$

where ω is the angular velocity of Earth's rotation (= 7.292 $\times 10^{-5}$ s^{-1}) and ϕ is the latitude.

3.2.2 Heat flux models

Delft3D-FLOW models the heat exchange at the free surface by considering the distinct effects of solar (short wave) and atmospheric (long wave) radiation, as well as heat loss due to back radiation, evaporation, and convection. Within the literature, there exists significant variability in empirical formulations used to calculate these heat fluxes across the sea surface. The differences in these formulations primarily stem from variations in the dependency of heat exchange on meteorological parameters like wind speed, cloud cover, and humidity. Fig. 3.2 schematically illustrates the radiation process along with the mechanisms of heat flux at the water surface.

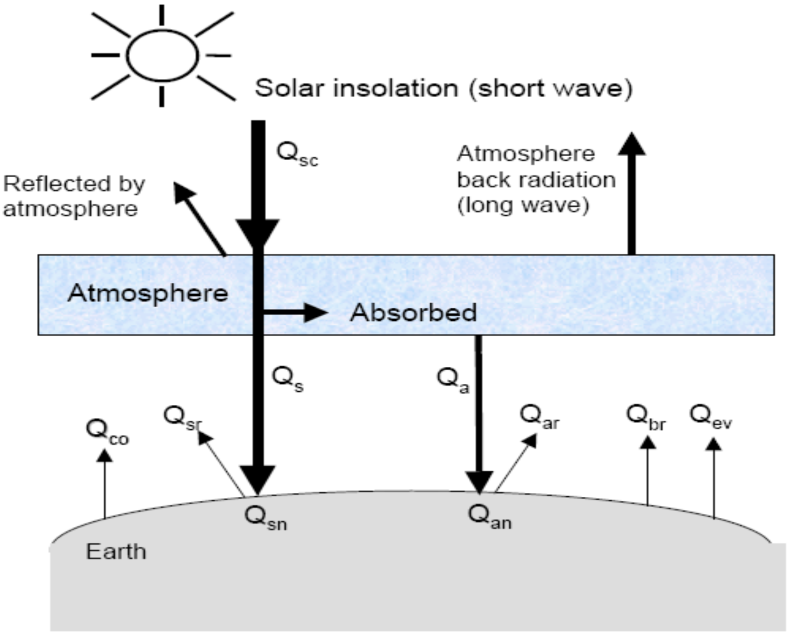

Figure 3.2 The heat flux mechanisms at the water surface

The total heat flux (Q_{tot}) through the free surface is defined by:

$$Q_{tot} = Q_{sn} + Q_{an} - Q_{br} - Q_{ev} - Q_{co} \tag{3.6}$$

where Q_{sn} is net incident solar radiation (short wave), Q_{an} is net incident atmospheric radiation (long wave), Q_{br} is back radiation (long wave), Q_{ev} is evaporative heat flux (latent heat) and Q_{co} is convective heat flux (sensible heat). The unit is J/m^2/s.

3.2.3 Coordinate system

In this model, the horizontal grid takes the form of a rectangular grid with a Cartesian frame of reference (Deltares, 2017). The vertical grid system employs a σ-coordinate system, comprising layers bounded by two σ-planes. These planes, while not strictly horizontal, conform to both the bottom topography and the free surface (Fig. 3.3). The σ-grid is fitted to both the bottom and the dynamic free surface, enabling a smooth representation of the topography. Consequently, although the number of σ-layers remains consistent across the domain, their thickness varies in relation to the depth (Deltares, 2017).

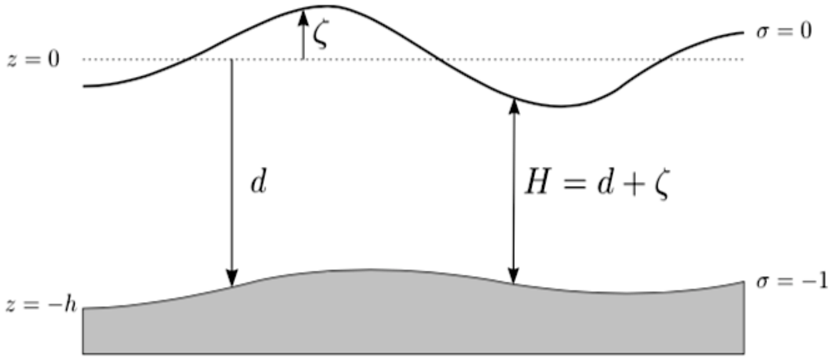

Figure 3.3 Definition of water level (*ζ*), depth (*h*) and total depth (*H*)

The σ coordinate system is defined as:

$$\sigma = \frac{z-\zeta}{d+\zeta} = \frac{z-\zeta}{H} \tag{3.7}$$

where z is the vertical coordinate in physical space, ζ is the free surface elevation above the reference plane (at z = 0) and d is the depth below the reference plane. H is the total water depth, given by

$$H = d + \zeta \tag{3.8}$$

The values of σ are set at $\sigma = 0$ for the free surface and $\sigma = -1$ at the bottom (Deltares, 2017). Previous research verification indicates that simulation results remain highly consistent even with an increase in the number of σ-layers beyond ten. Consequently, in this model, the number of σ-layers is fixed at ten, distributed as 5% × 3, 10% × 4, and 15% × 3 from surface to bottom.

3.2.4 Basic setting of the hydrodynamic model

This study employed a generalized 3D hydrodynamic model developed by (Yano et al., 2010) to simulate the physical conditions within the Ariake Sea. The simulation domain encompassed both the Ariake Sea and the Yatsushiro Sea, employing a horizontal resolution of 10” (Δx =250 m), as shown in Fig. 3.4. The calculation period for each year spanned from April 1st to October 31st, with a time step of 2 minutes.

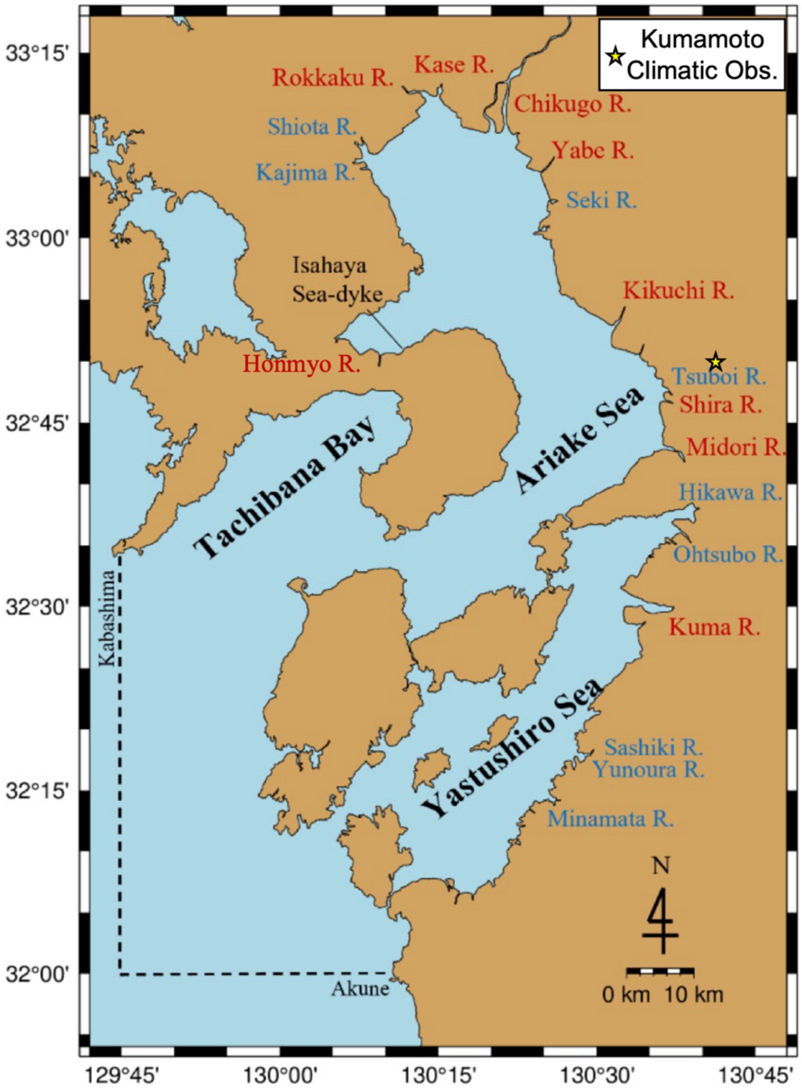

Figure 3.4 Calculation domain and open boundaries of the hydrodynamic model. Red and blue letters represent class A and class B rivers, respectively.

The physical parameters within this model include constants, roughness, viscosity, and others. The roughness formula employed in this model utilizes Chezy, with values of 80 $m^{1/2}/s$ in both the u-direction and v-direction. Additionally, the SGS (Sub-Grid Scale) model assesses horizontal eddy viscosity and eddy diffusion coefficients for the horizontal direction. Meanwhile, for the vertical direction, the model incorporates the k-ε model, determining the coefficients by transport equations for both turbulent kinetic energy and turbulent kinetic energy dissipation to evaluate vertical turbulent eddy viscosity and eddy diffusivity.

The heat flux model employs the Murakami model, which defines parameters such as relative humidity, air temperature, and net (short-wave) solar radiation. The data, encompassing temperature, humidity, radiation, and wind, are sourced from the Kumamoto observatory within the AMeDAS Observatory under the Japan Meteorological Agency.

The open boundaries, positioned outside the inlet to the Ariake Sea and along the line connecting Kabashima Suido and Akune (Fig. 3.4), represent cross-sections characterized by non-zero flow. Consequently, values for the concentration of state variables need to be specified at each time step (Deltares, 2017). To establish these boundaries, the amplitude and phase were fine-tuned exclusively for the four primary tidal components (M_2, S_2, K_1, O_1), out of a total of 40 tidal components, based on the existing harmonic constants at both ends. These harmonic constants, originally outlined by Yano et al. (2010), are referred to for guidance. The specific amplitudes and phases at the open boundary ends are detailed in Table 3.1, with linear interpolation applied between these ends.

Table 3.1 The amplitudes and phases at both ends of the open boundary.

Station/tidal components		
Akune	**Amplitude (cm)**	**Phase (°)**
M_2	71.7	211
S_2	31.4	229
K_1	22.9	209
O_1	17.7	185
Kabashima Suido	**Amplitude**	**Phase (°)**
M_2	86	219
S_2	36	240
K_1	25	205
O_1	19	186

This study accounts for freshwater inflows from eight A-class rivers (Chikugo River, Yabe River, Kase River, Rokkaku River, Kikuchi River, Shira River, Midori River, Kuma River), nine B-class rivers (Kashima River, Shiota River, Seki River, Tsuboi River, Hikawa, Otsubo River, Sashiki River, Yunoura River, Mizumata River), and the north-south drainage gates of Isahaya Bay. To include downstream discharge from the observatory, adjustments will be made to the observed discharge using the following equation:

$$Q_{(\mathrm{A-class})} = Q_0 \times \frac{A_2}{A_1} \tag{3.9}$$

where Q is the discharge of A-class rivers, Q_0 is the discharge from the observatory, A_1 and A_2 are observatory catchment area and total river area, respectively (Fig. 3.5).

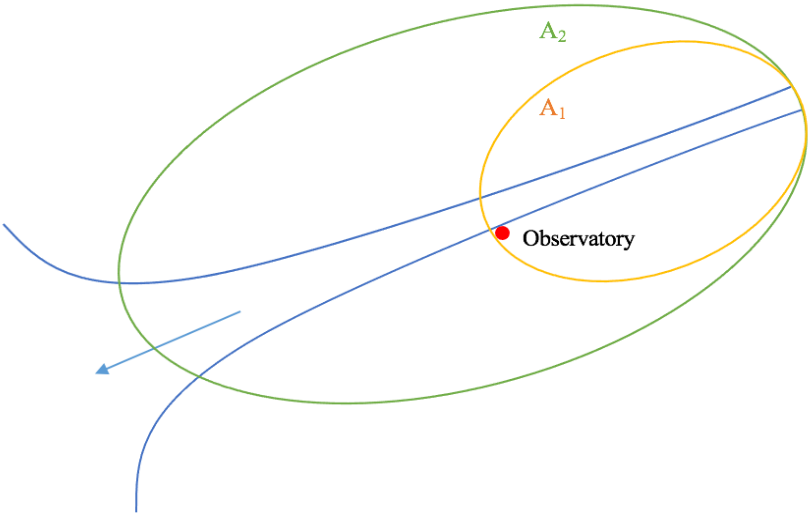

Figure 3.5 Simplified diagram of the river area.

The discharge (Q_0) from A-class rivers utilized the hourly discharge data obtained from the observatory nearest to the estuary, sourced from the Hydrological Water Quality Database of the Ministry of Land, Infrastructure, Transport, and Tourism. In the case of B-class rivers, the discharge estimation relied on the catchment area ratio in proximity to the nearby A-class rivers.

3.3 Ecosystem Model

The lower-trophic ecosystem model, simulated by the Delft3D-WAQ module, solves equations governing transport, physical, (bio)chemical, and biological processes. Substance transport relies on results generated by the hydrodynamic model simulated through the Delft3D-FLOW module, which produces a communication file. During the coupling process, temporal and spatial distributions of hydrodynamic results—

such as temperature, salinity, velocity, and turbulence dispersion coefficients—are integrated. Additionally, shear stress, temperature, and salinity coupling outcomes are represented as segment functions, necessitating manual input as parameters. These functions include time and space-varying values for all computed units and serve as forcing functions (Deltares, 2020a).

In this study, to configure the Ecosystem model, we obtained monthly monitoring data on dissolved oxygen concentrations in first-class rivers from the water quality observation station within the Ministry of Land, Infrastructure, Transport, and Tourism (MLIT) Water Information System. Subsequently, hourly DO concentrations were derived through interpolation methods. The calculation of nutrient inflow load (L) for each A-class river involved formulating L-Q equations using water quality data encompassing organic and inorganic nutrients spanning from 2001 to 2016, as elaborated in the study by Tadokoro & Yano (2019).

3.3.1 Mass transport balances

The movement of water from one computational cell to the next contributes negatively to the mass balance in the first cell and positively in the second. This method inherently conserves mass. Through combining computational cells in one, two, or three dimensions, various water systems can be accurately represented, allowing for the transportation of substances across these cells and, consequently, throughout the entire water system. The Delft3D-WAQ module addresses this simplified representation for each computational cell and state variable.

$$M_i^{t+\Delta t} = M_i^t + \Delta t \cdot \left(\frac{\Delta M}{\Delta t}\right)_{\mathrm{Tr}} + \Delta t \cdot \left(\frac{\Delta M}{\Delta t}\right)_{\mathrm{P}} + \Delta t \cdot \left(\frac{\Delta M}{\Delta t}\right)_S \tag{3.10}$$

where M_i^t is the mass at the beginning of a time step, $M_i^{t+\Delta t}$ is the mass at the end of a time step and $\left(\frac{\Delta M}{\Delta t}\right)_{\mathrm{Tr}}$, $\left(\frac{\Delta M}{\Delta t}\right)_{\mathrm{P}}$, $\left(\frac{\Delta M}{\Delta t}\right)_{\mathrm{S}}$ are changes by transport, processes and sources, respectively.

It is necessary to take the advection-diffusion equation into account, which is defined by:

$$T_{x_0}^A = v_{x_0} \times A \times C_{x_0} \tag{3.11}$$

$$T_{x_0}^{D} = -D_{x_0} \cdot A \cdot \left.\frac{\partial C}{\partial x}\right|_{x=x_0} \qquad (3.12)$$

where $T_{x_0}^{A}$ and $T_{x_0}^{D}$ are advective transport and dispersive transport (g/s), v_{x_0} is velocity at x = x_0 (m/s), A is the area perpendicular to the x-axis at x = x_0 (m^2), C_{x_0} and $\left.\frac{\partial C}{\partial x}\right|_{x=x_0}$ are concentration (g/m^3) and concentration gradient at x = x_0.

Here, a finite volume transport method is applied to solve the convection-diffusion equation. The precision of this method correlates with the dimensions Δx, A (= $\Delta y \times \Delta z$), and Δt. By introducing terms for transport in the *y*- and *z*-directions, a three-dimensional model is derived. Upon revisiting the asymptotic limit, this process results in a three-dimensional advection-diffusion equation.

$$\frac{\partial C}{\partial t} + v_x \frac{\partial C}{\partial x} - D_x \frac{\partial^2 C}{\partial x^2} + v_y \frac{\partial C}{\partial y} - D_y \frac{\partial^2 C}{\partial y^2} + v_z \frac{\partial C}{\partial z} - D_z \frac{\partial^2 C}{\partial z^2} = 0 \qquad (3.13)$$

If the functions S and f_R are added as shown in the above equation, the so-called convection diffusion reaction equation appears:

$$\frac{\partial C}{\partial t} + v_x \frac{\partial C}{\partial x} - D_x \frac{\partial^2 C}{\partial_y 2} + v_y \frac{\partial C}{\partial_2} - D_y \frac{\partial^2 C}{\partial_2 2} + v_z \frac{\partial C}{\partial_2} - D_z \frac{\partial^2 C}{\partial \alpha^2} = S + f_R(C, t) \qquad (3.14)$$

where C represents the concentration of the state variable (g/m^3), while v_x, v_y, v_z denote the velocity components (m/s). Additionally, D_x, D_y, D_z stand for the dispersion coefficients (m^2/s), and t represents time. The function S denotes the substance source entering the water system via river discharge and ocean water from the outer boundary, while function f_R encompasses physical, (bio)chemical, and biological processes (Deltares, 2020a).

3.3.2 Boundary conditions

In this study, constant boundary conditions are employed for the model boundaries. The solution to the convection-diffusion equation necessitates an open boundary, demanding the specification of concentration and dispersion coefficients for all substances across all time steps at these boundaries. The flow information is automatically derived from Delft3D-FLOW. When water crosses the boundary, it's assumed that the concentration outside the modeled area is influenced by previous outflows. In cases where flow changes and reintroduction of inflow occurs, like in tidal estuaries, it's presumed that a portion of previously outflowed water re-enters.

As the inflow progresses, boundary conditions might grow increasingly effective. The Thatcher-Harleman time lag method utilizes internal concentrations, starting from the latest outflow concentration when there's outflow, to reach the specified boundary concentration within the user-defined time lag. Accurate specification of the Thatcher-Harleman time lag (T) is essential, especially if the model domain is relatively small to the boundaries, as boundary conditions exert a significant impact on simulation results (Deltares, 2020a).

3.3.3 Processes of water quality modeling

In this study, we simplified the Generical Ecological Model (GEM) by assuming the decomposition rate of dissolved organic matter to be identical to that of inorganic matter immediately after production. The model variables encompass living organic matter (Algae), dissolved organic matter (DOM), particulate organic matter (POM), dissolved inorganic nutrients (NH_4-N, NO_3-N, and PO_4-P), and dissolved oxygen (DO) concentrations (Fig. 3.6).

The module integrated three pivotal phytoplankton-related processes: production, respiration, and mortality, along with two nutrient cycles involving nitrogen and phosphorus. Furthermore, it accounted for two fundamental DO processes: exchange across the sea surface due to reaeration and oxygen consumption by sediment. Therefore, DO was associated with production through reaeration and photosynthesis, as well as consumption through decomposition, nitrification, and sediment oxygen consumption.

Typically, a comprehensive ecological model incorporates multiple phytoplankton species (*e.g.*, Scodium algae) to account for seasonal changes in biological populations (Tanaka & Odagiri, 2010). However, this model's simulation period exclusively considers the summer season. To streamline the model, our study focuses solely on one primary phytoplankton species within the ecological model.

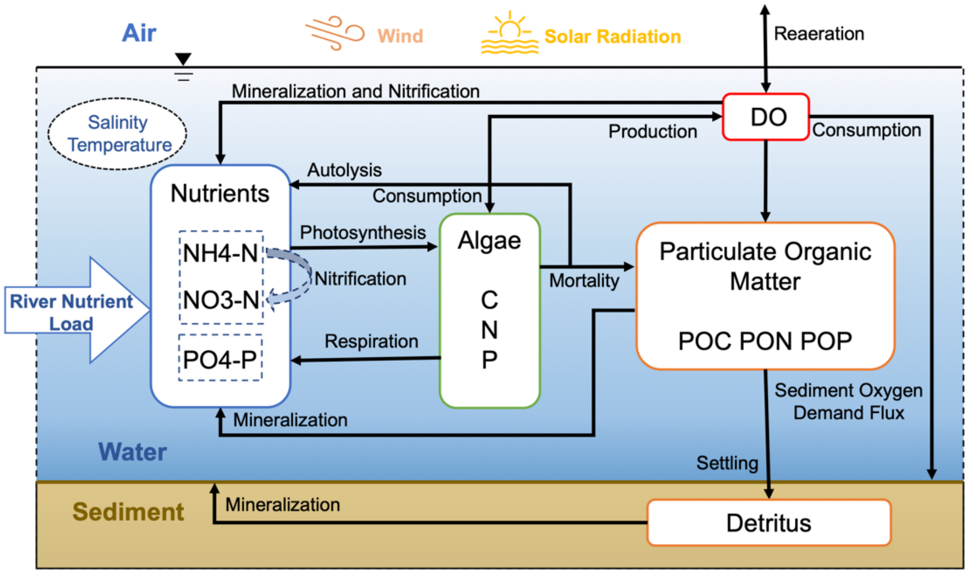

Figure 3.6 Conceptual diagram of the lower-trophic model

3.3.4 Phytoplankton processes

In the Delft3D-WAQ module, phytoplankton processes are composed of gross primary production, respiration and mortality. The general mass balance for phytoplankton is given by:

$$\frac{\Delta\, ALG}{\Delta t} = loads + transport - settling + resuspension + gross\ primary\ production - respiration\ - mortality \tag{3.15}$$

Phytoplankton generates oxygen in proportion to the gross production of organic matter. Respiration encompasses both growth respiration and maintenance respiration. Algal mortality is proportional to biomass concentration and the overall mortality rate. Sedimentation occurs only when the bottom shear stress falls below a critical value, hence relying on flow velocity and turbulence in the water. Here, net algae growth (*gro*) equals the difference between gross primary production (*gpp*) and respiration (*rsp*). The balance equations for state variables are as follows:

$$gro = gpp - rsp \tag{3.16}$$

$$gpp = \left(f_{\mathrm{nut}} \cdot f_{\mathrm{li}} \cdot k_{\mathrm{tp}}^{(T-20)} \cdot k_{\mathrm{gp}}^{20}\right) \cdot C_{\mathrm{ALG}} \tag{3.17}$$

$$rsp = \left(\propto_{\mathrm{gr}} \cdot\, gpp + k_{\mathrm{tm}}^{(T-20)} \cdot \left(1-\alpha_{\mathrm{gr}}\right) \cdot k_{\mathrm{main}}^{20}\right) \cdot C_{\mathrm{ALG}} \tag{3.18}$$

$$mrt = (k_{\mathrm{tm}}^{T-20} \cdot k_{\mathrm{mrt}}^{20}) \cdot C_{\mathrm{ALG}} \tag{3.19}$$

where f_{nut} is the nutrient limitation factor, f_{li} is the light intensity limitation, k_{tp} is temperature constant for gross primary production, k_{gp}^{20} is Potential maximum production rate constant at 20°C (day^{-1}), $\propto_{\mathrm{gr}}$ is fraction of growth respiration, k_{main}^{20} is potential maximum maintenance rate constant at 20°C (day^{-1}), k_{tm} is temperature constant for mortality and k_{mrt} is respiration and potential maximum mortality rate constant at 20°C.

In phytoplankton processes, amounts of nutrients, solar energy and temperature are the main limiting factors to affect the rate of gross primary production. Phytoplankton require chemical elements to function and the most vital elements are nitrogen and phosphorus. The absorption of light (extinction) depends on the concentration of absorbing substances, such as algal biomass, detrital organic matter, inorganic sediments and water. The more phytoplankton, the less solar energy available for each phytoplankton, until the energy of each phytoplankton cell is too small to sustain growth. A higher temperature increases the rate of the chemical processes within the algal cells, thus will lower temperature limits the growth of algal biomass (Deltares, 2020b).

The nutrient limitation factor considers only the most limiting nutrient:

$$f_{\mathrm{nut}_i} = min\left(\frac{C_{\mathrm{n}}}{K_{s,\mathrm{n}} + C_{\mathrm{n}}}, \frac{C_{\mathrm{ph}}}{K_{s,\mathrm{ph}} + C_{\mathrm{ph}}}, \frac{C_{\mathrm{si}}}{K_{s,\mathrm{si}} + C_{\mathrm{si}}}\right) \tag{3.20}$$

where C_n, C_{ph} and C_{si} are the concentration of ammonium plus nitrate, phosphate and dissolved inorganic silicate (g/m^3), $K_{s,\mathrm{n}}$, $K_{s,\mathrm{ph}}$ and $K_{s,\mathrm{si}}$ are their half saturation constant (g/m^3). Here, the parameters refer to Yamaguchi & Hayami (2018) and only consider the limitation of N and P.

Due to extinction, the light intensity within the water column diminishes compared to the intensity at the water surface. As Lambert-Beer's law, light intensity follows an exponential decay function with depth, multiplied by the extinction coefficient. The depth-averaged light intensity (W/m^2) is derived using Lambert-Beer's law to account for light attenuation:

$$I_z = I_{\text{top}} \cdot e^{(-ec*z)} \tag{3.21}$$

where ec is extinction coefficient of visible light (m^{-1}), I_{top} is light intensity at the top of a water layer (W/m^2) and z is water depth (m).

In this model, for algae cells to grow (increasing biomass) and sustain basic metabolism, respiration is essential. The respiration linked to cell growth directly correlates with gross primary production, employing a fraction α_{gr}. Furthermore, the respiration rate necessary to maintain cell survival is believed to be temperature-dependent (Deltares, 2020b).

The mortality of algae correlates with temperature, increasing with higher temperatures. When algae die, a portion of their biomass is directly released into the water as dissolved inorganic matter in a process called autolysis. However, most of the biomass remains intact and continues to exist as particulate organic matter in the nutrient cycle (Deltares, 2020a). Furthermore, while zooplankton mortality is influenced by predation from zooplankton, shells, fish, and other aquatic life, this model solely represents a lower-trophic ecosystem and does not consider algae predation.

3.3.5 Nutrient cycling processes

This model simulates a simplified cycling of two types of nutrients: nitrogen and phosphorus. It includes three major pools within the nutrient cycle: dissolved inorganic nutrients (NH_4^+, NO_3^- and PO_3^{4-}), living organic matter (Algae) and particulate organic matter (POM). The mass balances for these components are given by:

$$\begin{aligned}\frac{\Delta NO_3}{\Delta t} = \text{loads} + \text{transport} + \text{nitrification} - \text{denitrification} \\ -\text{primary production}\end{aligned} \tag{3.22}$$

$$\begin{aligned}\frac{\Delta NH_4}{\Delta t} = \text{loads} + \text{transport} - \text{nitrification} + \text{mineralization} \\ -\text{primary production} + \text{autolysis}\end{aligned} \tag{3.23}$$

$$\begin{aligned}\frac{\Delta PO_4}{\Delta t} = \text{loads} + \text{transport} + \text{mineralization} \\ -\text{primary production} + \text{autolysis}\end{aligned} \tag{3.24}$$

$$\frac{\Delta POM}{\Delta t} = \text{loads} + \ \text{transport} + \text{mortality} + \text{mineralization} - \text{setting} \tag{3.25}$$

Nutrient cycling processes are crucial for marine ecosystems and are susceptible to seasonal and regional influences. In this model, nutrient cycling primarily involves four processes: nutrient uptake by algae, nutrient release from dead algae, decomposition of organic matter, and nitrification.

(1) Uptake of nutrients by algae

The uptake of nutrients involves using the C:N:P:O ratio to calculate nutrient consumption during photosynthesis. Consequently, in the model, the nutrient uptake rate was defined as the growth rate, obtained by subtracting respiration from photosynthesis and then multiplied by the elemental composition ratios N/C (s_{N}) and P/C (s_{P}).

(2) Release of nutrients by dead algae

The mortality of algae leads to the release of nutrients, which can occur in either organic form (detritus) or inorganic form. This process follows a linear formula and is contingent upon temperature-dependent mineralization processes. Moreover, nitrogen and phosphorus in the form of debris are represented as state variables PON and POP, respectively, with PO denoting organic particles. The fluxes of PON and POP resulting from the mortality of algae are determined proportionally based on the N:C and P:C ratios within the algae biomass.

(3) Nitrification

Nitrification is the microbial, stepwise oxidation of ammonium (including its toxic form, ammonia) into nitrate, a process reliant on the presence of oxygen. While several intermediate oxidation products emerge, the final step from nitrite to nitrate is deemed rate-limiting. Notably, the accumulation of intermediate products, such as toxic nitrite (NO_2^-), is negligible in systems with residence times longer than a few days (Deltares, 2020b). This process exhibits high sensitivity to temperature, and the overall reaction equation is as follows:

$$\mathrm{NH_4^+} + 2\mathrm{O_2} + \mathrm{H_2O} \Rightarrow \mathrm{NO_3^-} + 2\mathrm{H_3O^+} \tag{3.26}$$

Here, nitrification is modeled as the sum of a zeroth and a first-order process. The nitrification rate is formulated as:

$$V_{\mathrm{nit}} = K_{0,\mathrm{nit}} + (f_{\mathrm{ox}} \cdot K_{1,\mathrm{nit}} \cdot C_{\mathrm{NH_4}}) \tag{3.27}$$

$$K_{1,\mathrm{nit}} = \begin{cases} K_{1,\mathrm{nit}}20 \cdot K_{t,\mathrm{nit}}{}^{(T-20)} & \\ 0.0 & \text{if } T < T_{\mathrm{c}} \end{cases} \tag{3.28}$$

where $K_{0,\mathrm{nit}}$ and $K_{1,\mathrm{nit}}$ are the zeroth order nitrification rate and first order nitrification rate (day^{-1}), $K_{t,\mathrm{nit}}$ is temperature coefficient for nitrification and $C_{\mathrm{NH_4}}$ is ammonium concentration (gN/m^3). It shows that if the water temperature drops below a critical value (=20°C), only the zeroth order flux remains. Moreover, the first order flux is related to water temperature and oxygen concentration, which here uses the oxygen limitation function (f_{ox}).

$$f_{\mathrm{ox}} = \begin{cases} 0 & \text{if } C_{\mathrm{ox}} \leq C_{\mathrm{oxc}} \\ \left(\frac{C_{\mathrm{ox}} - C_{\mathrm{oxc}}}{C_{\mathrm{oxo}} - C_{\mathrm{ox}}}\right) & \text{if } C_{\mathrm{oxc}} < C_{\mathrm{ox}} < C_{\mathrm{oxo}} \\ 1 & \text{if } C_{\mathrm{ox}} \geq C_{\mathrm{oxo}} \end{cases} \tag{3.29}$$

where C_{ox} is dissolved oxygen concentration for nitrification (gO$_2$/m^3), C_{oxc} is critical dissolved oxygen concentration for nitrification (gO$_2$/m^3) and C_{oxo} is optimal dissolved oxygen concentration for nitrification (gO$_2$/m^3).

(4) Decomposition

The decomposition of detrital organic matter involves a serial mineralization and conversion of six components, with each mineralization flux having a proportional conversion flux (Deltares, 2020a). This process is governed by the state variable balance equation:

$$dec_{\mathrm{POM}} = \left(k_{t,\mathrm{dec}}^{(T-20)} * k_{\mathrm{decL,POM}} + \left(k_{\mathrm{decH,POM}} - k_{\mathrm{decL,POM}}\right) \cdot f_{\mathrm{dec,nut}}\right) \cdot C_{\mathrm{POM}} \tag{3.30}$$

where $k_{t,\mathrm{dec}}$ is temperature constant for decomposition (m/day), $k_{\mathrm{decL,POM}}$ and $k_{\mathrm{decH},POM}$ are minimum and maximum first-order mineralization rate of POM (day^{-1}) and $f_{\mathrm{dec\,,nut}}$ is nutrient limitation factor for decomposition of POM. The first-order process is only active when the temperature exceeds a critical temperature (T_{c}).

3.3.6 Dissolved oxygen

In this model, dissolved oxygen (DO) is associated with the processes: production by reaeration and photosynthesis, consumption by decomposition, nitrification and sediment oxygen consumption. Among these, plant photosynthesis, decomposition, and nitrification have been previously discussed. This section delves into the processes of reaeration and sediment oxygen consumption. The mass balance is defined by:

$$\frac{\Delta DO}{\Delta t} = \text{loads} + \text{transport} + \text{reaeration} + \text{net primary production} \\ - \text{mineralization} - \text{nitrification} \tag{3.30}$$

(1) Reaeration

The reaction rate has been expressed as a linear function involving the temperature-dependent mass transfer coefficient in water and the disparity between the saturation level of dissolved oxygen and the present concentration, as depicted below:

$$rea = k_a \cdot \frac{C_{\mathrm{DOs}} - C_{\mathrm{DO}}}{z} \tag{3.31}$$

where k_a is reaeration transfer coefficient in water (m/day), C_{DOs} is saturation dissolved oxygen concentration (gO_2/m^3), and z is water depth. The reaeration transfer coefficient (m/day) is dependent on either the flow velocity or the wind speed, or dependent on both. It is given by:

$$k_a = k_{a_{20}} \cdot k_t^{\,(T-20)} \tag{3.32}$$

$$k_{a_{20}} = \left(\frac{a \cdot v^b}{H^c}\right) + (d \cdot W^2) \tag{3.33}$$

where $k_{a_{20}}$ is reaeration transfer coefficient at reference temperature 20°C (m/day), k_t is temperature coefficient for reaeration (m/day), v and W are flow velocity and wind speed respectively (m/s), a, b, c, d are coefficients with different values. The saturation concentration of DO is primarily influenced by water temperature and salinity. This model, based on Deltares (2020c), employs the following equation:

$$C_{\mathrm{DOs}} = (a_s - b_s T + (c_s T)^2 - (d_s T)^3)\left(1 - \frac{C\mathrm{cl}}{m}\right) \tag{3.34}$$

where C_{cl} is chloride concentration ($\mathrm{gCl/m^3}$), T is water temperature (°C), a_s, b_s, c_s, d_s

are coefficients with different values referring to Weiss (1970) and Truesdale *et al.* (1955). Chloride concentration depends on salinity (Deltares, 2020b) and is defined by:

$$C_{\mathrm{cl}} = \frac{1000}{1.805} S \tag{3.35}$$

where S is salinity (kg/m^3). Their relationship is shown in Fig. 3.7.

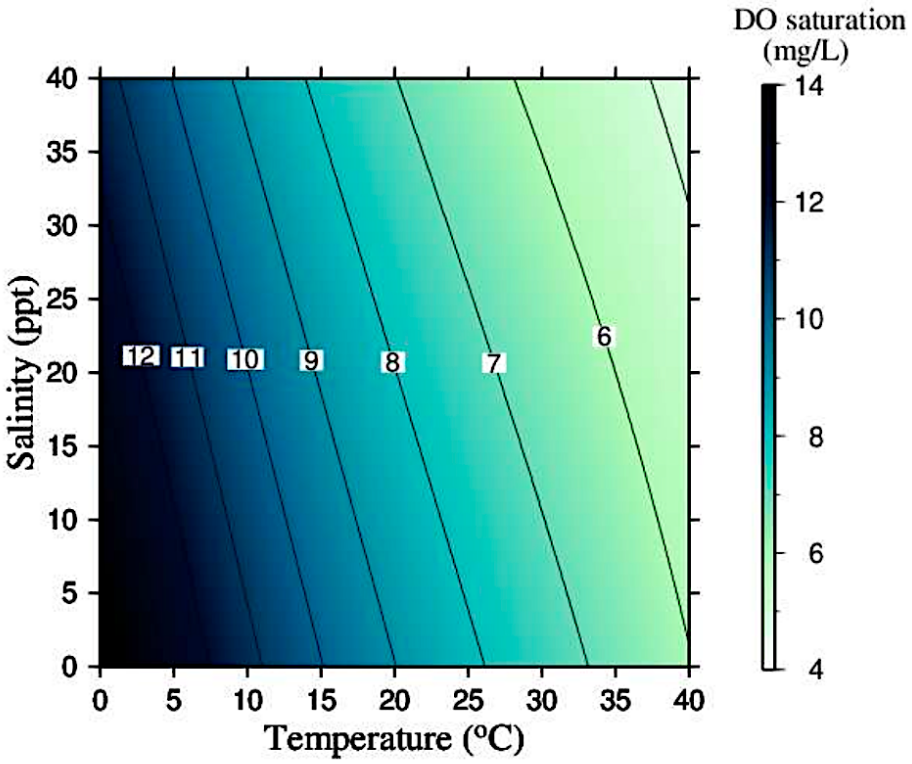

Figure 3.7 Contour of saturated oxygen content by water temperature and salinity.

(2) Sediment oxygen demand flux

The sediment oxygen demand flux denotes the measured oxygen demand within the sediment. Within this model, SOD represents the potential oxygen demand contributed by BOD and COD components in the sediment. Based on laboratory experiments by Abe (2003), oxygen consumption is calculated. However, in reality, this value fluctuates based on factors such as water temperature. For this model, a functional formula affected solely by water temperature activity was utilized to determine the decay of SOD, given by:

$$sod = \left(\frac{f_{\mathrm{sod}}}{z} + k_{\mathrm{oc}} \cdot k_{\mathrm{td}}^{(T-20)} \cdot C_{\mathrm{sod}}\right) O_{2func} \tag{3.38}$$

$$O_{2func} = \begin{cases} 0 & (C_{\mathrm{DO}} < C_{\mathrm{cr,sod}}) \\ \frac{C_{\mathrm{DO}} - C_{\mathrm{cr,sod}}}{C_{\mathrm{op,sod}} - C_{\mathrm{cr,sod}}} & (C_{\mathrm{cr,sod}} \leq C_{\mathrm{DO}} \leq C_{\mathrm{op,sod}}) \\ 1 & (C_{\mathrm{DO}} > C_{\mathrm{op,sod}}) \end{cases} \tag{3.39}$$

where f_{sod} is reference sediment oxygen demand (gO^2/m^2/day), k_{oc} and k_{td} are decay rate of SOD at 20 °C (day^{-1}) and temperature coefficient SOD decay, O_{2func} is oxygen function for decay of SOD, which depends on the relationship of oxygen concentration in surface water (C_{DO}) between critical oxygen concentration for SOD decay ($C_{\mathrm{cr,sod}}$) and optimal oxygen concentration for SOD decay ($C_{\mathrm{op,sod}}$).

3.3.7 Overview of parameters

Section 3.3 delineates the fundamental processes within the lower-trophic ecosystem model. Beyond the previously mentioned processes, additional phenomena such as denitrification, phosphate adsorption, autolysis, and various others occur. Table 3.2 offers an overview of the state variables and parameter inputs employed in the trophic-ecosystem model, established based on the DO model settings proposed by Tadokoro & Yano (2019).

Table 3.2 State variables and parameter input used in trophic-ecosystem model.

Description	Symbol	Value	Unit	Reference
State Variables				
Ammonium	C_{NH4}	*	gN/m^3	
Nitrate	C_{NO3}	*	gN/m^3	
Ortho-phosphate	C_{PO4}	*	gP/m^3	
Particulate organic carbon	C_{POC}	*	gC/m^3	
Particulate organic nitrogen	C_{PON}	*	gN/m^3	
Particulate organic phosphorus	C_{POP}	*	gP/m^3	
Particulate organic carbon in sediment	$C_{s,\mathrm{C}}$	*	gC/m^2	
Particulate organic nitrogen in sediment	$C_{s,\mathrm{N}}$	*	gN/m^2	
Particulate organic phosphorus in sediment	$C_{s,\mathrm{P}}$	*	gP/m^2	
Dissolved oxygen concentration	C_{DO}	*	gO$_2$/m^3	
Algae biomass	C_{ALG}	*	gC/m^3	
Fluxes				
Net algae growth	*gro*	*	gM/m^3/day	
Gross primary production	*gpp*	*	gM/m^3/day	
Algae respiration	*rsp*	*	gM/m^3/day	
Algae mortality	*mrt*	*	gM/m^3/day	
Decomposition of POM	*dec*	*	gM/m^3/day	
Settling flux	*set*	*	gM/m^3/day	
Autolysis of algae mortality	*aut*	*	gM/m^3/day	
Nitrification	*nit*	*	gM/m^3/day	
Reaeration	*rea*	*	gO$_2$/m^3/day	
Sediment oxygen demand	*sod*	*	gO$_2$/m^3/day	
Limiting factors				
Nutrient limitation factor for algae growth	f_{nut}	*	-	
Radiation limitation factor for algae growth	f_{li}	*	-	
Nutrient limitation factor for dec. of POM	$f_{\mathrm{dec,nut}}$	*	-	
Oxygen limitation factor for nitrification	f_{ox}	*	-	
Parameters and constants				
Algae				
Potential maximum production rate at 20°C	k_{gp}^{20}	1.5	day^{-1}	(D)
Potential maximum respiration rate at 20°C	k_{main}^{20}	0.041	day^{-1}	(Y)
Potential maximum mortality rate at 20°C	k_{mrt}^{20}	0.2	day^{-1}	(Y)
Temperature factor for primary production	k_{tp}	1.06	-	(Y)

Table 3.2 Continued

Description	Symbol	Value	Unit	Reference
Temperature factor for respiration	k_{tm}	1.07	-	(Y)
Temperature factor for mortality	k_{tm}	1.07	-	(Y)
Half saturation constant for nitrogen for algae growth	$K_{s,\mathrm{n}}$	0.005	gN/m^3	(G)
Half saturation constant for phosphorus for algae growth	$K_{s,\mathrm{ph}}$	0.001	gP/m^3	(G)
Light intensity at water surface	I_0	***	W/m^2	
Optimum light intensity for algae	I_{opt}	96.898	W/m^2	(Y)
Attenuation coefficient	ec	1.5	m^{-1}	(C)
Particulate organic matter				
Fraction of autolysis	α_{aut}	0.3	-	(B)
Maximum mineralization rate at 20°C of POC	$kmin_{\mathrm{max}}$, POC	0.24	day^{-1}	(C)
Minimum mineralization rate at 20 °C of POC	$kmin_{\mathrm{min}}$, POC	0.22	day^{-1}	(C)
Maximum mineralization rate at 20 °C of PON	$kmin_{\mathrm{max}}$, PON	0.24	day^{-1}	(C)
Minimum mineralization rate at 20 °C of PON	$kmin_{\mathrm{min}}$, PON	0.08	day^{-1}	(B)
Maximum mineralization rate at 20 °C of POP	$kmin_{\mathrm{max}}$, POP	0.24	day^{-1}	(C)
Minimum mineralization rate at 20 °C of POP	$kmin_{\mathrm{min}}$, POP	0.08	day^{-1}	(B)
Temperature factor for decomposition	$k_{t\mathrm{dec}}$	1.047	-	(G)
Upper limit stoichiometric constant PON	$f_{s\mathrm{U,N}}$	0.15	gN/gC	(D)
Lower limit stoichiometric constant PON	$f_{s\mathrm{L,N}}$	0.1	gN/gC	(D)
Upper limit stoichiometric constant POP	$f_{s\mathrm{U,P}}$	0.015	gP/gC	(D)
Lower limit stoichiometric constant POP	$f_{s\mathrm{L,P}}$	0.01	gP/gC	(D)
Settling velocity of POM	w_s	0.432	m/day	(Y)
Critical shear stress for POM	τ_c	0.3	N/m^2	(D)
Fraction of ammonium in nitrogen uptake	f_{uptN}	*	-	
Critical ammonium concentration	$C_{\mathrm{c,NH4}}$	0.01	gN/m^3	(D)
N:C ratio in algae biomass	s_{N}	0.16	gN/gC	(D)
P:C ratio in algae biomass	s_{P}	0.02	gP/gC	(D)
Potential maximum elution rate at 20°C	$K_{1,\mathrm{mel}}^{20}$	0.03	day^{-1}	(D)
Temperature factor for elution	$K_{t,\mathrm{mel}}$	1.09	-	(D)
Potential maximum nitrification rate at 20°C	$K_{1,\mathrm{nit}}^{20}$	0.02	day^{-1}	(Y)
Temperature factor for nitrification	$K_{t,\mathrm{nit}}$	1.03	-	(Y)

Table 3.2 Continued

Description	Symbol	Value	Unit	Reference
Dissolved oxygen				
Critical concentration of DO for nitrification	$C_{\mathrm{cr,DO}}$	1	$\mathrm{gO_2/m^3}$	(D)
Optimal concentration of DO for nitrification	$C_{\mathrm{op,DO}}$	5	$\mathrm{gO_2/m^3}$	(D)
O:C ratio in POC	s_{O}	2.67	$\mathrm{gO_2/gC}$	(D)
O:N ratio in $\mathrm{NO_3}$	s_{NO}	4.571	$\mathrm{gO_2/gN}$	(D)
Reaertion factor	k_a	0.7	$\mathrm{day^{-1}}$	(Y)
Saturation dissolved oxygen concentration	C_{DOs}	*	$\mathrm{gO_2/m^3}$	
Chloride concentration	$\mathrm{C_{cl}}$	*	$\mathrm{gCl/m^3}$	
Specified SOD	f_{sod}	1.5	$\mathrm{gO_2/m^2/day}$	(C)
Potential maximum SOD rate at 20°C	K_{oc}	0.5	$\mathrm{gO_2/m^3/day}$	(C)
Temperature factor for SOD	K_{td}	1.07	-	(C)
Critical concentration of DO for SOD	$C_{\mathrm{cr,sod}}$	0	$\mathrm{gO_2/m^3}$	(D)
Optimum concentration of DO for SOD	$C_{\mathrm{op,sod}}$	0.5	$\mathrm{gO_2/m^3}$	(C)
Physical input data				
Salinity	S	**	ppt	
Water temperature	T	**	°C	
Water depth	D	**	m	
Shear stress	τ	**	$\mathrm{N/m^2}$	

* : Calculated in Delft3D-WAQ
** : Calculated in Delft3D-FLOW
*** : Observation data

(B) : Blauw, *et. al.*(2009)
(C) : Calibrated
(D) : Delft3D-WAQ
(G) : Gurel, *et. al.*(2005)
(Y) : Yamaguchi, *et. al.*(2018)

3.4 Model Accuracy Verification

The numerical models utilized in this study have demonstrated good reproducibility at the tidal level (Yano et al., 2010), as well as in salinity, temperature, and bottom DO (Tadokoro and Yano, 2019). For accuracy verification, we compared the reproducibility of salinity, temperature, and bottom DO at St.6 throughout the summer months of June, July, and August. The simulated water temperatures corresponded well with observed values at most wave crests (Fig. 3.8a). However, the simulated values at the wave troughs tended to exceed the observed values (Fig. 3.8b). This discrepancy might be attributed to lower surface winds inputted into the model compared to the actual sea breeze (Stoffelen, 1998). Meanwhile, the simulated salinity accurately mirrored the decrease in surface salinity resulting from freshwater influx (Fig. 3.7c and Fig. 3.7d). The simulated DO generally followed a similar trend to the observed values, particularly when influenced by flood events (Fig. 3.8e).

Additionally, we utilized three performance metrics—Willmott's skill parameter (d), Root Mean Squared Error (RMSE), and Mean Absolute Error (MAE) (Willmott, 1982)—to quantitatively evaluate the model's performance. Willmott's skill parameter, which falls between 0 and 1, signifies the level of agreement between the simulation and observation, with values closer to 1 indicating stronger agreement. Typically, skill values above 0.5 denote excellent model performance. The results indicated strong agreement between the model predictions and observed data, with Willmott's skill parameter ranging from 0.73 to 0.90. Both RMSE and MAE also demonstrated minimal error, as detailed in Table 3.3.

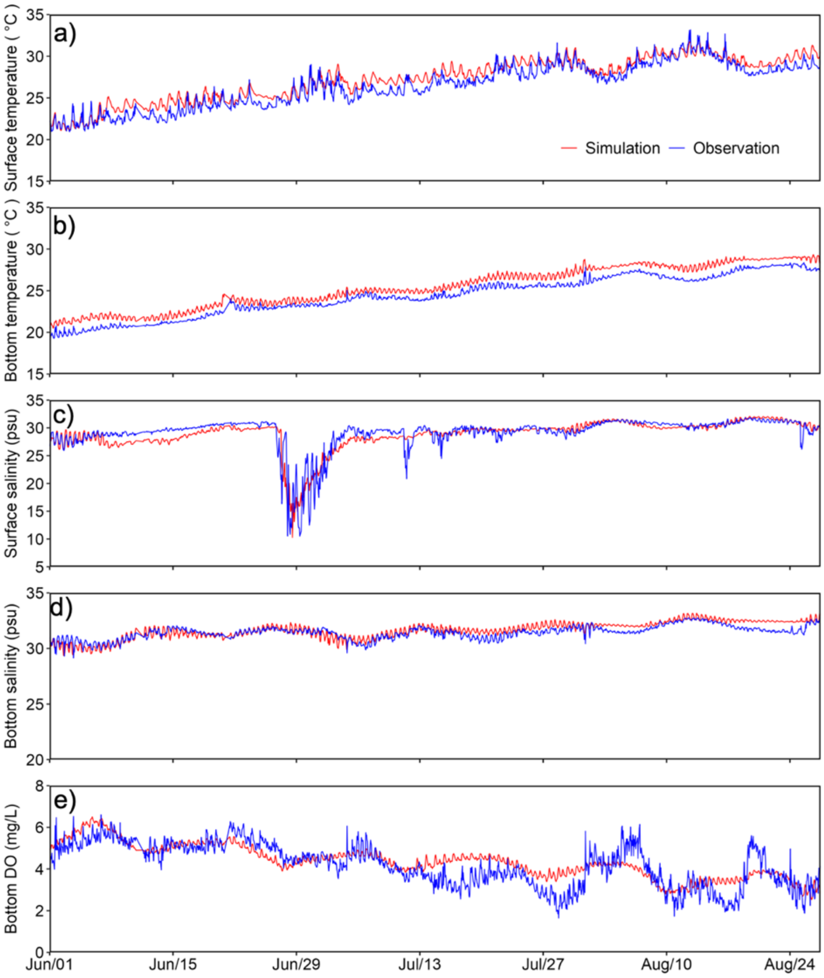

Figure 3.8 Time series of hourly observed and simulated data for a) surface temperature, b) bottom temperature, c) surface salinity, d) bottom salinity, and e) bottom DO during the summer of 2004 at St.B6.

Table 3.3 Willmott's skill parameter (d), Root Mean Squared Error (RMSE), and Mean Absolute Error (MAE) for environmental variables with N Samples.

Variable	**d**	**RMSE**	**MAE**	**N**
Surface Temperature (℃)	0.90	0.68	0.53	2052
Bottom Temperature (℃)	0.90	0.36	0.28	2052
Surface Salinity (psu)	0.86	1.04	0.77	2042
Bottom Salinity (psu)	0.82	0.42	0.36	2058
Bottom DO (mg/L)	0.73	0.51	0.40	2049

3.5 Results and Discussion

3.5.1 Stratification and hypoxia due to the 2020 Kyushu Floods

On July 4, 2020, the cumulative rainfall in the entire Chikugo River basin exceeded 500 mm, resulting in the highest water level measured by the Senoshita observatory downstream of the river in recent years. Fig. 3.9 displays the river discharge hydrograph of A-class rivers during the summer of 2020 (June, July, and August). During the 2020 Kyushu Floods, the Chikugo River experienced a prolonged effluent period lasting approximately 40 days, with a maximum hourly discharge reaching 8,000 m^3/s. This discharge accounted for roughly half of the total peak discharge observed in A-class rivers, excluding the Kuma River and the Honmyo River. Notably, the hydrograph reveals multiple lower peak discharges alongside the main peak discharge during this period. Fig. 3.10 illustrates the weather conditions observed at the Kumamoto observatory during the summer of 2020. After a prolonged effluent period from June 25 to August 4, Typhoon 2009 (MAYSAK) approached Kyushu on September 2, resulting in strong winds of up to 11.8 m/s on September 3.

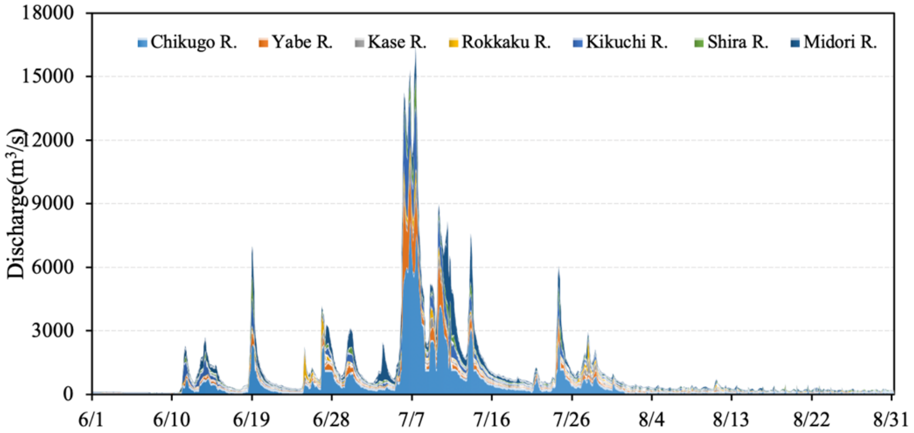

Figure 3.9 River discharge hydrograph of the A-class rivers, excluding the Kuma R. and Honmyo R. in the summer of 2020.

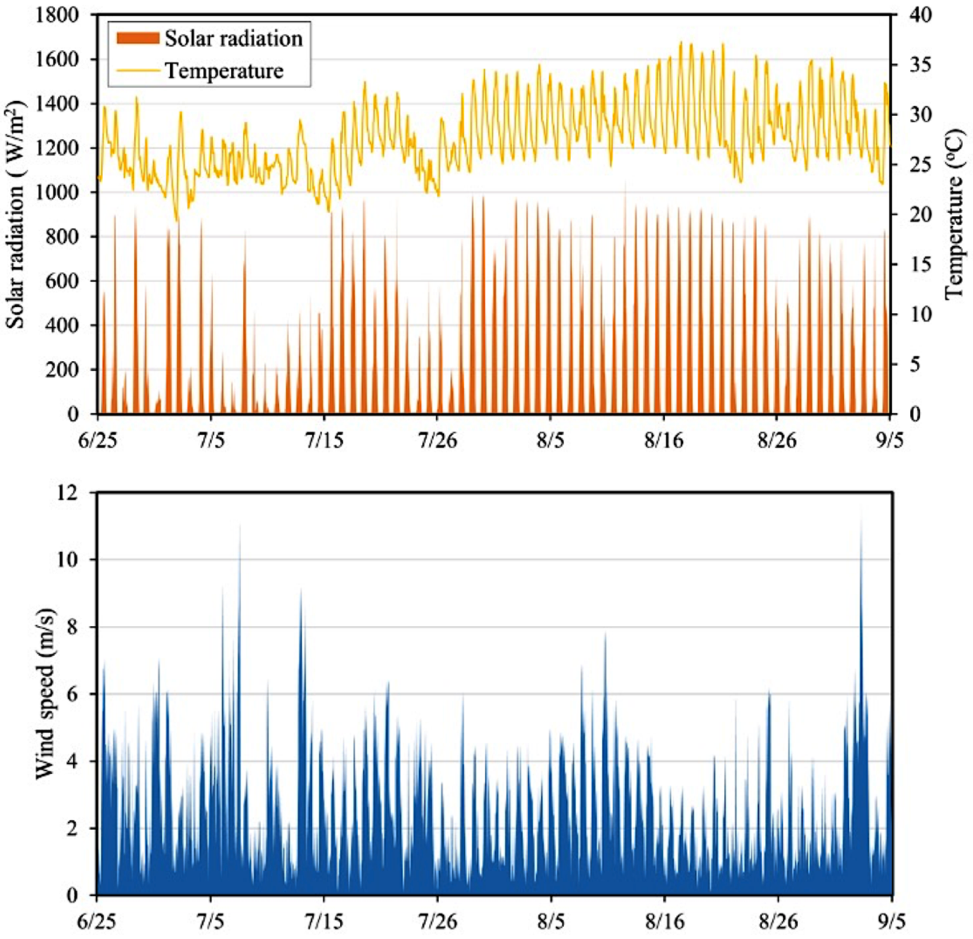

Figure 3.10 Solar radiation (red) and air temperature (yellow) (upper) and wind speed (below) at the Kumamoto observatory in the summer of 2020.

Heavy rainfall resulted in a substantial influx of freshwater into the Ariake Sea, potentially reducing salinity levels and causing density stratification (Yano et al., 2014). Fig. 3.11 describes the time series vertical distribution of salinity and DO at St.1 during the 2020 effluent period. As the influx of freshwater persisted, reaching its peak flow on July 6, a noticeable intensification of stratification occurred within the water column (Fig. 3.11a). This heightened stratification furthered the development of hypoxia throughout the water body, ultimately culminating in the establishment of anoxia (DO < 0.5 mg/L) at the bottom layer (Fig. 3.11b). This prolonged hypoxic state endured for over two months, with August exhibiting a larger and more vertically distributed hypoxic water mass compared to other months within the summer period (June to August). Besides, increased freshwater inflows significantly impacted the dynamics of salinity, particularly affecting nutrient transport in the bay's interior areas

(Murphy et al., 2011).

The interaction between tidal currents and density gradient leads to periodic variations in stratification. Strong tidal flow and turbulent mixing disrupt stratification and promote the vertical exchange of oxygenated water from the surface to the bottom, which in turn enhances the diffusion and distribution of DO, and thereby effectively mitigates the occurrence of hypoxia and anoxia (Kim et al., 2018). The dissipation of contiguous hypoxia occurred in September, which coincides with the period prone to typhoons (Fig. 3.10b). As a result, the influence of typhoons on the mixing and circulation patterns of the water column can be cited as a contributing factor, along with the intensified mixing of water bodies during spring tides, which assists in the alleviation of hypoxia.

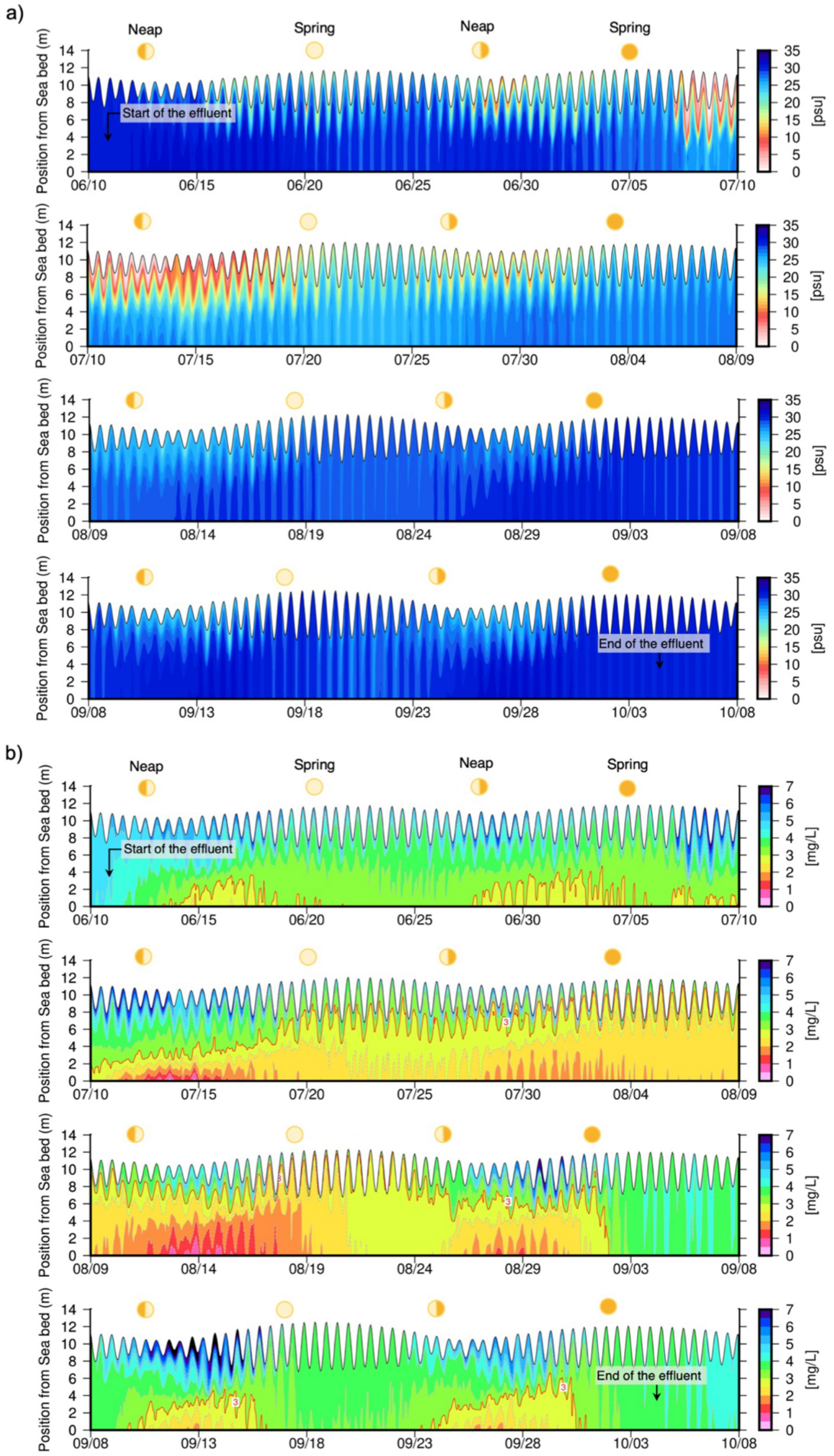

Figure 3.11 Isopleths of a) salinity and b) DO in 2020 at St.1. The red isolines in b) represent DO = 3 mg/L.

3.5.2 Effects of river discharge on the hypoxia

To assess the influence of various effluent patterns on hypoxia development during the summer rainy season (June to August), we designed six cases, considering alterations in effluent volume and peak discharge. Details of these distinct effluent patterns are outlined in Table 3.4.

Table 3.4 Calculation results of hypoxia for six flood patterns, which are extracted in the past 20 years (from 2000 to 2020) and observation points are at Sta.B3, Sta.B6 and Sta.KS73-1.

Case	**Year**	Q_{max} (m^3/s)	**Total volume of effluent** ($10^6 m^3$)	**Normalized total volume of effluent**	**Duration of hypoxia (day)**		
					Sta.B3	**Sta.B6**	**Sta.KS73-1**
1	2020	16,457.33	8,263.50	11.77	59.6	45.5	60.4
2	2018	16,000.46	2,925.55	4.17	23.9	6.8	20.0
3	2017	9,571.35	1,493.07	2.13	6.0	0	5.5
4(a)	2009 (1st)	10,410.90	1,672.60	2.38	0.2	0	0
4(b)	2009 (2nd)	9,608.09	2,394.19	3.41	5.8	0	4.9
5	2006	8,789.71	6,800.86	9.68	46.4	22.3	42.4
6	2004	3,936.39	702.27	1.00	0.3	0	0

The total effluent volume is calculated by aggregating the hourly river discharge from all A-class rivers (excluding Kuma River and Honmyo River) throughout the effluent period. This calculation is normalized based on the minimum value recorded in case 6. Hypoxia duration specifically denotes the persistence of hypoxic conditions within the bottom layer. Notably, this study conducts a comparison of hypoxia extents between 2006 and 2020 (Case 5 and Case 1), with the summer of 2006 being notable for recording unprecedented hypoxic events (Hamada et al., 2007).

Fig. 3.12 illustrates the relationship among the normalized total effluent volume, hypoxia duration, and peak discharge Q_{max} as detailed in Table 3.4. Notably, while case 1 and case 2 exhibit similar peak discharge values, their total effluent volumes differ considerably. This discrepancy results in a prolonged duration of continuous hypoxia in case 1 compared to case 2, despite both cases showing extended hypoxia periods. Case 1 and case 5 suggest that the hypoxia development during the summer of 2020 might surpass the severity observed in the past 20 years. Comparing case 2, case 3, and case 6, it becomes evident that longer hypoxia durations correlate with larger effluent volumes. Additionally, the hypoxia development appears to intensify with increased peak discharge $Q_{\max}$. Additionally, the nearshore areas (St.KS73-1) and the region of the Isahaya Sea dike (St. B3) exhibit increased vulnerability to freshwater influence compared to central regions, consequently resulting in extended periods of hypoxia.

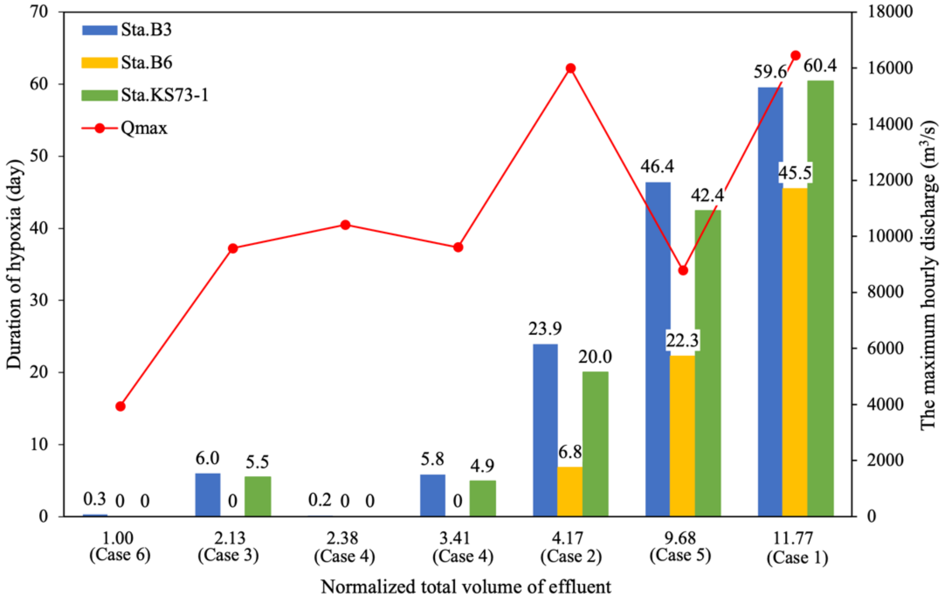

Figure 3.12 Relationship of normalized total effluent volume and duration of hypoxia at the bottom layer as well as the peak discharge in each case.

3.5.3 Tempo-spatial distribution of hypoxia

Seasonal hypoxia has been consistently observed in the inner areas of the bay since at least 2001 (Tsutsumi, 2006). In recent years, this phenomenon has shown an increased tendency to expand across the entirety of the Ariake Sea, attributed to the effects of climate change. The dynamics of DO in summer are notably sensitive to warming temperatures and increased freshwater inflow, exacerbating the deterioration of the marine environment. These factors intensify stratification and amplify nutrient loading, contributing to the degradation of water quality.

Figure 3.13 illustrates the most severe hypoxic conditions at the bottom following each effluent scenario. Across all cases, the most intense hypoxia was consistently observed in the northern region of the bay and the inner areas of Isahaya Bay. As the magnitude of the effluent increased, there was a discernible trend of the hypoxic area gradually expanding towards the central Ariake Sea. Particularly noteworthy was the emergence of large-scale anoxic water masses in the head of the bay and the inner sections of Isahaya Bay. As depicted in Fig. 3.14, the dissipation of hypoxia is determined by the threshold of DO > 3mg/L at Sta.B3. In cases with large-scale effluent, the dissipation requires an extended duration due to vertical mixing induced by wind and the gradual return to regular river discharge levels. Additionally, the impact of spring tides contributes to the dissipation process by facilitating the transfer of oxygen from the surface to the bottom (Hamada et al., 2007).

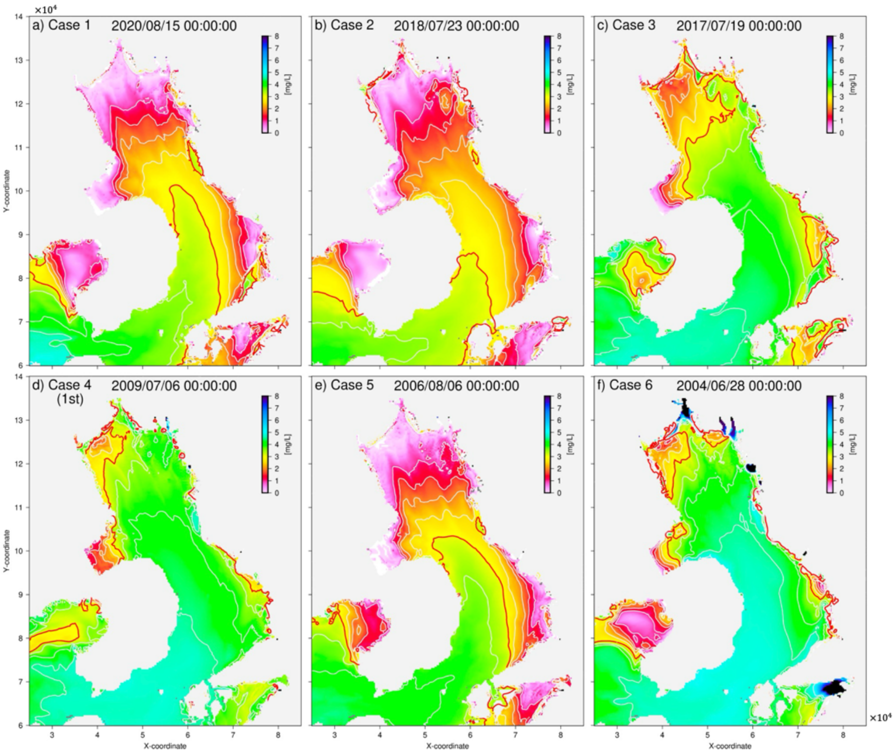

Figure 3.13 Spatial distribution of the bottom DO at the worst situation after the effluent in each case. The red line is 3 mg/L.

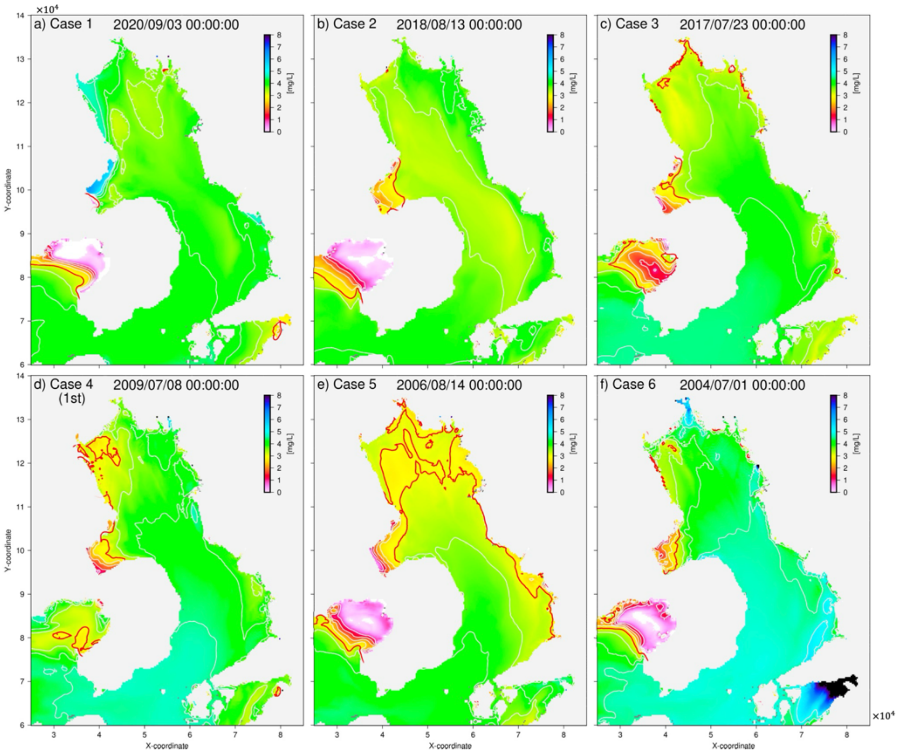

Figure 3.14 Spatial distribution of the bottom DO when dissipation occurs in each case. Red line is 3 mg/L.

3.6 Conclusions

The coupling of the hydrodynamic model and lower-trophic ecosystem model in the Ariake Sea enabled an exploration of the relationship between effluent patterns and DO dynamics. This study revealed several results:

(1) The duration and peak discharge of effluent strongly influence the development of hypoxia in the bottom layer.

(2) The historic extreme flood event in 2020 led to a longer duration of continuous hypoxia compared to the 2006 event, which previously held the record for the largest hypoxia occurrence post-2000.

(3) The intensified peak river discharge and prolonged flood duration, attributed to climate change, may impact the marine benthic ecosystem by altering the tempo-spatial scale of hypoxia. Additionally, the effluent patterns displayed varying effects on hypoxia development across different

positions.

However, this study solely delved into the impact of floods on water DO. Future investigations should encompass a combination of the hydrodynamic and hydrological models to examine the collective influence of factors like water temperature and rainfall on DO dynamics. This study will provide a comprehensive understanding of the ecological environment in the Ariake Sea, contributing to the formulation of strategies for optimizing fishery production.

References

Abe, J. (2003). Formation of High Turbidity Layer and Oxygen Consumption Process in the Western Ariake Sea. *Journal of Japan Society of Civil Engineers*, *Ser. B2 (Coastal Engineering)*, *50*, 996–970.

Abeysingha, N. S., Islam, A., & Singh, M. (2020). Assessment of climate change impact on flow regimes over the Gomti River basin under IPCC AR5 climate change scenarios. *Journal of Water and Climate Change*, *11*(1), 303–326. https://doi.org/10.2166/wcc.2018.039

Blauw, A. N., Los, H. F. J., Bokhorst, M., & Erftemeijer, P. L. A. (2009). GEM: A generic ecological model for estuaries and coastal waters. *Hydrobiologia, 618*(1), 175–198. https://doi.org/10.1007/s10750-008-9575-x

Deltares. (2017). Delft3D-FLOW users' manual; simulation of multi-dimensional hydrodynamic flows and transport phenomena, including sediments. *Version: 3.15*, *Deltares*, *Delft*, *The Netherlands (2017).*

Deltares. (2020a). Delft3D-Water quality User Manual, *Version:1.1.63465. Deltares, Delft*, *The Netherlands (2020).*

Deltares. (2020b). Delft3D-Water Quality Processes Technical Reference Manuall, *version: 5.01.69903. Deltares, Delft*, *The Netherlands (2020).*

Du, J., Shen, J., Park, K., Wang, Y. P., & Yu, X. (2018). Worsened physical condition due to climate change contributes to the increasing hypoxia in Chesapeake Bay. *Science of The Total Environment*, *630*, 707–717. https://doi.org/10.1016/j.scitotenv.2018.02.265

Easterling, D. R., Evans, J. L., Groisman, P. Y., Karl, T. R., Kunkel, K. E., & Ambenje, P. (2000). Observed Variability and Trends in Extreme Climate Events: A Brief Review *. *Bulletin of the American Meteorological Society*, *81*(3), 417–425. https://doi.org/10.1175/1520-0477(2000)081<0417:OVATIE>2.3.CO;2

Gurel, M., Tanik, A., Gonec, E., and Russo, R. C. (2005). *Biogeochemical Cycles. In: J. P. Wolflin & I. E. Gonenc, eds. Coastal Lagoons. s.l.:CRC Press.*

Hamada T., Hayami Y., Yamamoto K., Yoshino K., Ohgushi K., Hirakawa R., &

Yamada Y. (2007). The Observation of Growth-decay Process of Hypoxic Water Mass in the head of Ariake Bay. *PROCEEDINGS OF COASTAL ENGINEERING, JSCE*, *54*, 1121–1125. https://doi.org/10.2208/proce1989.54.1121

IPCC. (2018). Summary for Policymakers. In: *Global Warming of 1.5°C. An IPCC Special Report on the impacts of global warming of 1.5°C above pre-industrial levels and related global greenhouse gas emission pathways, in the context of strengthening the global response to the threat of climate change, sustainable development, and efforts to eradicate poverty* [Masson-Delmotte, V., P. Zhai, H.-O. Pörtner, D. Roberts, J. Skea, P.R. Shukla, A. Pirani, W. Moufouma-Okia, C. Péan, R. Pidcock, S. Connors, J.B.R. Matthews, Y. Chen, X. Zhou, M.I. Gomis, E. Lonnoy, T. Maycock, M. Tignor, and T. Waterfield (eds.)]. Cambridge University Press, Cambridge, UK and New York, NY, USA, pp. 3-24. https://doi.org/10.1017/9781009157940.001.

Kim, S., Hayami, Y., Tai, A., & Tada, A. (2018). The mechanism of bottom water DO variation in summer at the northern mouth of Isahaya Bay, Japan. *Journal of Oceanography*, *74*(6), 595–605. https://doi.org/10.1007/s10872-018-0467-z

Knapp, A. K., Beier, C., Briske, D. D., Classen, A. T., Luo, Y., Reichstein, M., Smith, M. D., Smith, S. D., Bell, J. E., Fay, P. A., Heisler, J. L., Leavitt, S. W., Sherry, R., Smith, B., & Weng, E. (2008). Consequences of More Extreme Precipitation Regimes for Terrestrial Ecosystems. *BioScience*, *58*(9), 811–821. https://doi.org/10.1641/B580908

Kundzewicz, Z. W., Merz, B., Vorogushyn, S., Hartmann, H., Duethmann, D., Wortmann, M., Huang, Sh., Su, B., Jiang, T., & Krysanova, V. (2015). Analysis of changes in climate and river discharge with focus on seasonal runoff predictability in the Aksu River Basin. *Environmental Earth Sciences*, *73*(2), 501–516. https://doi.org/10.1007/s12665-014-3137-5

Kyushu Regional Agricultural Administration Bureau. (2019). *Ariake Sea Fishing Ground Environmental Improvement Liaison Council (28th).* [Online] Available at: https://www.maff.go.jp/kyusyu/seibibu/isahaya/gyobakannkyou/gyoba_kankyou28.html [Accessed Nov. 2019]

Ministry of Land, Infrastructure, Transport and Tourism. (2020). About flooding in heavy rain in July 2nd year of Reiwa (2nd report).

Murphy, R. R., Kemp, W. M., & Ball, W. P. (2011). Long-Term Trends in Chesapeake Bay Seasonal Hypoxia, Stratification, and Nutrient Loading. *Estuaries and Coasts*, *34*(6), 1293–1309. https://doi.org/10.1007/s12237-011-9413-7

Osburn, C. L., Atar, J. N., Boyd, T. J., & Montgomery, M. T. (2019). Antecedent precipitation influences the bacterial processing of terrestrial dissolved organic matter in a North Carolina estuary. *Estuarine, Coastal and Shelf Science*, *221*, 119–131. https://doi.org/10.1016/j.ecss.2019.03.016

Rabalais, N. N., Díaz, R. J., Levin, L. A., Turner, R. E., Gilbert, D., & Zhang, J. (2010). Dynamics and distribution of natural and human-caused hypoxia. *Biogeosciences*, *7*(2), 585–619. https://doi.org/10.5194/bg-7-585-2010

Scully, M. E. (2013). Physical controls on hypoxia in Chesapeake Bay: A numerical modeling study. *Journal of Geophysical Research: Oceans*, *118*(3), 1239–1256. https://doi.org/10.1002/jgrc.20138

Sinha, E., Michalak, A. M., & Balaji, V. (2017). Eutrophication will increase during the 21st century as a result of precipitation changes. *Science*, *357*(6349), 405–408. https://doi.org/10.1126/science.aan2409

Stoffelen, A. (1998). Toward the true near-surface wind speed: Error modeling and calibration using triple collocation. *Journal of Geophysical Research: Oceans*, *103*(C4), 7755–7766. https://doi.org/10.1029/97JC03180

Tadokoro, M., & Yano, S. (2019). Evaluation of effects of temperature and river discharge changes due to climate change on hypoxia in the Ariake Sea. *Journal of Japan Society of Civil Engineers, Ser. B2 (Coastal Engineering), 75*(2), I_1231-I_1236. https://doi.org/10.2208/kaigan.75.I_1231

Tanaka M., & Odagiri M. (2010). Mechanism of the Oxygen-Depleted Water Formation near the Head of the Ariake Bay and its Numerical Modeling. *Journal of Japan Society of Civil Engineers, Ser. B2 (Coastal Engineering)*, *66*(1), 1011–1015. https://doi.org/10.2208/kaigan.66.1011

Tishchenko, P. Ya., Lobanov, V. B., Zvalinsky, V. I., Sergeev, A. F., Koltunov, A., Mikhailik, T. A., Tishchenko, P. P., Shvetsova, M. G., Sagalaev, S., & Volkova, T. (2013). Seasonal Hypoxia of Amursky Bay in the Japan Sea: Formation and Destruction. *Terrestrial, Atmospheric and Oceanic Sciences*, *24*(6), 1033. https://doi.org/10.3319/TAO.2013.07.12.01(Oc)

Truesdale, G. A., Downing, A. L., & Lowden, G. F. (1955). The solubility of oxygen in pure water and sea-water. *Journal of Applied Chemistry, 5*(2), 53–62.

Tsutsumi, H. (2006). Critical events in the Ariake Bay ecosystem: Clam population collapse, red tides, and hypoxic bottom water. *Plankton and Benthos Research*, *1*(1), 3–25. https://doi.org/10.3800/pbr.1.3

Wang, H., Chen, Q., Hu, K., & La Peyre, M. K. (2017). A Modeling Study of the Impacts of Mississippi River Diversion and Sea-Level Rise on Water Quality of a Deltaic Estuary. *Estuaries and Coasts*, *40*(4), 1028–1054. https://doi.org/10.1007/s12237-016-0197-7

Weiss, R. F. (1974). Carbon dioxide in water and seawater: the solubility of a non-ideal gas. *Marine Chemistry, 2*(3), 203–215. https://doi.org/10.1016/0304-4203(74)90015-2

Yamaguchi, S., & Hayami, Y. (2018). Impact of Isahaya dike construction on DO concentration in the Ariake Sea. *Journal of Oceanography*, *74*(6), 565–586. https://doi.org/10.1007/s10872-017-0454-9

Yano S., Nishimura K., Kitagawa Y., & Abdul N. Arifin. (2014). Examination on Effects of River Flooding Pattern on Baroclinic Structure in the Ariake Sea. *Journal of Japan Society of Civil Engineers, Ser. B2 (Coastal Engineering)*, *70*(2), I_436-I_440. https://doi.org/10.2208/kaigan.70.I_436

Yano, S., Winterwerp, J. C., Tai, A., & Saita, T. (2010). Numerical experiments on features of nonlinear tide and its influences on sediment transport in the Ariake Sea and the Yatsushiro Sea. *Journal of Japan Society of Civil Engineers, Ser. B2 (Coastal Engineering)*, *66*(1), 341–345.

Chapter 4

Influence of Summer Effluent on the Bottom Water DO Variation in the Yatsushiro Sea

4.1 Introduction

In recent years, the degradation of water quality in the Ariake Sea and the Yatsushiro Sea, both situated in western Kyushu, has become an increasingly pressing concern. This decline has triggered a cascade of adverse effects, significantly impacting the fisheries within these coastal regions. Similar to the Ariake Sea, the Yatsushiro Sea experiences a notable decline in water quality due to substantial freshwater inflows, leading to a conspicuous salinity stratification that surpasses temperature stratification.

Recent years have witnessed a deterioration in the Yatsushiro Sea's water conditions, resulting in an expanding impact on fisheries (Aoki et al., 2012; Sonada et al., 2013). Factors such as red tide, density stratification, acidification, and hypoxia have emerged as key influencers, with hypoxia believed to be a predominant contributor to this degradation. Over the past few decades, the annual catch yields of key species like the Manila Clam and benthic fish such as Nibe Croaker and Sole have experienced a significant decline in the bay (Ministry of the Environment, 2017). Starting in 2016, reports revealed a concerning downward trend in DO levels within certain sea areas, reaching as low as 4 mg/L by 2019 (Ministry of the Environment, 2016 & 2019). While the precise causes remain unclear, these changes signify an evolving marine ecological structure within the bay (Sonoda & Takikawa, 2016).

In the previous chapter, our study focused on assessing the influence of heavy rainfall on the emergence of hypoxia within the Ariake Sea. As a continuation of this investigation, the present chapter employs the same numerical models to evaluate the repercussions of summer extreme rainfall events on the dissolved oxygen (DO) levels in the Yatsushiro Sea.

4.2 The Numerical Models

4.2.1 Study area

The Yatsushiro Sea, spanning 1,200 km^2, forms a semi-enclosed coastal region linked partially to the Ariake Sea via three channels. It receives inflows from multiple rivers, notably the Kuma River, distinguished as the only A-class river contributing to the sea's northern domain. The Kuma River undergoes substantial seasonal fluctuations owing to shifting precipitation patterns, impacting the ecosystem dynamics of the Yatsushiro Sea. These fluctuations play a vital role in shaping water quality, nutrient distribution, and overall ecological balance within the sea (Aoki et al., 2014). Renowned for its unique tidal flats and extensive seaweed beds, the Yatsushiro Sea boasts high biological productivity. Additionally, serving as a prominent area for yellowtail aquaculture, the sea holds economic importance as a key producing region. However, mortality of aquaculture yellowtail due to Chartoella blooms has increased significantly in recent years (Nakashima et al., 2019). Recent surveys indicate a significant increase in the frequency of red tides (Takikawa et al., 2005). All these issues require a comprehensive and detailed investigation of the region's changing environmental dynamics.

In this study, the Yatsushiro Sea is delineated into five distinct parts, as illustrated in Fig. 4.1, with St. 11 chosen as the observation point situated at the head of the bay (Y1), characterized by intense stagnation. Similarly, Y2 exhibits notable stagnation and stands out due to its direct connection to the Ariake Sea, receiving direct freshwater input from the Kuma River. Y1 and Y2, particularly susceptible to the July rainy season, experience decreased salinity and lower DO levels at the bottom due to the presence of a halocline (Sonoda et al., 2013). The heavy rainfall in June and July significantly augments nutrient influx throughout the entire sea area. Notably, from October to February, the region sustains heightened nutrient levels attributed to marine aquaculture and fish farming activities (Sonoda et al., 2013).

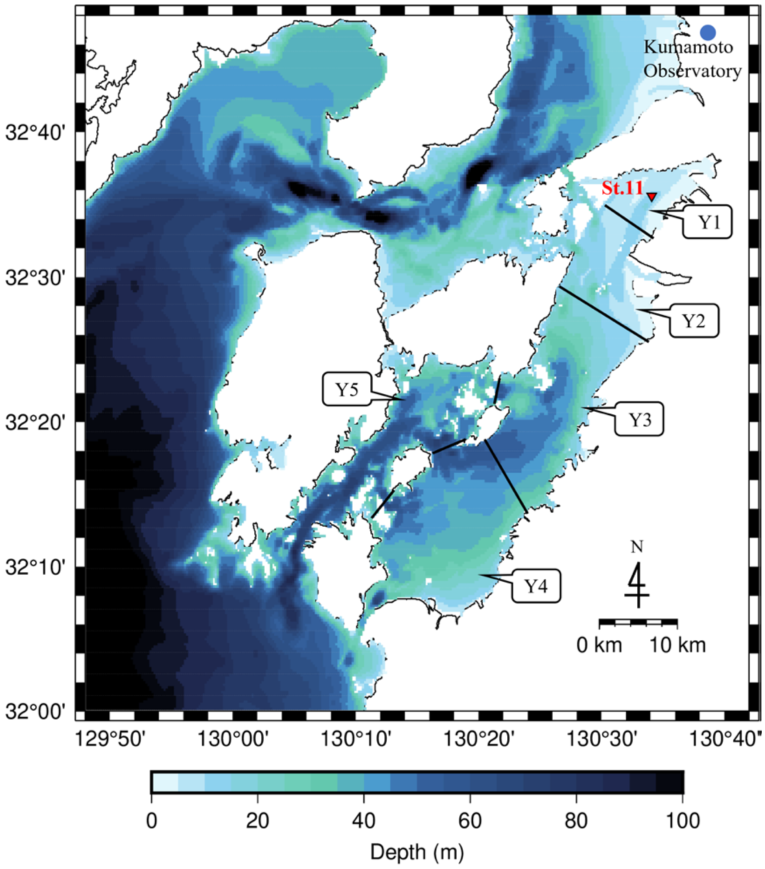

Figure 4.1 Sea area distinction of the Yatsushiro Sea. The red triangle indicates the observational point. The blue circle indicates Kumamoto Observatory.

4.2.2 Hydrodynamic model and ecosystem model

The numerical models employed in this study mirror those detailed in the preceding chapter, involving the coupling of a hydrodynamic model with an ecosystem model, as depicted in Fig. 4.2. The configuration of the general coastal 3-D hydrodynamic model remains consistent with that of the previous chapter. In the lower-trophic ecosystem model, we adjusted the empirical values for bottom oxygen demand to better align with the ecological characteristics of the Yatsushiro Sea, subsequently calibrating the model accordingly.

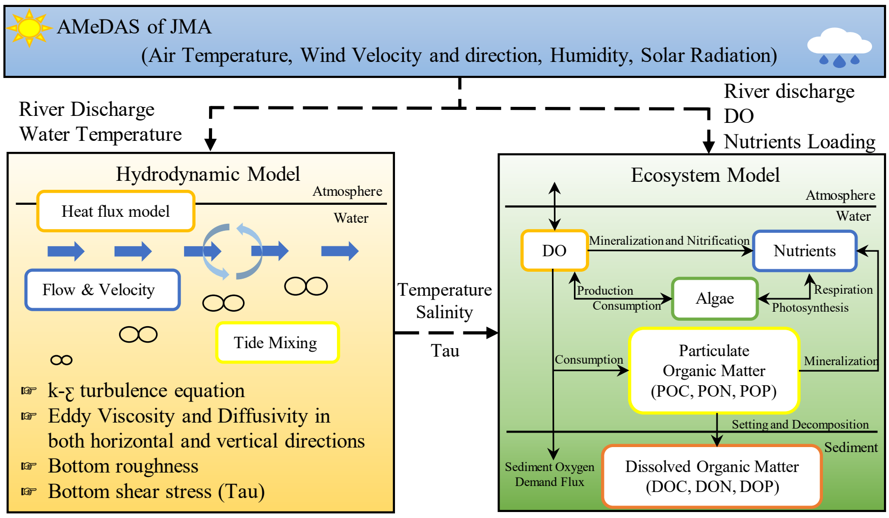

Figure 4.2 Coupling of the hydrodynamic model and lower-trophic ecosystem model.

4.2.3 Model reproducibility

Komori et al. (2021) established the strong reproducibility of the numerical model in simulating carbon dioxide dynamics within the Yatsushiro Sea. In this study, we further validated the performance of the model in the Yatsushiro Sea. Fig. 4.3a shows that the time series of calculated salinity can accurately simulate the trend of the surface salinity, especially during the flood period, which is responsible for driving a significant factor of circulation. In Fig. 4.3b, both time series of calculated DO and observations show lower DO at the bottom layer in July and August. However, the observed DO in June and October is much higher than the calculated values as the model does not consider over-saturation at the surface layer. Here, observational data was obtained from the Kumamoto Port and Airport Development Office, Kyushu Regional Development Bureau, Ministry of Land, Infrastructure, Transport and Tourism.

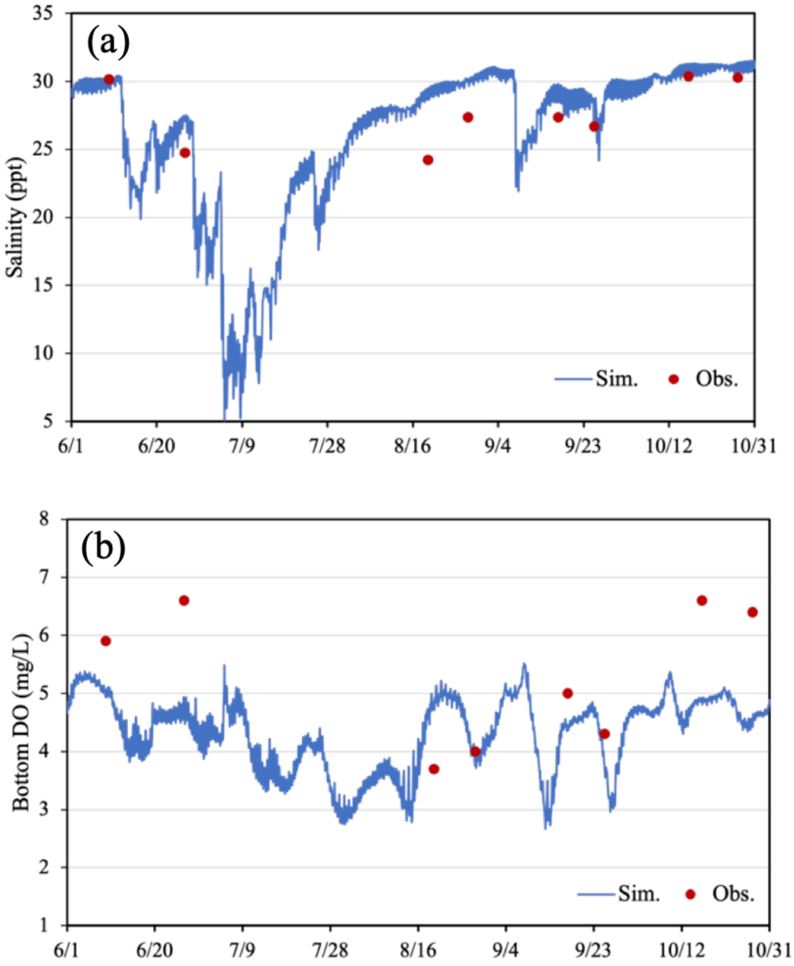

Figure 4.3 Time series of a) simulated salinity and observations at the sea surface and b) simulated DO and observations at the bottom layer at St.11 (the maximum depth is about 14m) in the summer of 2020.

4.3 Results and Discussion

4.3.1 Spatial distribution of bottom DO

The rivers tend to exhibit strong seasonal variation due to the rainy season from early June to mid-July. A continuous inflow of freshwater may cause the change in density that is responsible for driving the circulation in the bay (Tishchenko et al., 2013). Concurrently, maintaining a balance in salinity levels is pivotal for stabilizing the water column (Simpson, 1997). During the 2020 Kyushu Floods, the Kuma River experienced peak discharge, reaching 11,000 m^3/s on July 4, 2020, with the effluent period extending for 20 days. Sea surface salinity gradually decreased as the bay received a large amount of freshwater from the river.

Figures 4.4a and 4.4b portray the spatial patterns of sea surface salinity during peak discharge and DO levels at the bay's bottom layer on July 31, 2020, representing the lowest DO concentration following the effluent. The bay exhibited uniformly low DO levels (DO < 4 mg/L) except for Y5, while hypoxia was notably widespread across Y1, Y2, and a segment of Y3. Remarkably, regions susceptible to freshwater inflow, particularly Y1 and Y2, displayed consistently lower sea surface salinity compared to other bay areas during this period (Fig. 4.4d).

The complete dissipation of hypoxia was observed on August 20, 2020 (Fig. 4.4e), coinciding with intensified vertical mixing and the subsequent replenishment of DO. Figures 4.4c and 4.4f illustrate surface horizontal flow velocities during the onset and dissipation of hypoxia, respectively. The escalated flow velocity throughout the region notably facilitated horizontal mixing processes.

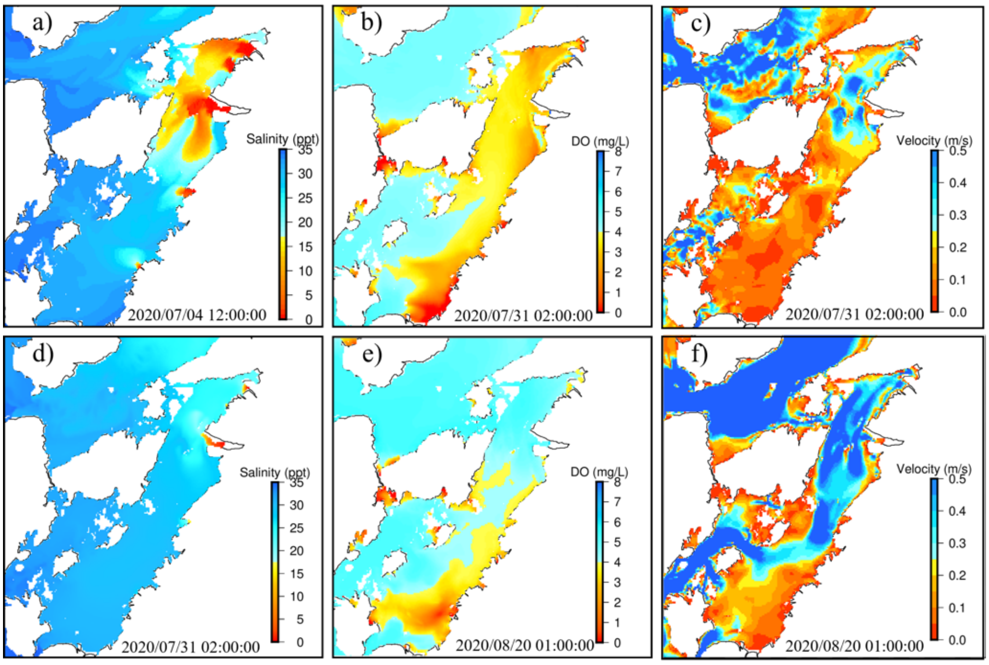

Figure 4.4 Spatial distribution of a) sea surface salinity at peak discharge, b) the bottom DO in the worst situation, c) horizontal flow velocity at sea surface when the lowest DO occurred, d) sea surface salinity at the worst case of the bottom DO, e) the dissipation of the bottom DO, and f) horizontal flow velocity at sea surface at the time of DO dissipation in the Yatsushiro Sea.

Additionally, wind dynamics played a significant role in wave formation and sea surface temperature alterations, considered another contributing factor to the dissipation of hypoxia (Tishchenko et al., 2013). The wind rose (Fig. 4.5) indicates the southwesterly wind prevailed in the week before the dissipation of the bottom hypoxia which strengthened the surface water flow and vertical circulation.

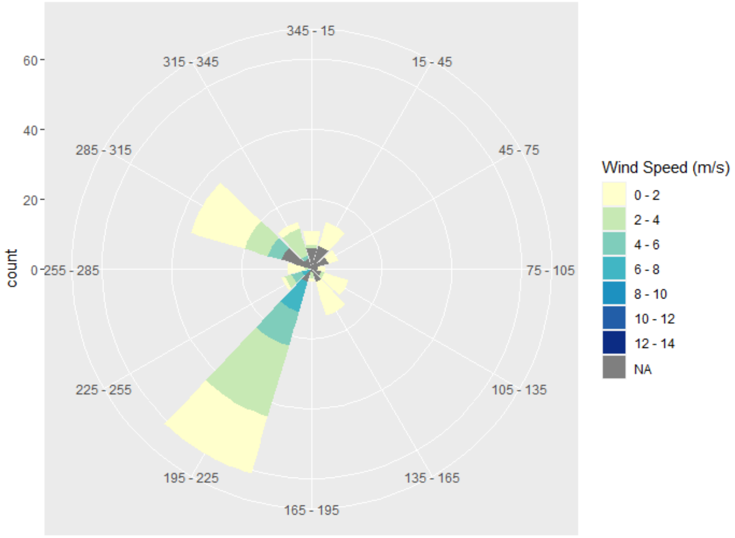

Figure 4.5 Wind rose diagram at Kumamoto observatory from August 13, 2020 to August 20, 2020.

Furthermore, the limited water exchange in the southern part of Y4, attributed to its semi-enclosed hydrogeomorphology, contributed to the persistence and difficulty in dissipating hypoxia (Kasai et al., 2007; Diaz & Rosenberg, 2008). Conversely, Y5 experiences a significantly stronger exchange flux, influenced by the external ocean, rendering it less susceptible to the effects of hypoxia compared to other regions within the Yatsushiro Sea.

4.3.2 Influence of the effluent on the hypoxia

Fig. 4.6 presents the hourly and cumulative discharge data of the Kuma River during summers from 2017 to 2020. Notably, the Kyushu floods in 2020 led to a peak flow of approximately 11,000 m^3/s, doubling the 2018 peak flow of approximately 5,600 m^3/s and significantly surpassing peak flows in other years, which measured around 2,500 m^3/s in 2017 and 1,400 m^3/s in 2019. Fig. 4.7a indicates that large-scale effluent caused salinity reduction and stratification at St.11 (Fig. 4.1) from July 4 to July 15, 2020.

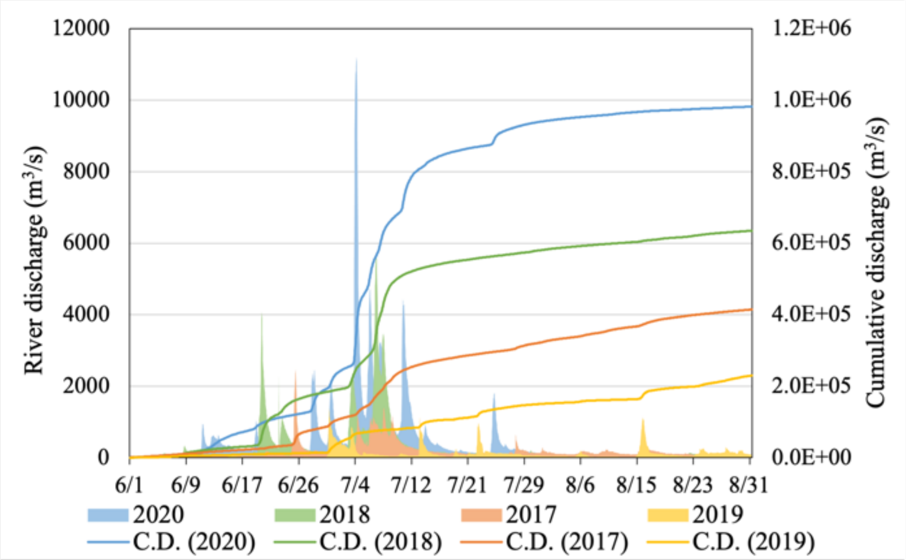

Figure 4.6 Hourly and cumulative discharge of the Kuma River in summer from 2017 to 2020.

The onset of hypoxia emerged towards the conclusion of the effluent period and recurred subsequently (Fig. 4.7b). Furthermore, the low DO concentration (DO < 4 mg/L) lasted for approximately one month. In contrast, during other years (2017, 2018, 2019), the hypoxia development diminished as the effluent scale reduced. In the summer of 2018, severe hypoxia ensued after the peak river discharge, enduring for about ten days (Fig. 4.7d). However, the persistence of low DO is significantly less than the case in 2020. Despite a larger effluent scale in 2017 compared to 2019, hypoxia was observed towards the end of July 2019 (Fig. 4.7h). Throughout the 2019 summer, four small-scale effluent events occurred from July to August, with the initial three concentrated in July (Fig. 4.6). Notably, a thermocline was evident between July 22 and July 28, potentially contributing to an extended duration of hypoxia.

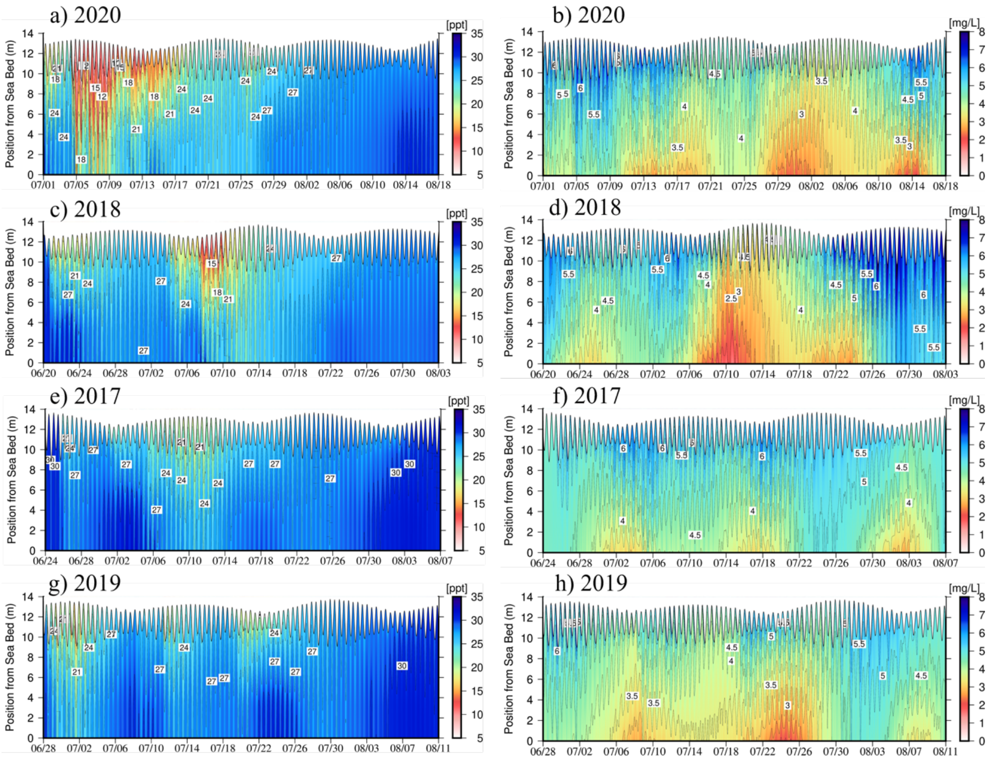

Figure 4.7 Isopleth of salinity (left) and DO (right) at St.11 (Fig. 4.1) in the summer of a, b) 2020, c, d) 2018, e, f) 2017 and g, h)2019.

4.4 Conclusions

In this chapter, we simulated the salinity and DO using the coupled hydrodynamic and ecosystem models and evaluated the impact of different scales of effluents on the development of hypoxia in the Yatsushiro Sea. The reproducibility of sea surface salinity and Bottom DO indicate the excellent performance of the numerical models though only one species of algae was considered in the model, which may decrease the accuracy of DO dynamic simulation. The Yatsushiro Sea was divided into five parts from its environmental characteristics to evaluate the spatial distribution of hypoxia. Furthermore, we evaluated the effect of effluent on the development of hypoxia by comparing the different scales of effluents in summer. The major results are as follows:

(1) The spatial-temporal hypoxic scale of DO due to the large-scale effluent in the bay can be assessed.

(2) Due to the 2020 Kyushu Floods, the worst hypoxia situation occurred in the

whole area of the Yatsushiro Sea except for Y5 on July 31. It took about 20 days to dissipate completely. Y1 and Y2 are susceptible to hypoxia due to the large effluent. Moreover, the persistence of low DO in the southern part of Y4 may be due to the small flow velocity and the difficult water exchange.

(3) The development of hypoxia is subject to the scale and duration of effluents. Large-scale and long-duration effluent can cause severe hypoxia and last for a long time.

In both this chapter and the previous one, numerical simulations were employed to assess the impact of the 2020 Kyushu heavy rainfall on hypoxia development in the Ariake Sea and Yatsushiro Sea, respectively. Our findings indicate an exacerbation of hypoxia beyond historical records in both bays, significantly affecting the marine environment. The increase in frequency and intensity of extreme rainfall due to climate change exacerbates salinity stratification, stemming from substantial freshwater influx, consequently leading to reduced DO levels and heightened nutrient influx. Moreover, rising summer temperatures contribute to increased thermal stratification. In forthcoming research, we aim to evaluate the dominant factors driving hypoxia through extended numerical simulations, facilitating a comprehensive understanding of the evolving coastal marine environment.

References

Aoki, K., Onitsuka, G., Shimizu, M., Kuroda, H., Matsuo, H., Kitadai, Y., Sakurada, K., Ando, H., Nishi, H., & Tahara, Y. (2014). Variability of factors driving spatial and temporal dispersion in river plume and Chattonella antiqua bloom in the Yatsushiro Sea, Japan. *Marine Pollution Bulletin*, *81*(1), 131–139. https://doi.org/10.1016/j.marpolbul.2014.02.005

Aoki, K., Onitsuka, G., Shimizu, M., Kuroda, H., Matsuyama, Y., Kimoto, K., Matsuo, H., Kitadai, Y., Sakurada, K., Nishi, H., & Tahara, Y. (2012). Factors controlling the spatio-temporal distribution of the 2009 Chattonella antiqua bloom in the Yatsushiro Sea, Japan. *Estuarine, Coastal and Shelf Science*, *114*, 148–155. https://doi.org/10.1016/j.ecss.2012.08.028

Diaz, R. J., & Rosenberg, R. (2008). Spreading Dead Zones and Consequences for Marine Ecosystems. *Science*, *321*(5891), 926–929. https://doi.org/10.1126/science.1156401

Kasai, A., Yamada, T., & Takeda, H. (2007). Flow structure and hypoxia in Hiuchi-nada, Seto Inland Sea, Japan. *Estuarine, Coastal and Shelf Science*, *71*(1–2), 210–217. https://doi.org/10.1016/j.ecss.2006.08.001

Komori, H., Xiong, B., Saito, N., Hao, L., Chi, B., Yano, S., Komai, K., & Nakayama, K. (2021). Numerical Modeling of CO2 Dynamics in Seawater Considering Effects of Freshwater Inflow in the Yatsushiro Sea. *Journal of Japan Society of Civil Engineers, Ser. B2 (Coastal Engineering)*, *77*(2), I_847-I_852. https://doi.org/10.2208/kaigan.77.2_I_847

Ministry of the Environment (2017). Report of Ariake Sea / Yashiro Sea Comprehensive Survey and Evaluation Committee, Chapter 3 (in Japanese).

Ministry of the Environment (2016). *Results of Regular Environmental Survey in 2016* p.2 (in Japanese).

Ministry of the Environment (2019). *Results of Regular Environmental Survey in 2019*, p.2 (in Japanese).

Nakashima, H., Murata, K., Yano, K., Nishi, H., Yoshimura, N., Kuroki, Y., Kawasaki, S., Furukawa, S., Ura, K., & Matsuo, H. (2019). A Chattonella bloom in the

Yatsushiro Sea, Japan in summer 2016: Environmental characteristics during the bloom and mortality of cultured yellowtail Seriola quinqueradiata. *Nippon Suisan Gakkaishi*, *85*(2), 162–172.

Simpson, J. H. (1997). Physical processes in the ROFI regime. *Journal of Marine Systems*, *12*(1–4), 3–15. https://doi.org/10.1016/S0924-7963(96)00085-1

Sonoda, Y., Takigawa, H., Kawasaki, S., Aoyama, C., & Saito, T. (2013). Characteristics of seawater quality in Yatsushiro Sea area. *J. JSCE Ser. B3*, *69*, I1240-I1245.

Sonoda, Y. and Takikawa, K. (2016) Characterization of benthos distribution and sediment environment in the Yatsushiro Sea, *J. JSCE, Ser. B3, Vol.72*, pp.I_1069-I_1074.

Takikawa, K., Aoyama, C., Tanaka, K., Morimoto, K., & Watanabe, K. (2005). Characteristics of Environment in Yatsushiro Sea. *Asian and Pacific Coasts 2005, September 4-8, 2005, Jeju, Korea*, 1452–1463.

Tishchenko, P. Ya., Lobanov, V. B., Zvalinsky, V. I., Sergeev, A. F., Koltunov, A., Mikhailik, T. A., Tishchenko, P. P., Shvetsova, M. G., Sagalaev, S., & Volkova, T. (2013). Seasonal Hypoxia of Amursky Bay in the Japan Sea: Formation and Destruction. *Terrestrial, Atmospheric and Oceanic Sciences*, *24*(6), 1033. https://doi.org/10.3319/TAO.2013.07.12.01(Oc)

Chapter 5

Relationship between River Discharge and Hypoxia Duration in the Ariake Sea, Alongside Numerical Experiments on Nutrient Loads

5.1 Introduction

River discharge plays a significant role in shaping the environment and ecosystem of semi-coastal water areas. Tanaka et al. (2021) emphasized in their investigation of flood risks within river basins that the intensity and frequency of extreme effluents in each basin will increase in future climate scenarios. A large amount of freshwater inflow could alter estuarine circulation, affecting organic matter transport, while its nutrient content could lead to eutrophication and hypoxia, negatively impacting marine ecology (Tanaka M. & Odagiri, 2010). Additionally, substantial river flow volumes transport sediments, leading to alterations in the estuary's landform and morphology (Elias & Hansen, 2013).

During the summer, especially in the rainy season, the Ariake Sea is significantly influenced by external factors, including increased temperature, freshwater, and nutrient loadings (Yano et al., 2014; Tadokoro et al., 2020). These effects result in diverse water environment issues, encompassing stratification, hypoxia, and ecological concerns like red tides and nori discoloration. In our previous chapter, we established that extreme rainfall could trigger stratification formation, ultimately leading to the development of hypoxia on a temporal-spatial scale in the Ariake Sea.

This chapter aims to explore the correlation between the effluent volume caused by summer floods and hypoxia duration. Additionally, it assesses the vulnerability of hypoxia occurrence across various observation sites. Furthermore, this chapter evaluates the inflow of freshwater, accompanied by nutrient loadings, as an additional factor influencing the aquatic environment of the Ariake Sea through numerical experiments.

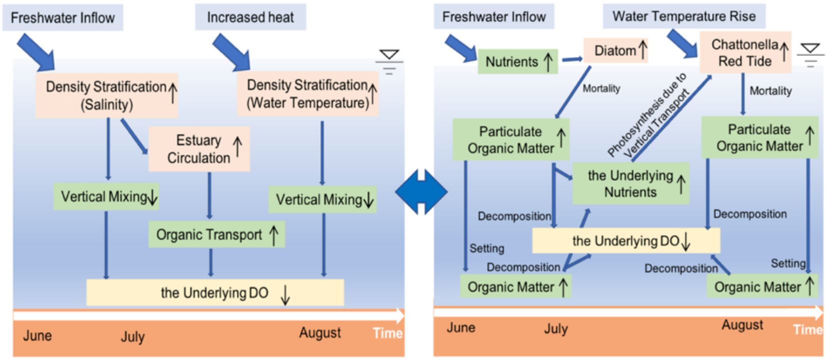

Figure 5.1 Conceptual diagram of physical process and biochemical process (Tanaka and Odagiri, 2010).

5.2 Data Compilation

Data compilation involved the collection and structuring of climatic, hydrological, and water quality datasets spanning from 1992 to 2021.

The climatic data, obtained at hourly intervals, includes air temperature, solar radiation, wind speed and direction, as well as humidity. These datasets were sourced from the Kumamoto climate monitoring station of the AMeDAS system of Japan Meteorological Agency (JMA). The river discharge (*Q*) data from 2001 to 2021 was obtained from the monitoring station closest to the estuary in the non-tidal zone of the Water Information System managed by the Ministry of Land, Infrastructure, Transport, and Tourism (MLIT). From 1992 to 2000, discharge calculations were performed using a rainfall-runoff model based on the 1K-DHM, as described in Tanaka et al. (2015). To account for downstream inflow, the station flow rate was corrected by multiplying it with a factor calculated by dividing the station's catchment area by the total watershed area. For B-class rivers, the calculation was based on the catchment area ratio to nearby A-class rivers (refer to Section 3.2). River salinity was assumed to be a constant at 0 psu, and the river water temperature was calculated by the empirical formula based on long-term observation and measured temperature data (Tadokoro and Yano, 2019).

Nutrient calculations employed the *L*-*Q* equation, whereas DO measurements from the river were obtained at a water quality observatory situated near the selected hydrological observatory.

5.3 The Numerical Models

The calculation area encompassed both the Ariake Sea and the Yatsushiro Sea, with the numerical model settings identical to those in chapter 3. In this study, the dataset used for model calculations spans 30 years, from 1992 to 2021. Notably, in 1997, the Ministry of Agriculture, Forestry, and Fisheries in Japan constructed the Isahaya Sea dike, a 7-kilometer-long barrier that partitioned the bay into two distinct areas. Periodically, the dike releases a certain amount of freshwater from reservoirs through gates situated at its southern and northern ends. Studies indicate that this construction has led to a reduction in tidal currents and DO concentrations, impacting both Isahaya Bay and the head of Ariake Bay (Tadokoro et al., 2020). After 2000, the decline in bivalve catches is attributed to oxygen depletion during summers, a consequence of ongoing reclamation activities (Hodoki & Murakami, 2006; Jia et al., 2018).

To enhance the model's accuracy, we accounted for the influence of the Isahaya Sea Dike by using a grid without the dike in calculations before 1997. Concurrently, the model now integrates the Honmyo River as a significant contributor to freshwater inflow, as depicted in Fig. 5.2.

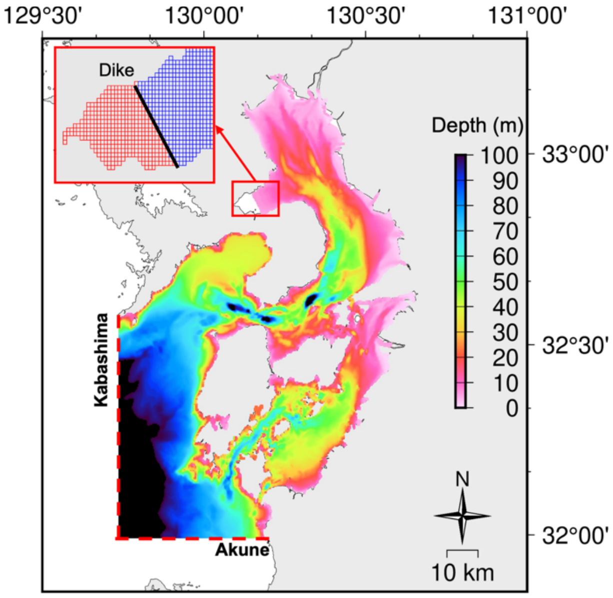

Figure 5.2 The calculation domain of the numerical models, where the red grid within the red box represents the calculation grid with the dike, and the blue grid represents the calculation grid without the dike. The red dotted line indicates the open boundaries.

5.4 Results and Discussion

5.4.1 Stratification and hypoxia

During the summer rainy season, the river discharge from the Chikugo River to the Ariake Sea exhibited a notable increase. In the past 50 years (1972-2021), there have been a total of 24 occurrences of small and medium-scale effluent with a peak discharge below 2,000 m^3/s, while large-scale effluent with a peak flow rate exceeding 4,000 m^3/s has occurred 4 times, predominantly concentrated within the last decade. Previous studies have demonstrated that such large-scale effluent events can lead to severe stratification. This study utilized the density stratification index (SI) proposed by Simpson et al. (1990) to assess the strength of density stratification. The equation for calculating the SI is presented in Equation (4.1):

$$\mathrm{SI} = \frac{1}{H}\int_{-H}^{0}(\rho_{ave}-\rho)gz\,\mathrm{d}z \tag{5.1}$$

where H is total water depth, ρ is the density at a given depth, ρ_{ave} is the vertically averaged density, g is the gravitational acceleration, and z is the depth. The SI represents the potential energy (J/m^3) needed to mix a water column, and a more considerable SI value indicates a stronger density stratification.

In Fig. 5.3a, the hourly river discharge of the Chikugo River is depicted, showcasing both the large-scale effluent in 2020 and the small-scale effluent in 2002. Fig. 5.3b and 5.3c compared the hourly SI and bottom DO, specifically at St.1. The strong stratification with a high SI reaching 600 J/m^3 can be attributed to the substantial influx of freshwater, which created a density contrast through a rapid reduction in surface salinity. Consequently, water exchange was suppressed, leading to water column stratification. Alternatively, moderate stratification persisted during periods of low river discharge, and the duration of this stratification was significantly shortened. In the summer, a gradual decrease in DO levels usually coincides with the onset of stratification. Nevertheless, the influence of freshwater on DO concentration can experience a time lag effect due to fluctuations in freshwater inflow rate and the presence of turbulent mixing conditions (Garvine et al., 1992).

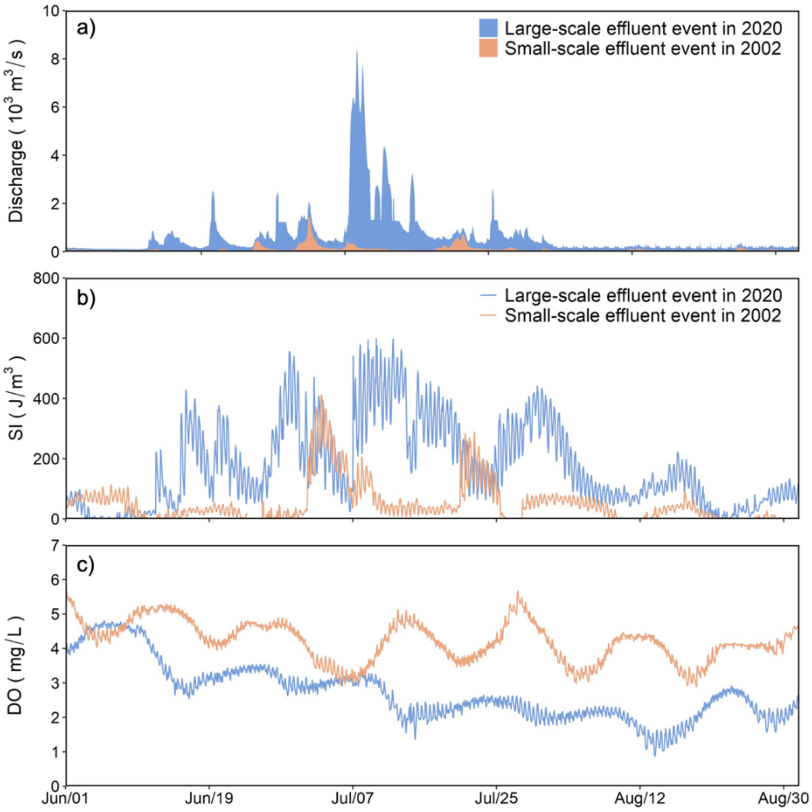

Figure 5.3 Time series of hourly a) river discharge of the Chikugo River, b) Stratification Index, and c) bottom DO in large-scale (2020) and small-scale (2002) effluent events.

Stratification duration determines the severity of hypoxia. As shown in Fig. 5.4b and d, sustained stratification occurred in early July, with hypoxia expanding upward from the bottom layer, accompanied by the emergence of anoxia. In a very small effluent scale (the peak discharge is only about 1000m^3/s), the stratification was not obvious, there was only very slight hypoxia, and the low DO state (DO < 4mg/L) repeated periodically (Fig. 5.4a and c). Tidal interactions, combined with freshwater inflow, play a pivotal role in shaping the stratification patterns of estuaries and shallow coastal areas, which not only account for the periodic variations in DO but also actively influence the distribution of DO by modifying water mixing dynamics and facilitating oxygen exchange processes (Haas, 1977; Chen et al., 2015).

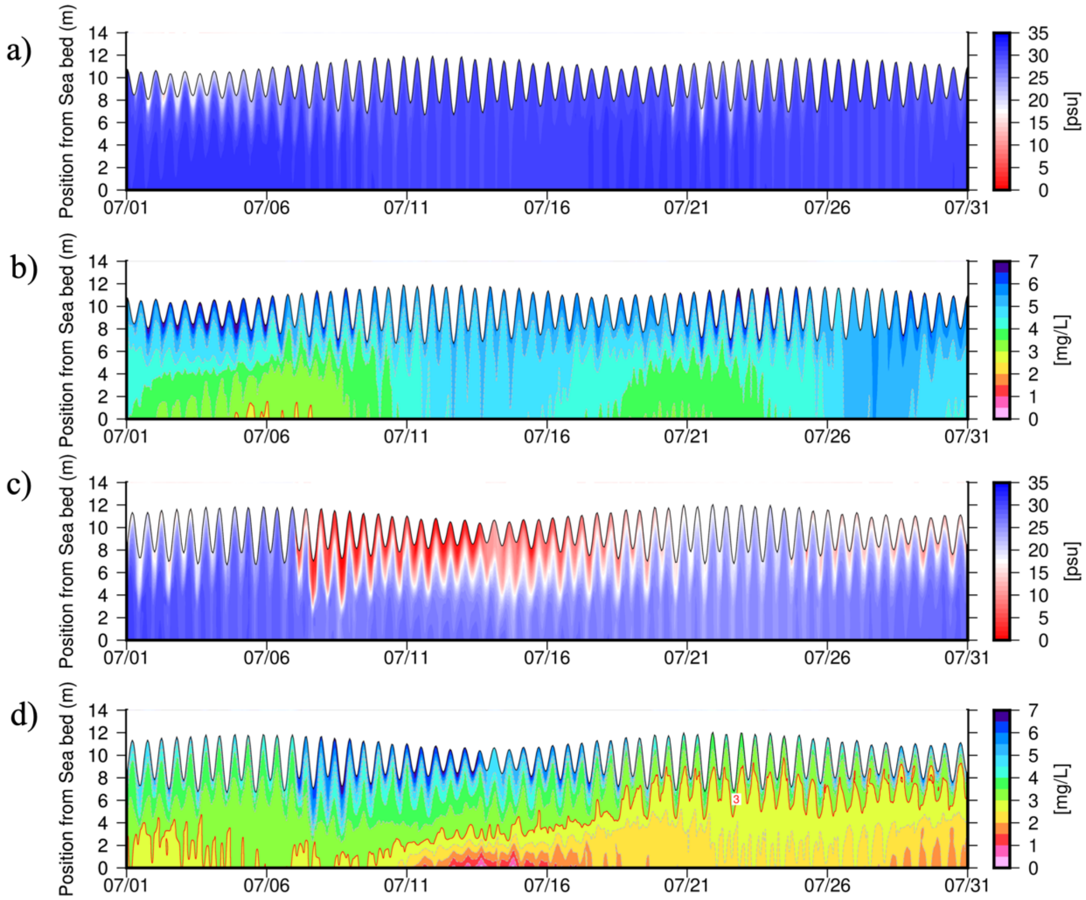

Figure 5.4 Isopleths of a) salinity in 2002, b) DO in 2002, c) salinity in 2020, and d) DO in 2020 at St.1. The red isolines in b) and d) represent DO = 3 mg/L.

5.4.2 The key role of effluent in summer hypoxia

The narrow and elongated distribution of the Ariake Sea, combined with its relatively narrow strait opening, hinders and complicates the seawater exchange at the strait entrance. As a typical Region of Freshwater Influence (ROFI), freshwater input from rivers acts as a non-uniformly distributed buoyancy source, creating and maintaining horizontal solid salinity gradients that give rise to a circulation pattern primarily governed by density differences (Simpson & Sharples, 2012). In contrast to surface heating, variations in freshwater input, tidal stirring, and wind forcing predominantly determine the hydrodynamic characteristics of the bay on various time scales. The DO levels in the Ariake Sea exhibit seasonal fluctuations, accompanied by hypoxia in summer and recovery in winter (Tsutsumi et al., 2015). During the summer, the frequent rainy periods bring about a significant rise in river discharge, becoming a primary factor contributing to hypoxia. Fig. 5.5 to Fig. 5.8 illustrate the correlation between effluent volume and the duration of hypoxia at six stations from 1992 to 2021 in four A-class rivers. Effluent volume refers to the cumulative volume of water inflowing during a single flood event caused by the rainy season, with the daily discharge exceeding or falling below the ordinary water discharge serving as the event's start or end. The duration of hypoxia represents the time in days during which bottom water experiences continuous hypoxia. In Fig. 5.5, the nearshore region (St. KS73) is more vulnerable to freshwater inflow and shows a stronger correlation (R = 0.82) between hypoxia duration and effluent volume compared to St.3 (R = 0.53), which is situated further away in the central area of the sea. Furthermore, the construction of the dike promoted changes in water exchange within Isahaya Bay. Prior to dike construction, the Honmyo River actively facilitated water exchange, leading to a reduced occurrence of hypoxia in the bay. Additionally, the correlation between effluent volume and the duration of hypoxia is influenced not only by the river outflow but also by the relative positioning of the river in relation to the observation station.

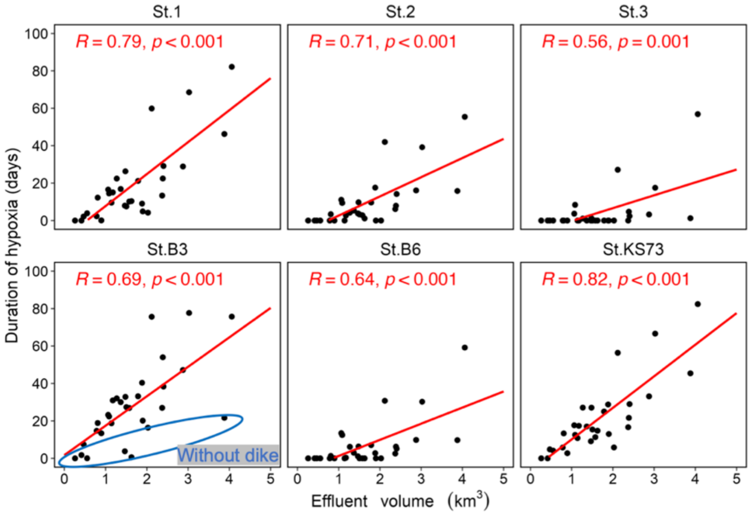

Figure 5.5 Correlation between the effluent volume of Chikugo R. and the duration of hypoxia at six stations over thirty years. Red solid lines indicate linear regression lines and blue oval in St.B3 indicates years without constructing the Isahaya dike.

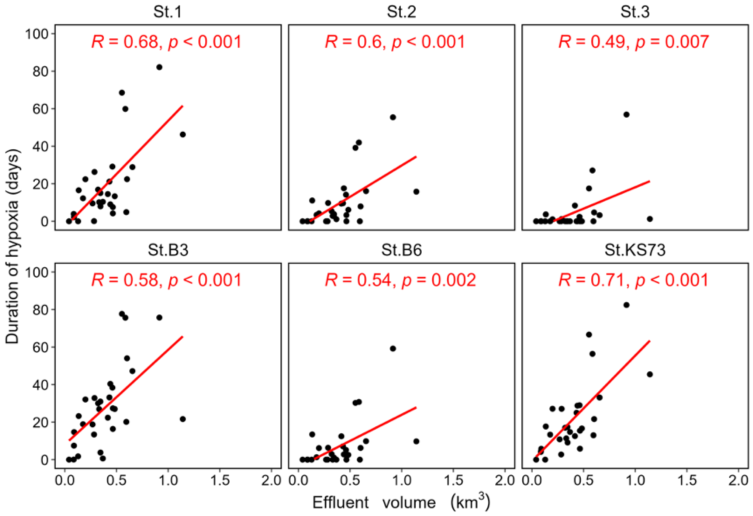

Figure 5.6 Correlation between the effluent volume of Yabe R. and the duration of hypoxia at six stations over thirty years. Red solid lines indicate linear regression lines.

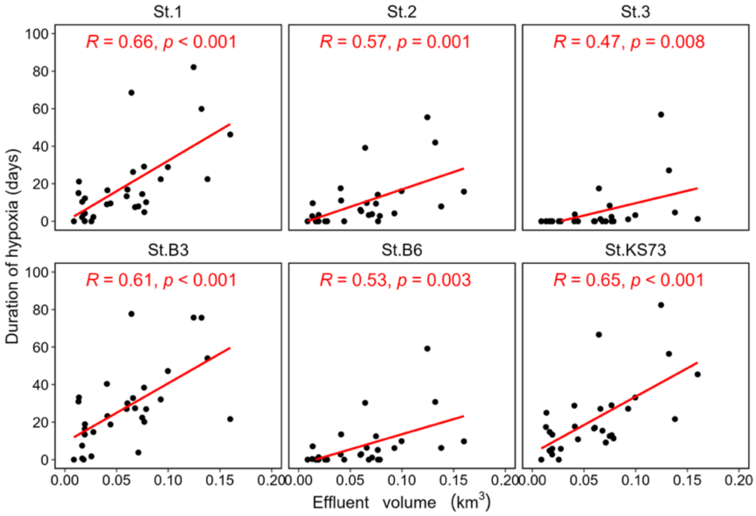

Figure 5.7 Correlation between the effluent volume of Rokkaku R. and the duration of hypoxia at six stations over thirty years. Red solid lines indicate linear regression lines.

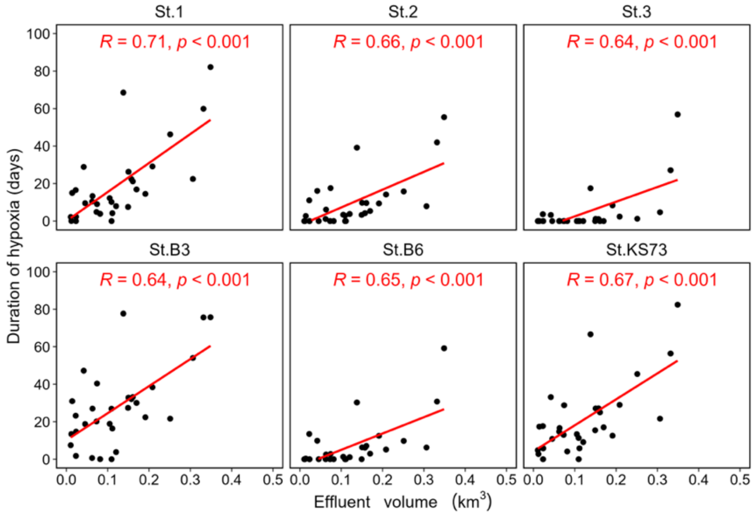

Figure 5.8 Correlation between the effluent volume of Kase R. and the duration of hypoxia at six stations over thirty years. Red solid lines indicate linear regression lines.

The decrease in DO levels can be explained by the restricted replenishment due to stratification, as well as the depletion caused by an excessive influx of nutrients leading to biological activity (Wu, 2002). The freshwater inflows may increase the input of nutrients, providing crucial conditions for the growth of phytoplankton (Chen et al., 2018). The high temperature will increase the metabolic rate and growth rate of phytoplankton, which synergistically promotes their reproductive capacity with nutrients (Rabalais et al., 2010). Fig. 5.9 indicates the correlation of bottom DO with various environmental variables in summer (June, July, and August). The analysis of monthly average values from 6 sites over a 30-year period consistently indicates a strong correlation between bottom DO and various factors. Salinity demonstrates a positive correlation (R=0.50), while water temperature (R=-0.49) and nutrient loading (R=-0.58) display negative correlations. Notably, there is a significant positive correlation (R=0.73) between bottom DO and algae. However, due to the complex dynamic relationship between river discharge and DO, changes in river discharge may affect DO levels with a specific time lag (Justić et al., 1993). This lag effect may result in a lower correlation coefficient between river discharge and DO.

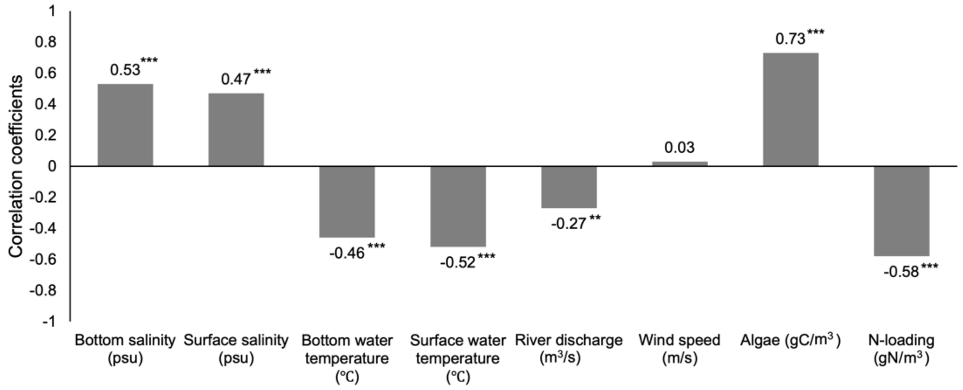

Figure 5.9 Correlation coefficients between monthly average DO concentration and various environmental variables across all stations in summer. The symbols indicate the statistical significance levels: ** for p-value < 0.01 and *** for p-value < 0.001.

5.4.3 Numerical experiments on nutrient loads

As previously established, nutrients hold a pivotal position in the marine ecosystem cycle. They actively contribute to the photosynthesis of phytoplankton, promote plant growth, and simultaneously serve as significant contributors to the occurrence of red tide. Additionally, nutrient salts indirectly influence the levels of DO and pH in water by engaging in the mineralization of organic matter. In the lower-trophic ecosystem model, nutrient loading is one of the boundary conditions, but due to the absence of continuous measurements for river nutrient concentrations, we adopt the L-Q equation generally used to estimate water quality parameters to calculate river outflow nutrients. The selected rivers were eight A-class rivers flowing into the Ariake/Yatsushiro Sea: Chikugo River, Rokkaku River, Kase River, Yabe River, Kikuchi River, Shirakawa River, Midori River, and Kuma River. A comprehensive description of the flow observatories, water quality observatories, and calculation results can be found in Tadokoro & Yano (2019).

In this study, we conducted a numerical experiment by modifying the equation coefficient (a) to increase nutrient loads from river inflow and then examined variations in DO levels under various magnified nutrient loading cases. The aim of this numerical experiment is to confirm the influence of modifications in nutrient loadings on hypoxia while simultaneously assessing the sensitivity of DO to these nutrient alterations. The nutrient loads (L) were calculated using the L-Q equation, which is described by:

$$L = aQ^b \tag{5.1}$$

where Q is river discharge (m^3/s), the coefficients a and b are determined using the Least Squares Method.

Table 5.1 Numerical experiments conditions and calculation results.

Cases	Coefficient a	Average DO change	Maximum DO change
1	a	-	-
2	$1.25a$	-4.69%	-11.80%
3	$1.5a$	-8.39%	-25.86%
4	$1.75a$	-15.64%	-43.31%
5	$2a$	-20.00%	-55.66%

Table 5.1 displays the coefficient settings for various cases in the numerical experiments and the rate of DO changes during hypoxia periods. For this numerical experiment, the cases were based on data affected by large-scale effluent during the summer of 2020. To minimize the influence of other factors such as water temperature, seasonal variations, wind, and currents, the hypoxia period assessed was defined as the first occurrence of hypoxia following the peak discharge.

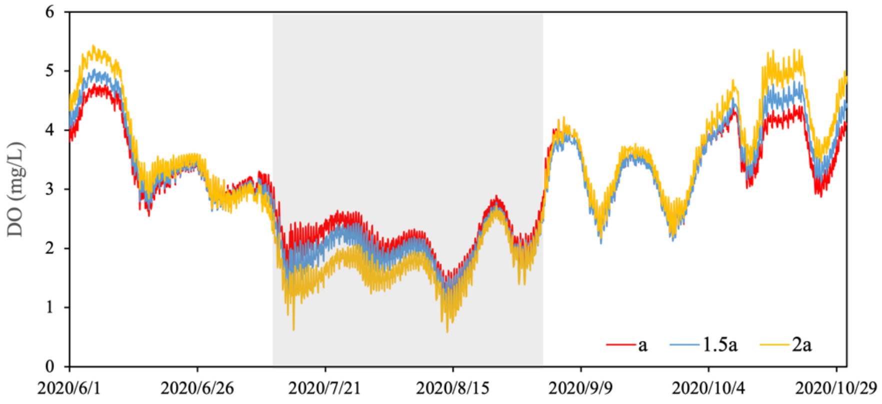

Figure 5.10 Time series of DO under different cases at St.1 in 2020.

Fig. 5.10 illustrates that within the hypoxia cycle, heightened nutrient levels correspond to diminished bottom DO. This may be because eutrophication leads to excessive growth of phytoplankton. Subsequently, the decomposition process following phytoplankton death consumes oxygen within the water body, making it difficult to replenish the DO at the bottom of the stratified water. Conversely, during non-flood periods, a moderate nutrient increase potentially stimulates phytoplankton photosynthesis, contributing to increased DO levels within the water body, particularly when the water column experiences efficient mixing.

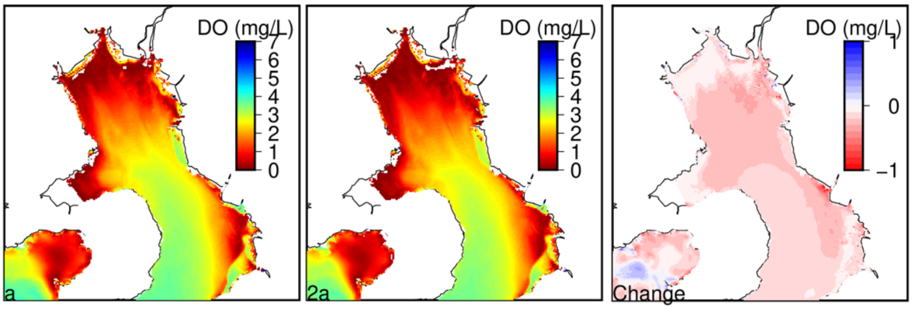

Figure 5.11 Spatial distribution of bottom DO under case 1 (left) and case 5 (middle), and DO change (right).

In our spatial analysis, we contrasted the progression of hypoxia between case 1 and case 5, examining the relative degree of change (Fig. 5.11). Elevated nutrient loading resulted in the expansion of bottom hypoxia, notably observed through intensified hypoxic conditions in the central bay area compared to its head, with a subsequent decline spanning the entire sea area.

5.5 Conclusions

In our previous chapter, we showcased how the extreme rainfall in 2020 broke historical records, resulting in an unprecedented duration of hypoxia in the Ariake Sea. This revealed the spatial impact of freshwater inflow on DO dynamics. Nevertheless, the precise relationship between river discharge and hypoxia remains partially elucidated. In this study, numerical models were employed for the first time to calculate and assess the long-term trend of hypoxia, as well as the effects of intense rainfall on hypoxia duration in the Ariake Sea spanning 1992 to 2021.

Our analysis was primarily focused on exploring the correlation between effluent volume and hypoxia duration, as well as evaluating the impact of freshwater inflow on salinity stratification using a stratification index. Furthermore, numerical experiments were conducted to evaluate the impact of nutrient loads carried by freshwater inflow on the extent of the hypoxic zone. From this research, three key conclusions emerged:

(1) The duration of hypoxia demonstrated a robust positive correlation with effluent volume near the river mouth, supported by notably high correlation coefficients (*e.g.*, R = 0.82 for St.KS73).

(2) Large-scale water discharge consistently induced stratification, contrasting with small-scale discharges, and emerges as the primary contributor to hypoxia formation.

(3) Various factors contributed to changes in DO concentration, particularly an increase in nutrient loads, leading to the expansion of the bottom hypoxic zone during the summer rainy season in the Ariake Sea.

Throughout this chapter, our 30-year simulation data has highlighted the crucial impact of summer effluent volume changes on the duration of hypoxia within the Ariake Sea. However, the spatial variations in the hypoxic zone remain unexplored. In our future research, our focus will shift towards understanding the spatial trends of hypoxia, aiming to achieve a more comprehensive understanding of hypoxia development in the Ariake Sea.

References

Chen, N., Krom, M. D., Wu, Y., Yu, D., & Hong, H. (2018). Storm induced estuarine turbidity maxima and controls on nutrient fluxes across river-estuary-coast continuum. *Science of The Total Environment*, *628–629*, 1108–1120. https://doi.org/10.1016/j.scitotenv.2018.02.060

Chen, X., Shen, Z., Li, Y., & Yang, Y. (2015). Tidal modulation of the hypoxia adjacent to the Yangtze Estuary in summer. *Marine Pollution Bulletin*, *100*(1), 453–463. https://doi.org/10.1016/j.marpolbul.2015.08.005

Elias, E. P. L., & Hansen, J. E. (2013). Understanding processes controlling sediment transports at the mouth of a highly energetic inlet system (San Francisco Bay, CA). *Marine Geology*, *345*, 207–220. https://doi.org/10.1016/j.margeo.2012.07.003

Garvine, R. W., McCarthy, R. K., & Wong, K.-C. (1992). The axial salinity distribution in the delaware estuary and its weak response to river discharge. *Estuarine, Coastal and Shelf Science*, *35*(2), 157–165. https://doi.org/10.1016/S0272-7714(05)80110-6

Haas, L. W. (1977). The effect of the spring-neap tidal cycle on the vertical salinity structure of the James, York and Rappahannock Rivers, Virginia, U.S.A. *Estuarine and Coastal Marine Science*, *5*(4), 485–496. https://doi.org/10.1016/0302-3524(77)90096-2

Hodoki, Y., & Murakami, T. (2006). Effects of tidal flat reclamation on sediment quality and hypoxia in Isahaya Bay. *Aquatic Conservation: Marine and Freshwater Ecosystems*, *16*(6), 555–567. https://doi.org/10.1002/aqc.723

Jia, R., Lei, H., Hino, T., & Arulrajah, A. (2018). Environmental changes in Ariake Sea of Japan and their relationships with Isahaya Bay reclamation. *Marine Pollution Bulletin*, *135*, 832–844. https://doi.org/10.1016/j.marpolbul.2018.08.008

Justić, D., Rabalais, N. N., Eugene Turner, R., & Wiseman, W. J. (1993). Seasonal coupling between riverborne nutrients, net productivity and hypoxia. *Marine Pollution Bulletin*, *26*(4), 184–189. https://doi.org/10.1016/0025-326X(93)90620-Y

Rabalais, N. N., Díaz, R. J., Levin, L. A., Turner, R. E., Gilbert, D., & Zhang, J. (2010). Dynamics and distribution of natural and human-caused hypoxia. *Biogeosciences*, *7*(2), 585–619. https://doi.org/10.5194/bg-7-585-2010

Simpson, J. H., Brown, J., Matthews, J., & Allen, G. (1990). Tidal Straining, Density Currents, and Stirring in the Control of Estuarine Stratification. *Estuaries*, *13*(2), 125. https://doi.org/10.2307/1351581

Simpson, J. H., & Sharples, J. (2012). *Introduction to the physical and biological oceanography of shelf seas*. Cambridge University Press.

Tadokoro, M., Yano, S., Peizhi, Q., & Orrheim, L. (2020). Effects of change of density stratification due to Isahaya Sea-Dyke on the fate of anoxic water in the Ariake Sea. *IOP Conference Series: Earth and Environmental Science*, *419*(1), 012161. https://doi.org/10.1088/1755-1315/419/1/012161

Tanaka M., & Odagiri M. (2010). Mechanism of the Oxygen-Depleted Water Formation near the Head of the Ariake Bay and its Numerical Modeling. *Journal of Japan Society of Civil Engineers, Ser. B2 (Coastal Engineering)*, *66*(1), 1011–1015. https://doi.org/10.2208/kaigan.66.1011

Tanaka, T., Kobayashi, K., & Tachikawa, Y. (2021). Simultaneous flood risk analysis and its future change among all the 109 class-A river basins in Japan using a large ensemble climate simulation database d4PDF. *Environmental Research Letters*, *16*(7), 074059. https://doi.org/10.1088/1748-9326/abfb2b

Tanaka, T., Tachikawa, Y., & Yorozu, K. (2015). A flood risk curve development for inundation disaster considering spatio-temporal rainfall distribution. *Proceedings of the International Association of Hydrological Sciences*, *370*, 57–62. https://doi.org/10.5194/piahs-370-57-2015

Tsutsumi, H., Takamatsu, A., Nagata, S., Orita, R., Umehara, A., Komorita, T., Shibanuma, S., Takahashi, T., Komatsu, T., & Montani, S. (2015). Implications of changes in the benthic environment and decline of macro-benthic communities in the inner part of Ariake Bay in relation to seasonal hypoxia. *Plankton and Benthos Research*, *10*(4), 187–201. https://doi.org/10.3800/pbr.10.187

Tadokoro, M., & Yano, S. (2019). Evaluation of Effects of Temperature and River

Discharge Changes due to Climate Change on Hypoxia in the Ariake Sea. *Journal of Japan Society of Civil Engineers, Ser. B2 (Coastal Engineering), 75(2)*, I_1231-I_1236. https://doi.org/10.2208/kaigan.75.I_1231

Yano S., Nishimura K., Kitagawa Y., & Abdul N. Arifin. (2014). Examination on Effects of River Flooding Pattern on Baroclinic Structure in the Ariake Sea. *Journal of Japan Society of Civil Engineers, Ser. B2 (Coastal Engineering)*, *70*(2), I_436-I_440. https://doi.org/10.2208/kaigan.70.I_436

Chapter 6

Long-term Developments in Seasonal Hypoxia and Response to Climate Change in the Ariake Sea

6.1 Introduction

The degradation of water quality may cause serious damage to the fisheries. Especially, since hypoxia usually occurs within the bottom water, it is very harmful to the benthic species and even the entire ecosystem (Tsutsumi et al., 2015; Kodama & Horiguchi, 2011). Numerous studies have established that changes in precipitation patterns, as one of the consequences of climate change, are driving the change in the river and marine systems (Tanaka et al., 2021).

Previous studies have highlighted that large river discharges due to heavy rainfall led to a decrease in salinity and the formation of a halocline, which inhibited the vertical transfer of dissolved oxygen (DO) from the surface to the bottom, thus promoting the persistence of hypoxia. In Chapter 5, we assessed the correlation between effluent volume and hypoxia duration, revealing a high correlation. However, these results are derived from observational points situated in the northern part of the Ariake Sea. The extent of change in the hypoxic area throughout the entire bay remains undetermined.

In this chapter, our assessment focuses on the trends in seafloor DO over the past 30 years (1992 to 2021) at a spatial scale. We also specifically analyzed the correlation between river outflow and sea hypoxia area. Additionally, we employ the same numerical model to investigate potential causes behind seasonal hypoxia throughout these three decades.

6.2 Methodology

In continuity with the methodology outlined in earlier chapters, the numerical model adopted in this section remains consistent with the model previously detailed in Chapter 3. This model, coupled with a general coastal 3D hydrodynamic model and a lower-trophic ecosystem model, serves as the foundational tool for our analysis. Building upon the established framework, the setup and configuration of these numerical models, as well as the meticulous methods employed for compiling data.

6.3 Results and Discussion

6.3.1 River discharge and hypoxia

To clarify the impact of river discharge on the long-term trend of hypoxia, this section specifically focuses on presenting time series graphs depicting the long-term river discharge and hypoxic area. The time series plot in Fig 6.1a shows a rising trend in the annual maximum discharge of the Chikugo River during the summer rainy season. Especially, the annual maximum discharge in 2020 reached approximately 5224.70 m^3/s and the total effluent volume reached roughly 4 km^3 during the effluent period from 11 June 2020 to 3 October 2020, which is 2.3 times the average effluent volume in 30 years (from 1992 to 2021). Fig. 6.1b shows the time series of the hypoxic area at the bottom layer. The hypoxic area here refers to the most severe single-day area of hypoxia after the effluent, which occurred during the neap tides and indicated an overall upward trend.

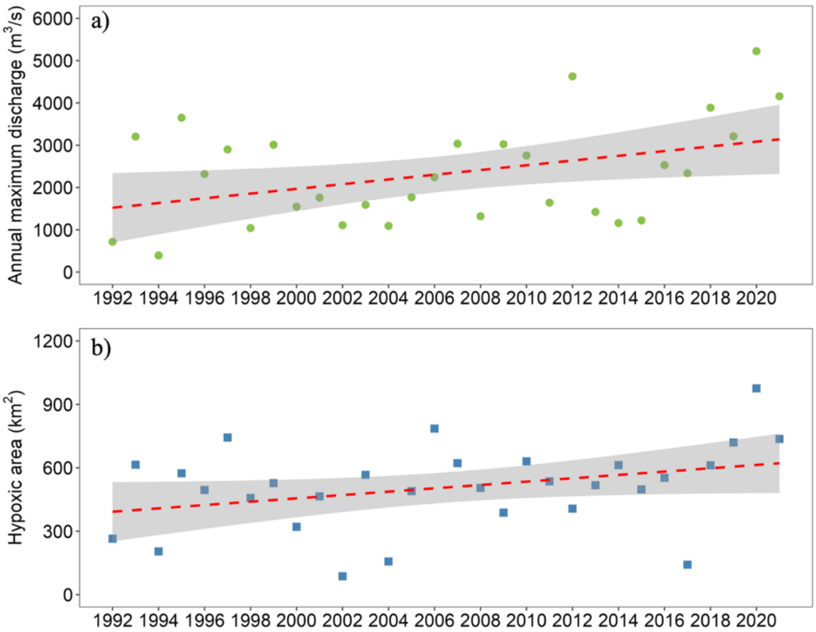

Figure 6.1 Time series of a) annual maximum discharge of Chikugo River and b) the bottom hypoxic area when it reaches its largest extent following the effluent. The red dashed line represents the linear trendline, and the gray area represents the 95% confidence interval.

Fig. 6.2 indicates the relationship between effluent volume and peak discharge, as well as the persistence of hypoxia and hypoxic area. Effluent volume, derived from the Chikugo River and hypoxia duration refers to the average duration of hypoxic conditions across six observation points. Previous studies have established a strong correlation between hypoxia duration and river discharge. However, the addition of multiple correlations in this section aims to assess hypoxia development from both duration and hypoxic area. Compared to peak discharge, the effluent volume had a stronger correlation with hypoxia duration and the extent of the hypoxic area. Regarding spatial distribution, moderate hypoxia exhibited a higher frequency compared to other scales while concerning the duration, hypoxia tended to concentrate within short-duration hypoxia. In addition, there was also a high correlation between hypoxic area and hypoxia duration, with a correlation coefficient of 0.76.

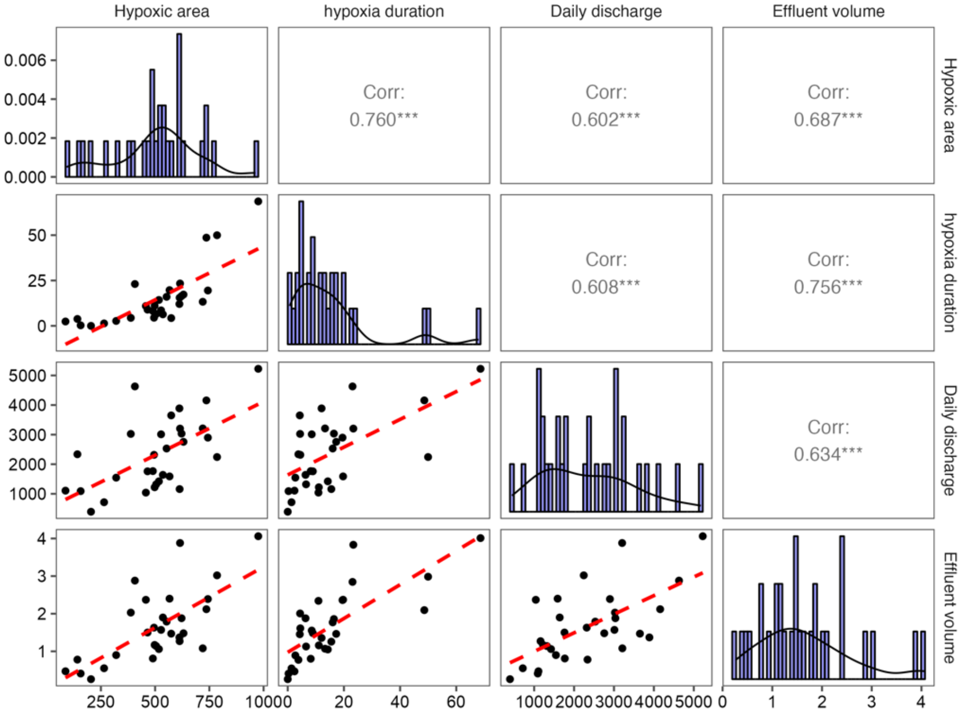

Figure 6.2 Multiple linear regression for hypoxic area (km^2), hypoxia duration (day), maximum daily discharge (m^3/s), and effluent (km^3). The symbols indicate the statistical significance levels: *** for p-value < 0.001.

6.3.2 Long-term trend in hypoxia

Intense summer rainfall, resulting in substantial freshwater inflow, frequently exacerbates hypoxia, demonstrating a distinct seasonal pattern. Fig. 6.3 illustrates the trend in the bottom DO levels resulting from climate change, with hypoxic and anoxic areas steadily expanding to varying extents. In contrast to the comparatively modest growth observed in the simulations for the period from 1992 to 2010, with an average annual increase of 3.52 km²/yr, the trend of growth in the hypoxic area from 2010 to 2021 exhibited a notably steeper incline, averaging 22.5 km²/yr. The anoxic area has increased from virtually non-existent to approximately 100 km^2 presently. On the other hand, several significant hypoxic events (notably occurring in 1993, 1997, 2006, and 2020) were accompanied by substantial effluent volume ranging from 2 to 4 km^3 from the Chikugo River. Simultaneously, the frequency of extremely severe hypoxic events was also on the rise.

Fig. 6.4 further indicates the long-term change in the hypoxic area during neap tides following the largest summer flood events from 1992 to 2021. The head of the Ariake Sea is profoundly influenced by tidal dynamics, resulting in intense mixing during spring tides, which mitigates the conditions for hypoxia formation. Conversely, during neap tides, the interaction of limited mixing and high stratification promotes the development of hypoxia. Long-term numerical simulations of DO reveal a declining trend, accompanied by the extension of hypoxic area from the head to the central areas. Moreover, the sustained depletion resulting in anoxia appears to be a novel feature of nearshore waters in recent years.

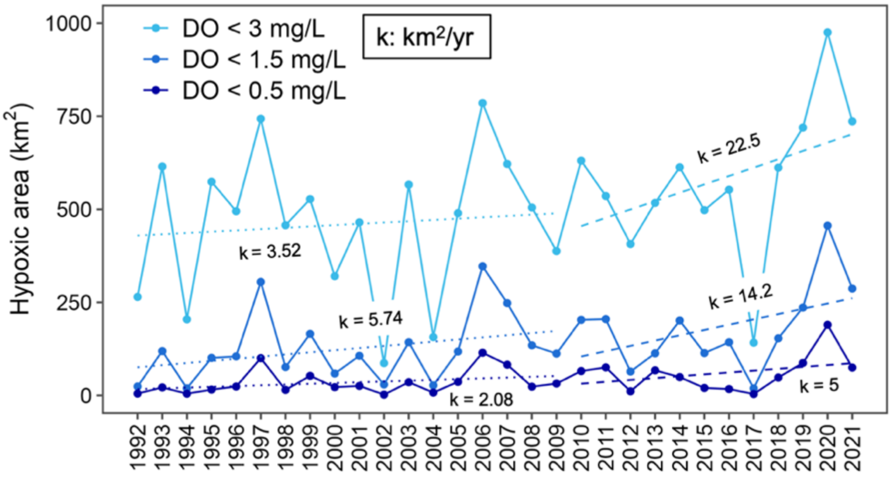

Figure 6.3 Interannual variability of the hypoxic area at the bottom during 1992-2021. The dotted lines represent the trend lines for the period from 1992 to 2009 and the dashed lines represent the trend lines for the period from 2010 to 2021.

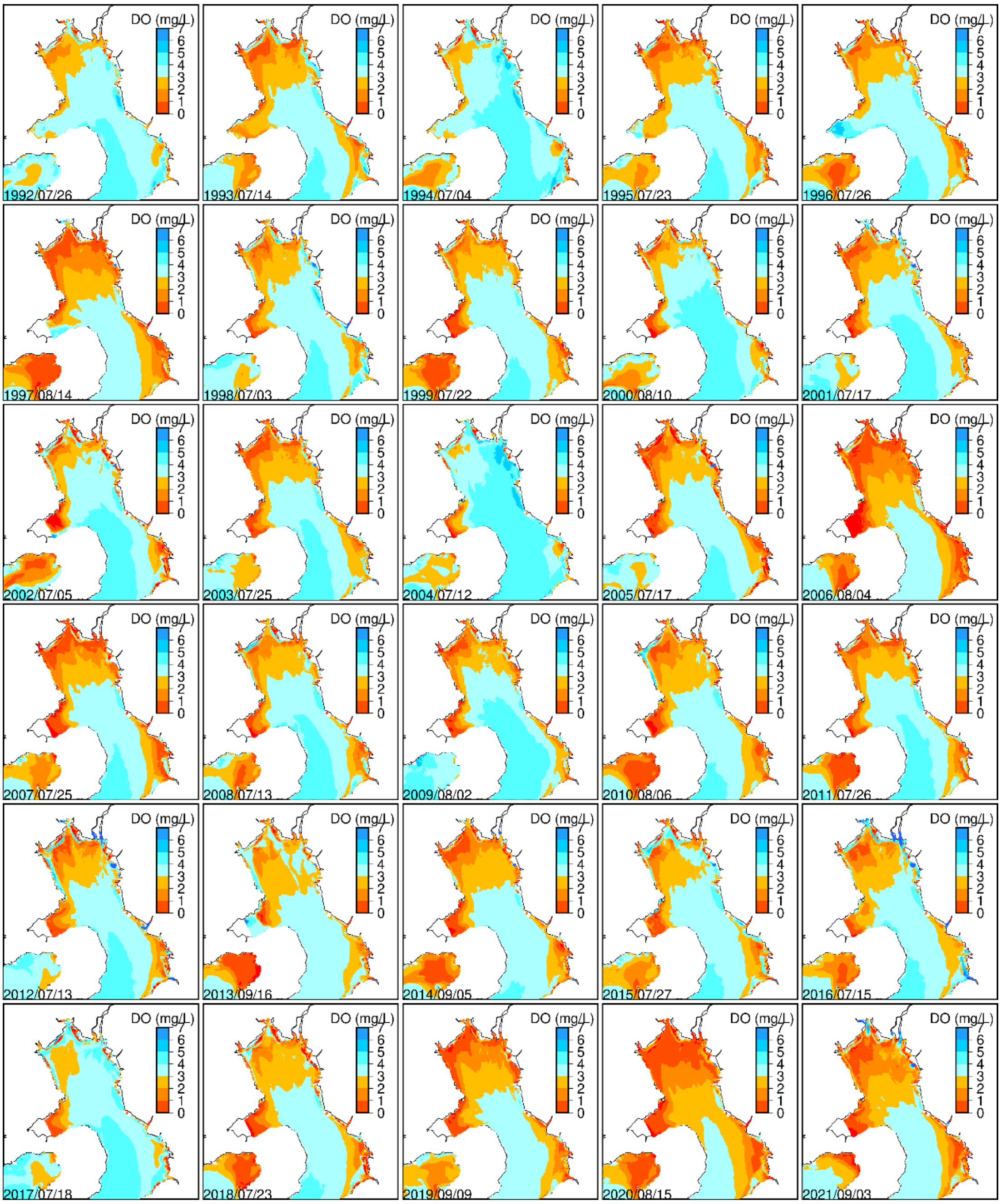

Figure 6.4 Spatial distribution of bottom DO levels during the neap tide period following the largest summer flood events over a thirty-year span from 1992 to 2021.

6.3.3 Response to the climate change

The rising water levels caused by global warming have become a global issue that affects ecosystems and human societies in coastal areas, with model predictions indicating that tidal dissipation will decrease as the water levels rise (Green, 2010).

Changes in stratification resulting from shifts in precipitation patterns will alter the ROFI environment. Changes in salinity directly affect the biodiversity and distribution of marine environments and coastal ecosystems (Aladin et al., 2009; Des et al., 2021). The decline in salinity, influenced by freshwater input, represents not only a short-term alteration but also a seasonal fluctuation. This change is one of the environmental shifts in the Ariake Sea, consequently affecting its ecosystem. Aoki et al. (2015) indicate that algae blooms in the Ariake Sea coincide with declining salinity, which is directly correlated with increased river discharge and present a spatial differentiation.

Fig. 6.5 shows the changes in environmental variables during the summer of 1992-2021, encompassing salinity, water temperature, river discharge, wind speed, DO, and nutrient loading (NH_4^+ and NO_3^-). Compared to the bottom layer salinity, the surface salinity showed an overall decreasing trend (with slopes of 0.03 and 0.06 in July and August, respectively), while the water temperature exhibited an overall increasing trend. In addition, another notable trend is the decline in DO, which can be attributed to the adverse effects of temperature and freshwater inputs. As water temperatures rise, oxygen solubility decreases, leading to lower DO levels. Additionally, increased freshwater inputs from sources such as rivers can dilute the water and reduce the concentration of DO. Another factor that restricts DO levels is the persistent rise in nutrient influx from freshwater sources, which amplifies the declining trend of DO levels.

In addition, Fig. 6.5g demonstrates an increasing trend in wind speed. This could be attributed to climate change, as global warming can lead to alterations in weather patterns, including the intensity and frequency of winds. The rise in wind speed can enhance the mixing within water bodies, consequently influencing the distribution of environmental variables and transport processes (Nakata et al., 2009). All these changes indicate that climate change significantly impacts the Ariake Sea. Shifts in precipitation patterns will alter the morphology of river mouths and river runoff, as well as nutrient inputs (Hoitink et al., 2017). These alterations have had a noticeable impact on the biological and chemical characteristics of the water, including changes in salinity, temperature, and DO levels.

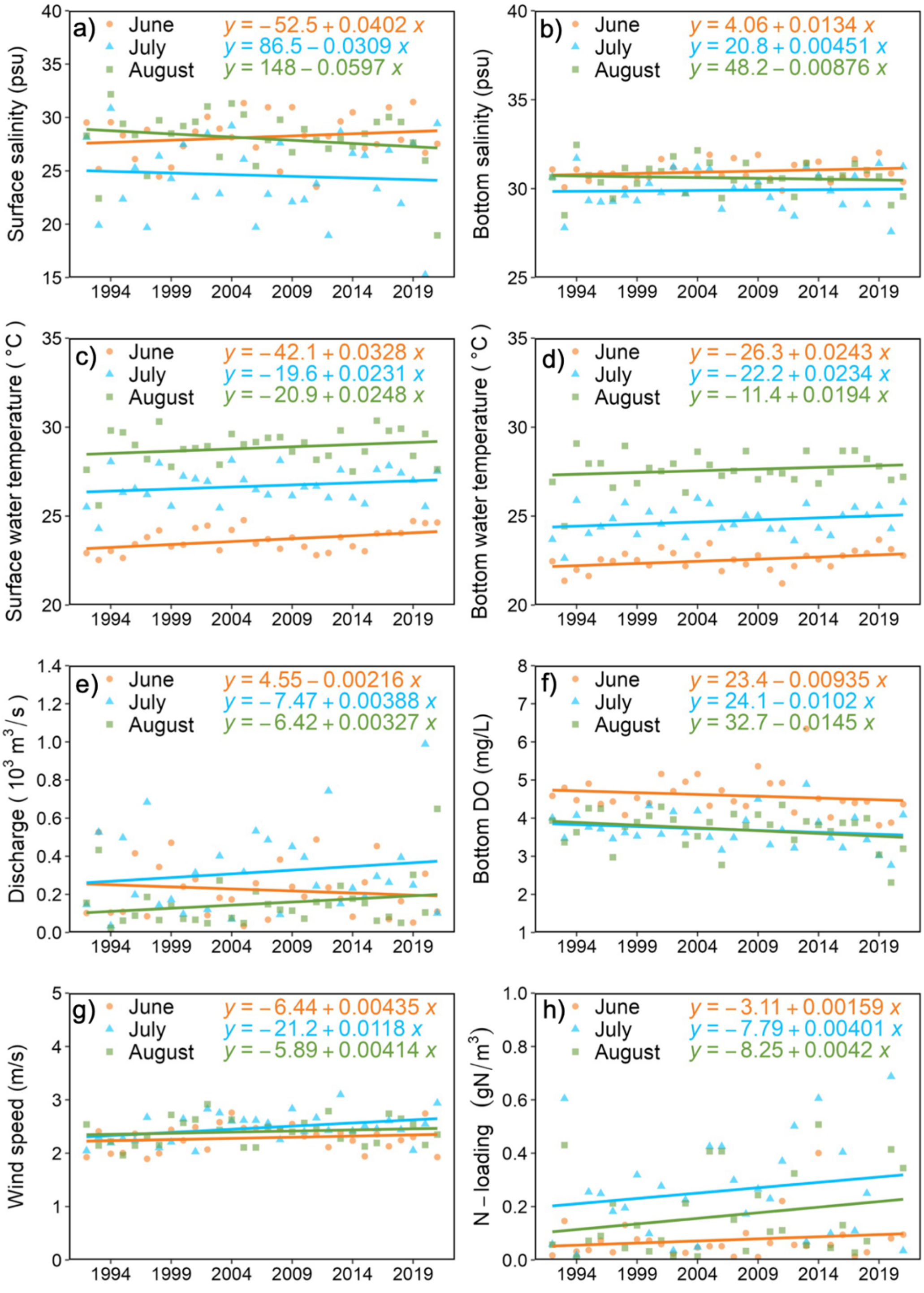

Figure 6.5 Time series of monthly averaged environmental variables from 1992 to 2021 for six observational stations: a) surface salinity, b) bottom salinity, c) surface temperature, d) bottom temperature, e) river discharge, f) bottom DO, g) wind speed and h) N-loading in June, July, and August.

6.4 Conclusions

This study employed numerical models to assess the long-term trend of hypoxia and the influence of heavy rainfall on hypoxia duration in the Ariake Sea spanning from 1992 to 2021. An assessment of environmental drivers, including salinity, water temperature, wind speed, and nutrient loading, was conducted. The results indicate:

(1) Hypoxia displayed an expanding spatial trend, stretching from the Ariake Sea's head towards its central regions due to climate-induced shifts. The model analysis illustrated a substantial 1.7 times increase in the hypoxic area, with anoxic regions expanding from negligible to covering approximately 100 km^2.

(2) A numerical analysis of various environmental factors highlighted diverse responses to climate change within the Ariake Sea region. These responses suggested potential declines in both physical attributes and water quality parameters, indicating significant alterations in the local ecological communities.

This detailed understanding of climate change's impact on coastal environments yields valuable insights, laying a foundation for devising practical adaptation strategies and environmental policies.

References

Aladin, N. V., Plotnikov, I. S., Micklin, P., & Ballatore, T. (2009). Aral Sea: Water level, salinity and long-term changes in biological communities of an endangered ecosystem-past, present and future. *Natural Resources and Environmental Issues*, *15*(1), 36.

Aoki, K., Onitsuka, G., Shimizu, M., Yamatogi, T., Ishida, N., Kitahara, S., & Hirano, K. (2015). Chattonella (Raphidophyceae) bloom spatio-temporal variations in Tachibana Bay and the southern area of Ariake Sea, Japan: Interregional displacement patterns with Skeletonema (Bacillariophyceae). *Marine Pollution Bulletin*, *99*(1–2), 54–60. https://doi.org/10.1016/j.marpolbul.2015.07.063

Des, M., Fernández-Nóvoa, D., deCastro, M., Gómez-Gesteira, J. L., Sousa, M. C., & Gómez-Gesteira, M. (2021). Modeling salinity drop in estuarine areas under extreme precipitation events within a context of climate change: Effect on bivalve mortality in Galician Rías Baixas. *Science of The Total Environment*, *790*, 148147. https://doi.org/10.1016/j.scitotenv.2021.148147

Green, J. A. M. (2010). Ocean tides and resonance. *Ocean Dynamics*, *60*(5), 1243–1253. https://doi.org/10.1007/s10236-010-0331-1

Hoitink, A. J. F., Wang, Z. B., Vermeulen, B., Huismans, Y., & Kästner, K. (2017). Tidal controls on river delta morphology. *Nature Geoscience*, *10*(9), 637–645. https://doi.org/10.1038/ngeo3000

Kodama, K., & Horiguchi, T. (2011). Effects of hypoxia on benthic organisms in Tokyo Bay, Japan: A review. *Marine Pollution Bulletin*, *63*(5–12), 215–220. https://doi.org/10.1016/j.marpolbul.2011.04.022

Nakata, H., Mishina, H., Takahashi, T., & Hirano, K. (2009). *A Newly Emerging Environmental Issue: Development of Hypoxia in the Bottom Water of Ariake Bay*.

Tanaka, T., Kobayashi, K., & Tachikawa, Y. (2021). Simultaneous flood risk analysis and its future change among all the 109 class-A river basins in Japan using a large ensemble climate simulation database d4PDF. *Environmental Research Letters*, *16*(7), 074059. https://doi.org/10.1088/1748-9326/abfb2b

Tsutsumi, H., Takamatsu, A., Nagata, S., Orita, R., Umehara, A., Komorita, T., Shibanuma, S., Takahashi, T., Komatsu, T., & Montani, S. (2015). Implications of changes in the benthic environment and decline of macro-benthic communities in the inner part of Ariake Bay in relation to seasonal hypoxia. *Plankton and Benthos Research*, *10*(4), 187–201. https://doi.org/10.3800/pbr.10.187

Chapter 7

Conclusions

Climate change has led to a surge in extreme rainfall occurrences, amplifying their frequency and magnitude. This surge significantly harms marine ecology and coastal economies. Notably, the post-2000 decline of seaweed in the Ariake Sea has brought widespread attention to the environmental degradation within the region. Similarly, the Yatsushiro Sea has witnessed a substantial decline in fish production over the past decade.

Previous studies primarily relied on on-site water quality monitoring to investigate the Ariake Sea. While crucial for comprehending environmental characteristics, this approach falls short in aiding the development of effective improvement measures. Monitoring during the summer rainy season proves challenging, impeding accurate assessments of extreme event impacts.

To address this, this study employed a coupled 3D hydrodynamic and ecological model, boasting proven reproducibility. This model facilitated the analysis of DO dynamics, especially during hypoxic events triggered by extreme rainfall. By utilizing this model, hypoxia duration was calculated, and its vertical and spatial distribution within the Ariake and Yatsushiro Seas was assessed. Additionally, for the first time, our model evaluated long-term trends in ecological variables (*e.g.*, water temperature, salinity, DO) spanning over 30 years in the Ariake Sea.

Key findings from the study include:

(1) Extreme summer rainfall intensified freshwater inflow into the Ariake Sea, inducing severe water column stratification that obstructs DO exchange. The 2020 Kyushu floods resulted in more prolonged hypoxia compared to the 2006 record event. Similarly impacting the Yatsushiro Sea, the 2020 extreme rainfall led to historically prolonged hypoxia, affecting almost all areas.

(2) Hypoxia duration strongly correlated with effluent volume near the Ariake Sea estuary (*e.g.*, R = 0.82 for St.KS73). The correlation remained significant

albeit lower in the central region (R = 0.56 for St.3). Furthermore, the scale of effluent volume had an impact on the hypoxic area, exhibiting a correlation coefficient of 0.69.

(3) Long-term analysis revealed a deteriorating trend in summer bottom DO at spatial scales, particularly during large-scale effluent events. Notably, hypoxia area have surged 1.7 times, with anoxic regions expanding from negligible to covering approximately 100 km^2. After 2010, this surge accelerated significantly.

(4) Over three decades, environmental responses to climate change have led to noteworthy shifts in temperature patterns and precipitation trends. Summer water temperatures rose by 0.035 °C annually, while surface salinity declined at 0.1 psu per year. This change has escalated extreme rainfall frequency and intensity, resulting in a 50% average annual increase in river flows between 1992 and 2021, along with amplified nutrient loads.

The escalation and prevalence of hypoxia pose a growing challenge in global coastal waters. Current water quality management strategies may prove insufficient in addressing deteriorating water quality due to climate change. Innovative, integrated basin-wide hydrology and water quality management strategies have the potential to mitigate hypoxia within the Ariake Sea. In further studies, it is necessary to combine hydrological models with numerical models for accurate simulations to provide an adequate basis for fisheries and human development adaptation.